

TISSUE EQUIVALENT PHANTOM DEVELOPMENT FOR BIOMEDICAL
APPLICATIONS

By

DAVID MICHAEL PETERSON

A DISSERTATION PRESENTED TO THE GRADUATE SCHOOL
OF THE UNIVERSITY OF FLORIDA IN PARTIAL FULFILLMENT
OF THE REQUIREMENTS FOR THE DEGREE OF
DOCTOR OF PHILOSOPHY

UNIVERSITY OF FLORIDA

2009

© 2009 David Michael Peterson

To my wonderful wife, Tiffany; our two children, Cody and Hunter; my parents, David and Helen, I thank you all for your loving support through this endeavor.

ACKNOWLEDGMENTS

The author gratefully acknowledges the support from family and friends to enable this accomplishment. He also greatly appreciates the support from the staff and faculty at the University of Florida, McKnight Brain Institute and fellow students of the Department of Biomedical Engineering. In addition, the entire teams at Convergent Engineering and the University of Florida, Electrical and Computer Engineering working on the electronic pill project have been helpful and have provided a good academic environment, I want to specifically thank Hong Yu for his assistance through this project. Dr. Jeffrey Fitzsimmons has been an admirable mentor and friend, allowing academic freedom while providing guidance and he has always shown the highest regard for my life goals, whether personal or professional. The author is also thankful to Dr. Neil Euliano and Dr. Brian Watson for many fruitful discussions and professional guidance.

TABLE OF CONTENTS

	<u>page</u>
ACKNOWLEDGMENTS.....	4
LIST OF TABLES.....	8
LIST OF FIGURES.....	9
ABSTRACT.....	12
CHAPTER	
1 INTRODUCTION.....	13
Phantoms.....	14
Conductivity.....	16
Permittivity.....	16
Measurement of Conductivity and Permittivity in the Radio Frequency Range.....	17
Current Standards.....	21
INIRC-IRPA.....	22
NCRP.....	23
IEEE.....	23
Guidelines Summary.....	24
Maximum Permissible Exposure.....	25
Specific Absorption Rate.....	26
SAR with Far Field Assumptions.....	27
Discussion of the Far Field Assumptions.....	29
2 REVIEW OF THE STATE OF THE ART.....	32
Objective.....	32
Debye Formula and Cole-Cole Modification for Complex Permittivity.....	33
Use of Coaxial Probes for Measuring Permittivity.....	34
HP85070C Dielectric Probe.....	35
8752A Vector Network Analyzer.....	35
Computer and Software.....	36
Uncertainty of the Measurement.....	36
Phantoms Characteristics.....	37
Saline Phantoms.....	38
Tissue Equivalent Phantoms.....	39
Segmented Tissue Equivalent Phantoms.....	39
3 ANTENNA SIMULATIONS.....	41
Computational Method for Solving Maxwell's Equations.....	42
Description of the Simulation Setup and Parameters.....	43

	Dipole in air	44
	Folded dipole on the human body	48
	MRI coil on the human body	52
	MRI coil on the 1 S/m saline phantom.....	58
	Folded dipole antenna on the 1 S/m saline phantom	63
	Summary.....	69
4	PHANTOM CONSTRUCTION, TESTING AND ASSESSMENT	71
	Introduction	71
	Materials and Methods	76
	Results	80
	Phantom Attenuation Using A VCO To Determine Losses When Transmitting Signals From Inside The Body And Receiving Signals Outside The Body	83
	Materials and Methods	83
	Results	84
	Conclusions	84
5	COMPARISON OF SIMULATION AND PHANTOM RESULTS	86
	Introduction	86
	Description of the Experimental Setup.....	86
	Results	90
	Folded Dipole Heating and SAR in the Tissue Equivalent Phantom	90
	Folded Dipole Heating and SAR in the Saline Phantom	91
	MRI Coil Heating and SAR in the Tissue Equivalent Phantom	91
	MRI Coil Heating and SAR in the Saline Phantom.....	91
	Conclusions	91
6	EXAMPLE APPLICATIONS APPLIED TO PHANTOMS	93
	Introduction	93
	Medication Compliance Through The Use Of a Passive Electronic Pill	93
	Fundamental Operating Procedures of the Proposed Passive RF Detection System and its Theory of Operation	97
	Resonance of an Electronic Pill Antenna.....	101
	Empirical measurements in Solution, ISM 902-928 MHz Band	104
	Applications to MRI at 21T (900MHz)	106
	MRI theory, Quantum Mechanics of NMR/MRI	106
	Classical Description of NMR/MRI	107
	MRI Bench Experiments and Results	110
7	SUMMARY AND FUTURE WORK	112
	Summary.....	112
	Future Work	114

LIST OF REFERENCES..... 116
BIOGRAPHICAL SKETCH..... 124

LIST OF TABLES

<u>Table</u>		<u>page</u>
4-1	The table above shows the electrical parameters of skin versus an acrylic outside sheet used for phantom construction.	73
4-2	Main tissues in the human torso (excluding bone and skin), that are to be used in the human torso phantom.	75
4-3	Combined tissues used in the human torso phantom.....	75
4-4	Measured average tissues used in the human torso phantom.....	77
4-5	Transmission attenuation through various mediums	84
6-1	Capacitance versus inductance values for a given frequency. *Actual capacitor used, #corresponding frequency.	103
6-2	Capacitance versus inductance values for a given frequency. *Actual capacitor used, #corresponding frequency.	103
6-3	Capacitance versus inductance values for a given frequency. *Actual capacitor used, #corresponding frequency.	103
6-5	Capacitance versus inductance values for a given frequency. *Actual capacitor used, #corresponding frequency.	104
7-1	Summary of 45mm MRI coil experiments.	114
7-2	Summary of folded dipole experiments.	114

LIST OF FIGURES

<u>Figure</u>	<u>page</u>
3-1 A $\lambda/2$ dipole with a total length of approximately 32.4 cm and each segment being approximately 8.2 cm.....	45
3-2 A folded dipole demonstrating a tuned and matched configuration at 915 MHz.....	46
3-3 The radiation pattern of a standard $\lambda/2$ dipole antenna at 915 MHz in air.....	47
3-4 The 3D radiation pattern for a dipole at 915MHz is displayed as a reference.	47
3-5 A folded dipole that was simulated, showing its location on the human body model.	48
3-6 A folded dipole demonstrating a tuned and matched configuration at 914 MHz.....	49
3-7 The Phi and Theta patterns of the folded dipole antenna.....	50
3-8 A 3D look at the combined Phi and Theta patterns of the folded dipole applied to the human body model at 914 MHz.	50
3-9 The SAR distribution for the folded dipole on the human body model.....	51
3-10 SAR for 1 gram average violating the safety guidelines by exceeding 9W/kg. ...	52
3-11 The MRI coil that was simulated, showing its location on the human body model, using the same location as the folded dipole.	53
3-12 The MRI coil that was simulated, showing its location on the human body model, using the same location as the folded dipole, tuned to 915 MHz.....	54
3-13 The Phi and Theta patterns of the MRI coil, from this we can see that the Theta pattern is disturbed by the human body model.....	55
3-14 A 3D look at the combined Phi and Theta patterns of the MRI coil applied to the human body model at 915 MHz.....	56
3-15 The MRI coil simulation, showing its location on the human body model, using the same location as the folded dipole.	57
3-16 SAR for 1 gram average violating the safety guidelines by exceeding 5W/kg. ...	57
3-17 The MRI coil that was simulated, showing its location on the saline model.	58
3-18 The MRI coil that was simulated, tuned to approximately 904 MHz	59

3-19	The Phi and Theta patterns of the MRI coil.....	60
3-20	A 3D look at the combined Phi and Theta patterns of the MRI coil applied to the saline box at 905 MHz.	61
3-21	The MRI coil simulation, showing its location on the human body model, using the same location as the folded dipole.	62
3-22	SAR for 1 gram average violating the safety guidelines by exceeding 5W/kg. ..	63
3-23	The MRI coil that was simulated, showing its location on the human body model, using the same location as the folded dipole.	64
3-24	The folded dipole antenna was simulated, tuned to approximately 928 MHz.....	65
3-25	The Phi and Theta patterns of the MRI coil, from this we can see that the Phi pattern is disturbed by the saline box.	66
3-26	A 3D look at the combined Phi and Theta patterns of the MRI coil applied to the saline box at 905 MHz.	67
3-27	The MRI coil simulation, showing its location on the human body model, using the same location as the folded dipole.	68
3-28	SAR for 1 gram average violating the safety guidelines by exceeding 1.6W/kg.....	69
4-1	Measurements of various geographical locations in the human torso to determine the phantom size requirements based on the REMCOM human body model.	72
4-2	This setup shows the coaxial probe mounted in a fixture.....	76
4-3	Phantom construction, outer most layers are acrylic, followed by fat and then plastic wrap, in the bottom of the phantom is the lower average abdomen and the PVC piping on the center and to the left represent the esophagus and the stomach.	78
4-4	Heart, liver spleen mixture shown in the plastic bags.....	78
4-5	Another view showing the central organ mixture of heart liver and spleen, demonstrating the concentric nature of the phantom.	79
4-6	Final muscle layers filling in the area between the fat and the central organs, topping off the phantom with upper chest, back and shoulder muscles.	79
4-7	A 45 mm MRI surface coil matched to the human body in blue.....	81
4-8	Folded dipole tuned and matched to the human body in blue.....	82

5-1	Folded dipole matched to the human body placed on the tissue equivalent phantom at 914 MHz with a 2W sinusoidal waveform applied.	88
5-2	MRI coil matched to the human body placed on the tissue equivalent phantom at 915 MHz with a 2W sinusoidal waveform applied.	88
5-3	Folded dipole matched to the human body placed on the saline phantom at 914MHz with a 2W sinusoidal waveform applied.....	89
5-4	MRI coil matched to the human body placed on the saline phantom at 904 MHz with a 2W sinusoidal waveform applied.	89
6-1	The phase detected signal in the time domain after filtering. The distinct peak is the actual transition of a 180 degree phase shift at resonance.	100
6-2	Shows the probe set and pills with 1mm – 5mm traces. and on the right is the Q of a 5 mm wide trace pill resonated with a 4.7pF capacito	102
6-3	Plot on the left is from a swept source (frequency generator), 908-916MHz, ..	104
6-4	Plot on the left shows single frequency transmitted at 912MHz	105
6-5	Plot on the left shows a continuous wave (CW) at a single frequency of 912MHz	105
6-6	A 45 mm MRI surface coil matched to the human body in blue, saline in red and the tissue equivalent phantom in green at 915MHz.	111

Abstract of Dissertation Presented to the Graduate School
of the University of Florida in Partial Fulfillment of the
Requirements for the Degree of Doctor of Philosophy

TISSUE EQUIVALENT PHANTOM DEVELOPMENT FOR BIOMEDICAL
APPLICATIONS

By

David Michael Peterson

December 2009

Chair: Jeffrey R. Fitzsimmons
Major: Biomedical Engineering

The objective of this research was to develop a new “tissue equivalent phantom” to assist in the development of biomedical applications that utilize radio frequency transmissions. New technologies will be evaluated using the phantom. The knowledge gained is combined through simulation with real world measurements. Technologies can be evaluated without unnecessarily burdening human subjects or requiring the use of cadavers for system evaluation. A brief history of currently available phantom technology is presented, including the transition from bulk loading phantoms to more complicated phantoms that modify the conductivity and permittivity of the phantom. In a standard saline phantom only the conductivity is modified. Comparative analysis was performed and showed agreement between the simulation and the phantom. The phantom and simulation experiments were then confirmed with human experiments. Finally, specific applications were designed, constructed and tested using the new phantom.

CHAPTER 1 INTRODUCTION

Advances in medical technology related to biomedical and radio frequency (RF) engineering have dominated the engineering and medical community, from magnetic resonance imaging (MRI) to implantable RF devices. These advances have led to ever increasing frequencies in the RF range and increasing signal to noise ratios (SNR). This work focused on the RF range around 900MHz where a saline phantom no longer accurately represented the human body. The need to have an accurate model of the human body for study at UHF frequencies is important for the development of RF devices which interact with the human body where RF power deposition is a limiting factor. While simulations can be done to estimate SAR, no comparative analysis between phantoms and simulations exist in the 900MHz range of the ISM band.

There are many important uses of RF energy including commercial, industrial and medical. In commercial settings, such as telecommunications, radio and television broadcasting are used for transmitting information. Non-communication devices, such as microwave ovens are used as convenience devices for cooking food. Applications for industry include industrial heaters and sealers that use RF energy to rapidly heat a food or material (in the same manner as a microwave oven cooks food) or other applications including sealing items such as processed food products or even attaching the sole of a shoe. Medical applications include things like magnetic resonance imaging (MRI), thermal ablation devices and devices under current development that include *in vivo* wireless communication systems.

An area of interest in the ISM band are Body Area Networks (BAN or Bodynets), Personal Area Networks (PAN) or Wireless Personal Area Networks (WPAN) [1-23].

Because this is a rapidly developing area, a standard nomenclature or standard has yet to be defined. Currently the Institute for Electrical and Electronics Engineers has a working group to define these issues under IEEE 802.15 and has labeled the technology as Wireless Personal Area Networks (WPAN) [24], which is how the technology will be defined in this document. WPAN are novel networks used in some very diverse applications to track human body interactions. These *in vivo* bio-communications systems can be applied as wearable, implantable or even ingestible and have applications ranging from game playing through the use of EEG signals, to physiological monitoring via implantable sensors and medication compliance through a ingestible pill that sends a signal indicating that the medication has been ingested. Development of these systems requires an accurate human body phantom model in order to fully understand the implementation and the limitations of WPAN by adding additional information which can confirm or disprove simulations.

Phantoms

The conductivity and permittivity of tissues change with frequency. Because the human body is heterogeneous, it is comprised of several different tissue types. Each tissue type has varying conductivity and permittivity; therefore some tissues will absorb more energy than others. Saline phantoms are homogeneous, and by nature only have one value of conductivity and permittivity. Biomedical Engineers require phantoms that emulate the human body at the frequency of interest in order to develop hardware to be used in and around the human body. It is fundamentally important aspect for the development of WPAN and other technologies involving transmission and reception of signals through the human body. Typically, containers of saline have been used to mimic this biological system [25]. However, as frequency increases, especially above

100MHz, saline phantoms fail as an accurate representation of the human body, because various materials behave differently as the frequency increases. At very high frequencies, the high dielectric constant of water causes the electrical wavelength to be severely shortened within the phantom [25-27]. This introduces excessive errors of the electromagnetic field distributions as it would apply to a biological system. It becomes necessary to take a new approach to phantom development, where the phantom that is used experimentally has the proper permittivity (often referred to as dielectric constant, loss tangent or dissipation factor) and conductivities to be equivalent to real tissues at the specified frequency of interest. The conductivity and permittivity of the human body has been well characterized from 10-6000MHz, therefore, once the frequency of interest is specified, the required permittivity and conductivity values can be identified [28-33]. A human body phantom can be constructed using various chemicals and materials that are combined together to alter the conductivity and dielectric constant at the frequency of interest. Examples of a few agents that can be used to modify the dielectric constant are acetone, isopropyl alcohol, sugars (sucrose, polysaccharides). The conductivity of the phantom is typically modified with salts or other conductive agents, such as aluminum powder. These phantoms can be constructed to any desired shape (i.e. conform to the anatomy of the human body), they can also be segmented to have different regions with varying permittivity and conductivity and may be liquid or solidified using a gelling agent such as TX-151 (Oil Center Research, Baton Rouge, LA) a polysaccharide that gels with water [25, 34]. It has been shown that 5% accuracy for these types of phantoms when compared to known permittivity and conductivity can be attained, which is mostly attributed to the accuracy of the dielectric probe [35-38].

Conductivity

Electrical conductivity (here forward referred to as conductivity) of a material is defined by how easily current flows through a material under the influence of an external electric field [39]. The conductivity (σ) is a ratio of the current density (\mathbf{J}) to the electric field strength (\mathbf{E}). Conductivity measurements are defined in the International System of Units (SI) and the units are Siemens per meter (S/m).

$$\mathbf{J} = \sigma \mathbf{E}$$

Conductivity is the inverse of electrical resistivity (ρ) (referred to resistivity in this work). Some important properties to note about conductivity as it relates to phantom development are that a conductor is a material that has a high conductivity and a low resistivity. An insulator has a low conductivity and a high resistivity. The conductivity of a phantom solution is directly dependent upon the amount of dissolved chemicals that ionize the mixture (typically a salt). Conductivity measurements are made at 25° Celsius (C) and an example of why that may be done is to test the “purity” of water, where the lower the conductivity (the higher the resistance or resistivity) the purer the water [28].

Permittivity

The permittivity of a material determines how an electromagnetic wave propagates through a material [39]. The dielectric constant also referred to as the complex relative permittivity is comprised of a real and imaginary part, where ϵ' is defined as the real part, which is known as the relative permittivity or the dielectric constant and ϵ'' is the imaginary part, known as the out of phase loss factor associated with the dielectric constant. It is interesting to note that by measuring ϵ' the relative permittivity of the

material and ϵ'' is the loss associated with introduced phase errors; the conductivity of a material can be derived from the using the ϵ'' [25].

$$\epsilon = \epsilon' - j \epsilon''$$

For this particular formula ϵ_0 is the permittivity of free space, and, ω , the angular frequency (which is $2\pi f$ is the frequency in Megahertz). Because of this, measurements of a material's permittivity and loss factor can be made and conductivity can be calculated resulting in a complete picture of a phantom's electrical characteristics.

$$\sigma = \epsilon'' \epsilon_0 \omega$$

Skin depth of biological samples: In the human body (and other biologic samples) the E field decreases exponentially, at the rate of approximately $e^{-z/\delta}$ where z is the distance into the body and δ is the skin depth where E-field decreases to $1/e$ ($=0.368$) of its value just inside the boundary. The RF depth penetration distance (d) is defined as how far the wave penetrates into the body before losing 50% of its initial value inside the boundary and is related to skin depth by $d = 0.693\delta$. The skin depth depends on the electric and magnetic properties of the material, and is a function of frequency (ω), where σ is the conductivity, ϵ is the permittivity, and μ is the permeability. However, the magnetic permeability of biological tissues is approximately equal to the permeability of free space [40].

$$\delta = \omega^{-1} \left[\frac{\mu\epsilon}{2} \left(\sqrt{1 + \left(\frac{\sigma}{\omega\epsilon} \right)^2} - 1 \right) \right]^{-\frac{1}{2}}$$

Measurement of Conductivity and Permittivity in the Radio Frequency Range

Typical dielectric measurements of a material are conducted using a coaxial probe, vector network analyzer and controlling software. A coaxial probe structure can

measure the complex permittivity of a wide range of semi-solid, pliable solid and liquid materials. The software provides all the necessary control of the network analyzer to measure the complex reflection coefficient of the material under test (MUT). The complex reflection coefficient is then converted into the complex permittivity ϵ' and ϵ'' . The use of a computer controlled dielectric probe and network analyzer provides a convenient and reliable method for measuring dielectric materials [35]. The ease of measuring materials is done by pressing or immersing the probe against the material being tested. Although this simplifies the measurement, there are many practical steps that need to be taken to ensure reliable measurements. They include items such as proper calibrations; have a test material of known property and ensuring proper placement of the probe, making proper contact with the probe for a good measurement (even contact, no air space, etc...).

Radio Frequency Fields

The electromagnetic spectrum contains all modes electromagnetic energy in the form of radiation. There are many types of radiation including visible light, x rays, gamma rays, infrared waves and radio frequency waves. These waves of electric and magnetic energy oscillate at the same frequency, propagating through space at the speed of light. RF energy emitted by a transmitting antenna is one form of electromagnetic energy [41, 42].

It is important to note the RF wave has two components, the electric and a magnetic field and there are two different units, one for each type that describe the signal amplitude at a specific location. Electric field strength is defined in the unit "volts per meter" (V/m) and Magnetic field strength is defined in "amperes per meter" (A/m).

In a vacuum, where RF (or EM) waves travel at the speed of light, they can be characterized by a wavelength and a frequency utilizing the formula listed below.

$$\lambda = c/f.$$

The wavelength (λ) is the distance that the wave travels in one complete cycle of the RF wave, and the frequency is defined by how many RF waves passing a given point in one second. The frequency of an RF signal is usually expressed in terms of a unit called the hertz (Hz), where one Hz equals one cycle per second and one megahertz (MHz) equals one million cycles per second.[39] As defined by the IEEE standard, C95.1-2005, the radio frequency section of the electromagnetic spectrum is defined as frequencies in the range of about 3 kilohertz (3 kHz) to 300 gigahertz (300 GHz) [24].

Generally, research studies have shown that environmental levels of RF radiation that is encountered by the public is typically way below levels necessary to produce significant heating or increased body temperature. However, there have been studies to examine the possibility of a link between RF and microwave exposure and cancer. Many of these results have been conflicting and inconclusive [43, 44]. Under certain controlled conditions, it has been shown that tumor formation in animals can occur from RF exposure; however, these results have not been independently replicated. In 1996, the World Health Organization (WHO) embarked on a literature review called the International Electromagnetic Fields (EMF) project to review existing knowledge on biological effects and identify gaps that need to be filled by research and work toward an international standard on RF exposure limits and the WHO maintains a website (<http://www.who.int/peh-emf/en/>) to disseminate information [43].

Although general environments have been deemed at low risk for reaching exposure limits, workplace environments that are near high-powered RF sources, where recommended safety limits could be exceeded need to be monitored [24]. In such instances, restrictions can be employed in order to safely utilize the RF non-ionizing radiation.

Experiments that utilize RF energy have the potential to cause RF heating in tissues, especially when the body part is near the RF source or in a high power transmission path. There are many factors involved with tissue and heating, they are related to the conductivity, permittivity and the body's natural ability to expel excess heat (through circulation and physiologic functions). In particular, there are two areas of the body that are extremely vulnerable to RF heating. Heating can occur in the eyes and testes because there is insufficient blood flow to dissipate the excessive heat load that exists in these areas. Low level RF exposure (i.e. no tissue heating occurs) lacks significant evidence for harmful biological effects is ambiguous and unproven [44]. The human body has the most sophisticated response to a thermal input, whereas other mammals, such as rats are really poor indicators to how the human body will react to a thermal stress [26, 45]. This is not to say the information is useless, the knowledge gained from studying rats and other rodents can provide significant information about biological systems, it will just not be an accurate representation of the human body.

An important aspect of heat dissipation in the human body is the health of the individual. The ability to tolerate RF heating is a causal effect related to the health of the subject. Primary factors can be the patients overall health with factors such as cardiovascular conditioning, obesity and types of medications that a subject is on can all

change the thermoregulatory response to an applied RF source. The size of the current loop along with the biological factors determines the impact of the heating. It is well known that localized heating occurs, but the question is how much and is there any tissue damage caused by the heating? The body temperature of a healthy human being is 37 °C, but the highest core temperature that is still safe is 39.4 °C. The pain threshold for skin contact is 43 °C and proteins break down at 45 °C. This small range of temperatures becomes important when any amount of RF is transmitted into the human body. The potential for localized heating and tissue damage increases as frequency goes up and the human body becomes a significant portion of a wavelength of the excitation frequency [46].

Current Standards

There are two categories of radiation, ionizing and non-ionizing. Radiation that ionizes has sufficient energy to convert an atom or a molecule into an ion. This occurs when there is sufficient energy to add or remove a charged particle such as an electron or other ion. However, radio frequency fields fall into the category of non-ionizing radiation since the electromagnetic fields create by electrical communication and biomedical devices are insufficient to ionize molecules, but they are sufficient enough to cause thermal heating. This is quantified through a measurement called specific absorption rate (SAR) which is the thermal energy absorbed over a small mass of material and is expressed in the units of watts per kilogram (W/kg). Maximum SAR can be induced when the transmitted RF is in the range of about 80 and 100 MHz (where the body can be a resonant structure) and because of the resonance phenomena, stricter RF safety standards are required in this frequency range.[24, 26, 28, 47, 48]

Another effect, which happens below 100 kHz is electro-stimulation and this must also be accounted for where applicable [24].

The effects of radio frequency transmissions are evaluated by the Federal Communications Commission (FCC) as federally mandated by the National Environmental Policy Act of 1969. Controlled environments are those where RF energy is contained by a Faraday cage such as a Magnetic Resonance Imaging (MRI) system or industrial settings where access to high power RF transmission are limited and safety standards are in place. However, at the present time there are no federally mandated radio frequency exposure standards, but there are several non-government organizations, mostly international, that have issued recommendations for human exposure to electromagnetic fields. Europe and many other countries employ exposure guidelines developed by the International Non-Ionizing Radiation Protection Committee of the International Radiation Protection Association (INIRC-IRPA).[49] The INIRC-IRPA has set safety limits are similar to those of the NCRP and IEEE, albeit with a few exceptions [50].

INIRC-IRPA

The International Non-Ionizing Radiation Committee of the International Radiation Protection Association (INIRC-IRPA) is an international organization that provided a universal direction for various instances on non-ionizing radiation. The guidelines are based on the assumption of far-field radiation and make no provisions for the near-field [49]. Far-field radiation becomes well behaved after approximately one wavelength away from the antenna. In this case, the electric and magnetic fields are orthogonal to each other and the direction of propagation. Because the fields are predictable, power density calculations can be made using either electric or magnetic

field measurements. However, in the near-field case, especially in the area close to the antenna, the E and H fields are not perpendicular to each other and there is a reactive field caused by the inductive or capacitive storage energy of the antenna. This reactive field does not propagate far from the antenna, but it can still interact with tissues within its sphere of influence. This complicates the power density calculations as they must now include both the electric and magnetic fields.

NCRP

The National Council on Radiation Protection and Measurements (NCRP) produced a report in 1981, Scientific Committee 39, Report 67 titled *Radiofrequency Electromagnetic Fields: Properties, Quantities and Units, Biophysical Interaction, and Measurements*. NCRP Report No. 67 is a report non-ionizing radiation defining the quantities and units for measurement techniques. Additionally, biological effects and exposure criteria were defined for interactions with radio frequency electromagnetic fields to provide radiation protection. The report started to define the exposure limits for non-ionizing radiation and make a connection to ionizing radiation by defining fundamental quantities and units [51]. Report No. 67 is the primary source that the ANSI C95.1-1982 and subsequent revisions IEEE Std.C95.1-1992 and 2005 are based, which concluded that there is little possibility of measuring the absorption of radio frequency energy at the cellular level.

IEEE

The Institute for Electrical and Electronics Engineers (IEEE) Std C95.1-2005 provides exposure recommendations for electromagnetic fields in the radio frequency range of 3 kHz to 300 GHz to protect humans from the harmful effects these fields could invoke if used improperly. The recommendations apply to controlled environments and

the general population, but are not designed to regulate devices being used under the direction of professional medical personnel. This standard covers two types of possible adverse events; they are electro-stimulation and tissue heating. Electro-stimulation can be painful or even fatal (stopping the heart); therefore boundaries are set for signals below 100 kHz where electro-stimulation occurs. Tissue heating is defined to occur at above 100 kHz and while there can be a sensation of heating; it does not necessarily imply tissue damage and this standard does not propose a standard for thermal sensation. However, it does set limits based on frequency, amplitude and time. In the region of 100 kHz to 5MHz, guidelines for both electro-stimulation and tissue heating must be adhered to [24]. Because the standards vary greatly based on frequency and class (controlled versus general), specific standards will be discussed when directly applicable to this research.

Guidelines Summary

These recommendations directly address the standards for electro-stimulation, maximum permissible RF exposure and SAR. Electro-stimulation is specifically covered in the IEEE standard C95.1-2005 and also covers tissue heating which is directly related to SAR. SAR in the human body when the transmitter is in close proximity to the human body can be simulated. While these standards have not taken into account the transmitter being inside the human body they are still applicable to WPAN and *in vivo* bio-communications. Essentially all the standards are in agreement, the assumption is mainly for far field effects where the E and H fields are perpendicular to one another. However, in the human body, the complex permittivity changes the phase relationship between the electromagnetic waves, which allows for local hotspots [24]. There have been various organizations and countries that have developed RF radiation exposure

standards. In general these standards recommend the exposure levels for the general public and workplace, assuming far field radiation. Since 1985 the FCC has recognized safety guidelines for evaluating exposure to an RF environment. However, there are several federal safety agencies that have taken a vested interest in monitoring and investigating issues related to RF exposure. The list of these agencies includes but may not be limited to the Food and Drug Administration (FDA) [52], the National Institute for Occupational Safety and Health (NIOSH)[53], the Occupational Safety and Health Administration (OSHA) [54] and the Environmental Protection Agency (EPA) [55]. The FCC has adopted the recommendations of the National Council on Radiation Protection and Measurements (NCRP) advisory council on non-ionizing radiation and has settled on the standard of the ANSI/IEEE C95.1-2005 guidelines and this is documented in the FCC report FCC 96-326.[50] NCRP exposure criteria and the IEEE standard were implemented after extensive reviews of the scientific literature related to RF biological effects by expert engineers and scientists working in the field. These exposure guidelines are based on thresholds for known adverse effects, and they incorporate appropriate margins of safety. Therefore this research will be evaluated based on the IEEE 95.1-2005 standard.

Maximum Permissible Exposure

IEEE 95.1-2005 standard discusses maximum permissible exposures (MPEs), however, this is another method for defining SAR using the far field assumptions and power density in watts per meter squared (W/m^2), therefore it will be discussed more thoroughly in the next section on specific absorption rate. This next section will cover both far field and near field assumptions for SAR thus defining the role of phantom

studies and correlation to simulations for providing proof of compliance to recommended safety guidelines when developing new devices.

Specific Absorption Rate

Specific absorption rate, by definition is the measure of the rate at which radio frequency energy is absorbed or dissipated in the body. SAR is the “time derivative of the incremental energy (dW) absorbed by, or dissipated in an incremental mass (dm) contained in a volume element (dV) of a given density [51]. This is shown in mathematical form below:

$$\text{SAR} = d/dt (dW/dm) = d/dt [dW/\rho (dV)] \text{ [W/kg]}$$

The NCRP, INIRC-IRPA, and ANSI/ IEEE exposure guidelines state the threshold level at which harmful biological effects may occur, and the values for maximum permissible exposure (MPE) recommended for electric and magnetic field strength and power density in both documents are based on this threshold level. The threshold level is a SAR value for the whole body of 4 watts per kilogram (4 W/kg) averaged over any 15 minute period. The most restrictive limits on whole-body exposure are in the frequency range of 30-300 MHz where the RF energy is absorbed most efficiently when the whole body is exposed. For devices that only expose part of the body, such as mobile phones, different exposure limits are specified. Since placement of a device on or in the human body is crucial to the evaluation, this research will look at specific body locations to determine SAR and general safety of proposed devices. However, it is not realistic to measure the energy that is deposited within a unit of tissue, but other characteristics can be measured and SAR can be inferred. The power deposition can be calculated in the human body when the characteristics, which are the conductivity and relative permittivity of the target tissue, are known. As stated by IEEE Standard

C95.1-2005, the electromagnetic field contains two parts, the electric and the magnetic field. The equivalent power density equation can be used when of the fields is known.

$$\text{SAR} = \sigma / 2\rho (|E|^2)$$

Where σ = tissue conductivity (S/m)

ρ = tissue density (kg/m³)

E = rms electric field strength in tissue (V/m)

SAR will be discussed as it applies to two conditions, using Poynting vector theorem using far field assumptions and then transitioning to near field assumptions.

SAR with Far Field Assumptions

Poynting vector theorem named after its inventor John Henry Poynting and independently co-discovered by Oliver Heaviside, describes the energy flux (power or density in W/m²) of a uniform plane wave that makes up an electromagnetic field [42]. The electromagnetic field is composed of two parts, the electric (E) and the magnetic field (H), and they are directly related to the current density (P).

$$P = E \times H$$

Poynting's vector is the cross product between the electric and magnetic field measurements. The units of watts per area come from the instantaneous power density where:

$$P = E \text{ (V/m)} \times H \text{ (A/m)} = E \times H \text{ (W/m}^2\text{)}$$

However, SAR is typically defined with far field assumptions, where in the far field the electric and magnetic fields are 90° apart and the intrinsic impedance (η) is defined as the square root of the ratio of permeability (μ) to permittivity (ϵ).

$$\eta = \sqrt{\frac{\text{permeability}}{\text{permittivity}}}$$

Therefore, when the intrinsic impedance is considered a perfect dielectric, as is the far field, the intrinsic impedance is defined as a ratio between the electric and magnetic fields.

$$\eta = E/H$$

This identity coupled with averaging the Poynting, allows the magnetic field component of the Poynting to be removed.

$$P = E^2/2 \eta$$

The human body is not a perfect conductor; it is actually a dielectric that has associated losses and conductivity, therefore the intrinsic impedance is a complex value. However, because of this complexity the NCRP Report 67 further simplifies the intrinsic impedance by assuming that the target tissue is a good conductor. The rationale for this is that the larger ratio of the conduction current, σ , to the displacement current $\omega\epsilon$, the closer the tissue is to a good conductor. In a good conductor, the electric and magnetic fields have a phase difference equal to or approximately equal to 90 degrees. This supports the previous assumption where the magnetic field component was removed from the Poynting vector. This is easily validated by calculating the phase relationship for a target tissue where $\sigma \gg \omega\epsilon$.

$$\tan^{-1}(\sigma/\omega\epsilon) \cong 90^\circ$$

The reasoning behind this assumption is that tissues of interest for SAR calculations are mainly composed of water, for areas such as muscle and organs in the torso. Other areas of the body that contain high concentrations of adipose tissue or contain large bones with a low water content compared to muscle tissues, then the conduction and displacement currents are closer. However the standard development

of the SAR equation assumes a tissue with high water content as these are areas of the body that control processes and damage could be severe. SAR is based on average power per mass of the target tissue; therefore average power must be defined [24, 49-51].

$$\text{Average power} = (\sigma\delta E^2 e^{-2d/\delta} \times A)/2$$

Therefore, the SAR is simply the average power divided by the mass.

$$\text{SAR} = \text{average power/mass}$$

Now if the average power is substituted in and the mass is equivalent to the tissue density times the volume, the equations becomes:

$$\text{SAR} = (\sigma\delta E^2 e^{-2d/\delta} \times A)/2 \rho \times \text{volume}$$

This equation can then be simplified by defining the volume of interest to an area, A, down to one skin depth, δ . The power than is assigned to begin at the skin's surface ($d=0$). The equation now becomes the SAR equation defined at the beginning of this chapter.

$$\text{SAR} = \sigma/2\rho (|E|^2)$$

Discussion of the Far Field Assumptions

Because of the applications for *in vivo* bio-communications can apply fields to the human body in the near field, it is appropriate to discuss how the far field assumptions can be applied to this work. Two assumptions were made when calculating SAR, the first being that tissue of interest was in the far field and second, that it was a good conductor.

The far field region initiates a finite distance from the antenna and as long as the transmit and receive antenna are a sufficient distance apart then the far field begins at a finite distance away from the antenna defined below [42].

$$R=2D^2/\lambda. ,$$

Where R = Range length (the separation between the transmit and receive antennas)

D = the aperture of the antenna under test

λ = the measurement wavelength

In the far field the power density, which is defined by the electric and magnetic field strengths are orthogonal to each other and one parameter can define the others.

$$P = E \times H = E^2/120\pi = 120\pi H^2$$

Where P is expressed in terms of W/m²

E in V/m

H in A/m

The area between the antenna and the far field defines the near field. At higher frequencies, i.e. 902-928MHz of the ISM band, the near reactive field is contained in a $\lambda/2\pi$ sphere which is approximately equal to 5.22 cm at 915MHz [42, 56]. The energy from these fields can be inductive or capacitive and affect the magnetic and electric fields. Generally, the near reactive field extends from the antenna to about one wavelength away ~30cm for 900MHz. This field is non-radiating, but also falls off with distance; however, it does not have the plane wave characteristics for the electric and magnetic fields that are associated with far field radiation. No relative assumptions can be made to characterize various parameters and because of this the far field assumptions may be invalid at certain tissue depths. Only general guidance for near field exposures is available relating to hot spots.

The second assumption made relating to SAR was that human tissue is a good conductor. Fat and bone are known not to be good conductors and can cause dispersion in phase between the electric and magnetic fields, however, muscle and

organ tissue which is the main thrust of these experiments have much higher water content and are therefore a much better conductor. Since the phantom is mainly constructed of a “good conductor”, i.e. water based gel containing the proper salt content to achieve the correct conductivity; the phantom does indeed behave as a good conductor.

Because the near reactive field is complex and the fields may not necessarily be far field, experiments in utilizing a finite difference time domain simulation, along with calorimetric measurements in the phantom will be used to determine the validity of the assumptions.

CHAPTER 2 REVIEW OF THE STATE OF THE ART

Objective

Since the fundamental theme of this work is providing a phantom of the human body that can be used by Biomedical Engineers at a specific, relatively narrow band of frequencies, it is important to define the earlier work, thereby showing the importance of this phantom work. Specific Absorption Rate (SAR) is a common theme when dealing with radio frequency fields. A more accurate definition for SAR can be defined as that takes into account the complex permittivity along with the conductivity is:

$$\text{SAR} = (\sigma + \omega \epsilon_0 \epsilon'') E_{\text{rms}}^2 / \rho \text{ watts/kilogram (W/kg)}$$

Where σ is the conductivity

ω is the frequency in radians / second

ϵ_0 is the relative permittivity of free space

ϵ'' is the relative permittivity of the material of interest

E_{rms}^2 is the magnitude of the E field at that point

ρ is the mass density in kg/m^3

Now that the definition of SAR equation has been shown it is important to realize how a phantom can be developed. This relies on a series of previously published works that will be reviewed over the next couple of sections, thus defining why the proper phantom must be used in the development of SAR. SAR varies directly with σ and ϵ'' , [47] therefore a model that has the proper size, geometry, conductive and dielectric properties is required to ensure device safety [45]. A quick review of the basic formulas that were used when trying to achieve the proper conductivity and permittivity, followed by an extensive review of “state of the Art” phantom technologies, their advantages, disadvantages and why a new segmented phantom need to be constructed.

Debye Formula and Cole-Cole Modification for Complex Permittivity

The basic foundations for measurements of permittivity in a sample revolve around the theoretical approximations proposed in 1929 by Debye [57] and the subsequent modifications to the formulas which adapted it to real world conditions by Cole and Cole in 1941[58].

The relative permittivity of a material can be defined by the Debye relaxation equation. This equation is used to determine the response of a system to a periodically changing external electric field (i.e. an oscillating field). In this case, relaxation means equilibrium. So in the Debye relaxation equation the time parameter 'tau' is simply the characteristic time for the system to come to equilibrium, the 'omega' is the frequency of the oscillating field, and the different values of 'epsilon' represent the low and high frequency limits of the permittivity. On a more practical note, the equation attempts to model the dielectric response of a system of ideal non-interacting dipoles to an external field. In other words, how does this system of dipoles change (in terms of its permittivity) in the presence of an oscillating electric field with frequency 'omega'?

$$\hat{\epsilon}(\omega) = \epsilon_{\infty} + \frac{\Delta\epsilon}{1 + i\omega\tau},$$

where ϵ_{∞} is the permittivity at the high frequency limit, $\Delta\epsilon = \epsilon_s - \epsilon_{\infty}$ where ϵ_s is the static, low frequency permittivity, and τ is the characteristic relaxation time of the medium.[57]

Since the Debye equation is an approximation, it was found to have errors associated with it for real world conditions. Therefore in 1941, Cole and Cole modified the formula via empirical data based on the Debye equation. In this equation, the parameter 'alpha' is included to take into account the special case in which the permittivity is symmetric with respect to the applied frequency of the electric field [58].

$$\hat{\epsilon}(\omega) = \epsilon_{\infty} + \frac{\Delta\epsilon}{1 + (i\omega\tau)^{\alpha}}$$

Use of Coaxial Probes for Measuring Permittivity

An area of interest that coincides well with phantom research is that of finding non-destructive broadband methods for measuring the permittivity of biomaterials at RF. One such method that fits this requirement is the use of open-ended coaxial lines as “dielectric probes”, which actually measure reflection coefficient which can be converted to permittivity and loss tangent. Because of this, conductivity can also be calculated giving a complete electrical specification of the material measured. Rigorous work has been applied to understanding and using open-ended reflection methods for permittivity measurements of materials [32, 33, 35-38]. This probe has been shown to have the most positive benefits for the study of permittivity of phantoms, excised and *in vivo* tissue samples. The probe should have several properties that make it suitable for making measurements, they include the ability to operate over a wide range of frequencies, have an optimum minimum capacitance ($\ll 1\text{pF}$), which introduces the least amount of error for ϵ' and ϵ'' , having a reasonable size, compared to the object being measured and be compatible with several forms of material (i.e. liquid, semi-liquid and solid samples) [32]. Dielectric probes are commercially available, which in turns allows the focus to remain on making the measurements related to phantoms. Although commercially available, a few concerns about the probe, computer and network analyzer must be discussed in order to have assurance of the measurement of materials used in the construction of phantoms for RF dosimetry studies. There are several pieces of equipment that when combined together make a measuring system used to quantify the reflection coefficient which is then used to calculate the dielectric

constant (ϵ') and the loss tangent (ϵ''), from this measurement a calculation to obtain the conductivity can be made. The equipment to be used in these experiments is a Hewlett-Packard (HP) 85070C dielectric probe, the next item used is an HP8752A vector network analyzer, and the final piece of equipment was a Dell Latitude 600 with the HP software to interface with the network analyzer and probe and perform all controlling functions and calculations based on its internal model.

HP85070C Dielectric Probe

The HP dielectric probe has a nominal frequency range of 200MHz to 20GHz; it works in the temperature range of -40°C to $+200^{\circ}\text{C}$, allowing measurements to be made in various environments. The probe makes certain assumptions that must be followed in order to obtain accurate results. The materials that are tested must be $>20\text{mm}$ in diameter, be non-magnetic, homogeneous and have a smooth surface that does not have gaps when interfaced to the probe. When these conditions are met, this probe is specified to have an accuracy of $\pm 5\%$ range on the measurements with repeatability and resolution that is two to four times greater than the accuracy.

8752A Vector Network Analyzer

The network analyzer chosen for making the reflection measurements in these experiments is the HP8752A. The important parameters for making measurements of phantom materials in combination with the dielectric probe are the noise source variation of $.00006\text{dB}$ and source variation of 0.1dB , however when compared to the accuracy of $.05$ to $.15\text{dB}$ errors associated with the probe calibration, the overall contribution to the errors from the network analyzer are insignificant.

Computer and Software

The computer system used is more or less irrelevant as long it meets the minimum required specifications of 4MB of random access memory (RAM), a 20 megabyte (MB) hard drive, video graphics adapter (VGA) capable video and Windows operating system. The Dell latitude 600 computer that was used was more than sufficient for the application with 1GB of RAM, a 40 gigabyte (GB) hard drive, super video graphics adapter (SVGA) and Windows XP.

The computer is specifically used for taking the reflection coefficient measurement from the network analyzer and used to calculate the permittivity because the permittivity is not measured but calculated based on a model software model provided with the dielectric probe. The software program for the HP85070C is a Windows based application

Uncertainty of the Measurement

The world in which we do research is imperfect; however in this particular case the uncertainty is definable. The largest deviation in accuracy is the probe itself, which is shown to have the greatest error of 3-5%. The effect of the dielectric error can be calculated using the following formula.

$$E = S_m/S_c \times D$$

E is the measurement error (delta permittivity)

S_m is the sensitivity of the material measured

S_c is the sensitivity of the calibration standard

D is the delta uncertainty used in the calibration

This information confirms the validity of the measurements allowing the researcher to be confident of the results within 5%. However, it is known that typically relative

measurements are more accurate than absolute measurements. Therefore, it is important to check the calibration often to ensure nothing in the setup measurement has changed. Also multiple measurements of each material need to be made in succession in order to make sure good contact interface between the materials under test (MUT) to ensure an accurate measurement. Once a material's permittivity is measured, it should also be confirmed later as an added protection of the results.

Phantoms Characteristics

Several types of phantoms have been used to mimic the human body for various RF applications; this section will cover the various types of phantoms used and discuss their advantages and disadvantages. Many phantoms do not take into account changing the dielectric constant of the phantom. This review will compare and contrast the various reasons for not accounting for the permittivity of a phantom. In all cases it may not be necessary to completely replicate the human body, especially in the case of low frequency applications. From a geometric perspective most phantoms do not accurately represent the human body. While geometrically accurate phantoms do exist, they are not common place in research, instead plastic bottles or other containers that are not an accurate representation are typically used. The rationale for this section is to determine which type of phantom in current use would be best used for high frequency applications. These include WPAN and ultra high static magnetic field MRI systems which result in an ultra high radio frequency (UHF) as well as any other human applications operating in the very high frequency (VHF) to UHF. However, current technology for phantoms does not accurately facilitate dosimetry measurements, and then a new method needs to be proposed along with the rationale for employing this new strategy for phantom development.

Saline Phantoms

There are great number of biomedical related RF studies over 100 MHz that use saline phantoms for RF studies, the concentrations range from .45% to .9% to mimic the physiologic properties of the human body. While below 100MHz, this may be accurate[59], at high frequencies, especially those that are large electrical dimensions, (i.e. approaching an electrical wavelength) and are much greater than 100MHz in frequency, the inaccuracies from the dielectric constant become a serious liability on the accuracy of the results. Typically when these phantoms are designed, the proper conductivity is found and utilized, while completely ignoring the permittivity aspects of the phantom which are around 80, which is typically much higher value than human tissues have at frequencies above 100MHz. Studies that utilize saline phantoms have many different applications including specifically, but not limited to: electron spin resonance (ESR) Magnetic Resonance Imaging, (MRI), microwave thermal imaging, intra-body communications [59] and many others that have a need for phantoms that have the proper electrical characteristics of the biological system being studied.

It has been determined by ESR measurements at 300, 700, and 900MHz that a “decrease in dielectric loss dominates over the signal reduction” which is not adequately represented by the high dielectric constant of saline. Another application used a .9% saline phantom to evaluate the near field of a microwave based imaging system and while this particular study did not address the effects of the dielectric constant, the model was still not accurate based on the fact the system was working in the 300-900MHz range.

Even MRI for the most part uses saline phantoms, but the consequences are well known and some adaptations have been made by using non-electrical loading

phantoms (i.e. doping the phantom with silicone oil) or the use of gel phantoms with corrected permittivity and conductivity values [25].

Tissue Equivalent Phantoms

Tissue equivalent phantoms are defined as those phantoms that attempt to have the proper permittivity and conductivity to mimic the biological region of interest. Typically this is done with distilled water that has no conductivity and dielectric constant around 80 across most frequencies ranges, salt (NaCl) to modify conductivity and a form of sugar such as sucrose to modify permittivity. These phantoms are typically liquid, homogeneous, estimate the bulk loading of the tissue in question and cannot represent various tissue types in a single phantom [60]. A clear example of a homogeneous tissue equivalent phantom is the specific anthropomorphic mannequin (SAM) which is used in the cellular telephone industry for calculating SAR. An advanced type of this phantom was reported by Ogawa [61] which described the need for a geometrically accurate phantom with complex permittivity. However, in the United States, the Cellular Telecommunication Industry Association (CTIA) which certifies cell phones, uses a geometrically correct, albeit a homogenous phantom even though it is common knowledge that in the human head is heterogeneous. The eyes are much more susceptible to heating versus other areas of the head, even in this limited case; it demonstrates the need for a segmented tissue equivalent phantom.

Segmented Tissue Equivalent Phantoms

While segmented phantoms that have the proper density for assessing the dosimetry in x-ray based modalities are common place and commercially available, they are virtually non-existent in the radiofrequency range. X-ray dosimetry phantoms typically consist of anatomically accurate, segmented materials of different densities to

accurately simulate human tissue at the x-ray frequencies [62, 63]. In the radio frequency range, there is a paper that covers a segmented tissue equivalent phantom [25], and while it is an excellent start to making a true tissue equivalent phantom, it has several flaws that needed to be pointed out. This particular phantom was for emulating rats for use in a very high frequency MRI system (470MHz) and while the target tissues were successfully obtained, the actual distribution of the segments are not in an optimized arrangement to emulate the actual tissue loading of a rat. In this case, this was a proof of concept, but there are many improvements upon this rudimentary phantom that can be made, especially when dealing with a geometrically large subject such as the human torso. This particular phantom for rats utilized four separate compartments, where the first compartment was an elliptical brain segment, followed longitudinally by a “large” muscle segment, followed an average abdomen segment and lastly containing a smaller muscle segment. The segments were also separated by large approximately quarter inch layer of wax, which is not representative of tissue. It is easy to see from this description that the tissues were placed in longitudinally which in actuality tissue segments are generally concentric, with skin, followed by fat, then muscle and finally the organs. A review of the software human body model and general human anatomy coupled with subsequent simulations will be compared to an anatomically correct phantom.

CHAPTER 3 ANTENNA SIMULATIONS

A growing international phenomenon is the increasing interest in wireless medical implants, telemetry devices, Magnetic Resonance Imaging (MRI) and other radio frequency applications that use the human body as a medium of propagation. In the United State, this growing demand for biomedical applications has prompted the FCC to allocate specific frequency bands for use with medical devices. Some examples of the allocated bands are, 402 to 405MHz for Medical Implant Communications Service (MICS) band, the 608 to 614 MHz for Wireless Medical Telemetry Service (WMTS) band, and the 902-928MHz, 2.4-2.483GHz and 5.725-5.825GHz Industrial-Scientific-Medical (ISM) bands. MRI frequencies have typical frequencies that are associated with the static magnetic field strength and overlap some of the other wireless bands. Some of these include research systems at approximately 400MHz or 9.4T, but the research MRI frequency of interest is 900MHz or 21T which happens to coincide with the ISM 902-928MHz region of interest. In order to evaluate the field distributions of antennas that are loaded by the human body and the associated SAR effects due to the close proximity of the transmitted power in the above FCC regulated frequency bands, we employed the finite difference time domain (FDTD) method in the 900MHz region. For the analysis, a folded dipole antenna with large bandwidth was simulated and a 45 mm surface coil for MRI applications, each was tuned to the desired frequency of interest and the near- and far-field behavior was characterized as it relates to SAR. Modeling antennas utilizing the human body as part of the environment is possible using a various commercially available program.

Computational Method for Solving Maxwell's Equations

Solving Maxwell's equations will be used to define the radiation patterns of antennas associated with the human body. Subsequently potential hotspots will be identified and localized tissue heating caused by SAR of an antenna can be viewed. In this case a folded dipole and a small MRI surface coil were studied. We must first find the Vector Potential \vec{A} ; this can be done using differential form of Maxwell's equations:

Gauss' Law for Electricity

$$\nabla \cdot \mathbf{D} = \rho$$

Gauss' Law of Magnetism

$$\nabla \cdot \mathbf{B} = 0$$

Faraday's Law of Induction

$$\nabla \times \mathbf{E} = -\frac{\partial \mathbf{B}}{\partial t}$$

Ampere's Law

$$\nabla \times \mathbf{H} = \mathbf{J} + \frac{\partial \mathbf{D}}{\partial t}$$

Where $\nabla \cdot$ is the divergence (per meter), $\nabla \times$ is the curl (per meter), ρ is the charge density in coulombs per cubic meter, \mathbf{E} is the electric field in volts per meter (or equivalently, Newton per coulomb), \mathbf{H} is the magnetic field in ampere per meter, \mathbf{D} is the electric displacement field (in coulomb per square meter) and is also known as the flux density, \mathbf{J} is the free current density (in ampere per square meter).

From the above equations it can be shown that the vector potential \vec{A} is found when solving a triple integral, which represents a volume in space. That equation is:

$$\vec{A} = \iiint \mathbf{J} e^{-jkR} \text{ where } k=2\pi/\lambda$$

The derivation of the equation shown above can be found in antenna, electromagnetic and microwave engineering texts [64], so the derivation of this equation has been defined and is omitted. The next step is to use the vector potential \vec{A} to find

the far field radiation of an electrically small dipole antenna through the use of a finite difference time domain (FDTD) simulation program.

The use of the Finite difference time domain method [52] is an accepted form to solve problems involving the interaction between electromagnetic waves and complex structures such as the human body. The simulated structure is segmented into box-shaped cells, which are small compared with the wavelength; this technique uses a grid-based time domain numerical method. Each cell is evaluated using time-dependent Maxwell's equations in partial differential form. It approximates the corresponding discrete forms and the ensuing difference equations are solved to obtain the spatial electrical and magnetic vectors at each time step. This represents the time needed for electromagnetic waves to travel from one cell to the next cell and the calculation continues until a state of convergence is obtained.

The benefit of using FDTD method over other simulation methods is its excellent scaling ability as the problem complexity increases. This is because as the number of variables multiplies, due to the increased structure size, the efficiency of this method outperforms the vast majority of other simulation methods. Another important feature related to the time domain nature, when compared to most frequency domain simulation methods, is that the FDTD method can obtain a broad band solution from a single broad-band excitation such as a time domain pulse. This gives a quick and accurate solution over a very large frequency band.

Description of the Simulation Setup and Parameters

The program chosen to do the simulations was REMCOM, which has a human body model and is widely used in industry and academia [65-69]. The first step is to open the program and start a geometry file. In the geometry file it is important to select

a cell size, however, having the best resolution results in slow running simulations. It is therefore important to balance the resolution of the mesh to get the required results without taking too much time for the simulation. Once the geometry is drawn, it is important to “pad” the boundaries, in this with air. This allows the program to converge, which brings us to some more parameters options of setting the convergence threshold in REMCOM (-30dB for simulations running in air, -16dB for simulations running with the human body model) and setting the number of time steps, which I set to 10,000 to help the program run faster. Initial studies were done using a $\lambda/2$ dipole for approximately 915MHz, center of the ISM band spanning from 902-928MHz. Once the solid geometry is drawn or imported from another computer aided drawing program (CAD), it must be converted to a wire mesh and add sources (passive- capacitors or inductors, active- signal generator). For the standard dipole an active series voltage source; no matching was required and the dipole was connected to the 50 Ohm source. After the setup of a regular dipole, a folded dipole configuration was used with the human body model.

Dipole in air

A $\lambda/2$ dipole, shown in Figure 3-1, resonating at 915 MHz in air was simulated to confirm the radiation pattern shown in most antenna engineering texts. Because the dipole is a simple structure it was drawn directly in REMCOM, and the structure was meshed. A narrow Gaussian shaped pulse was applied for tuning and Liao boundaries were used. Liao absorbing boundary conditions [53] are used in the simulation instead of the perfect matched layer (PML) boundary conditions when simulating in air as a medium. In this case, the boundary conditions only allow electrical waves to travel outward of the simulation space, however the PML increases the simulation space

because additional defined padding, which is composed of artificial absorbing materials at the outer boundary.

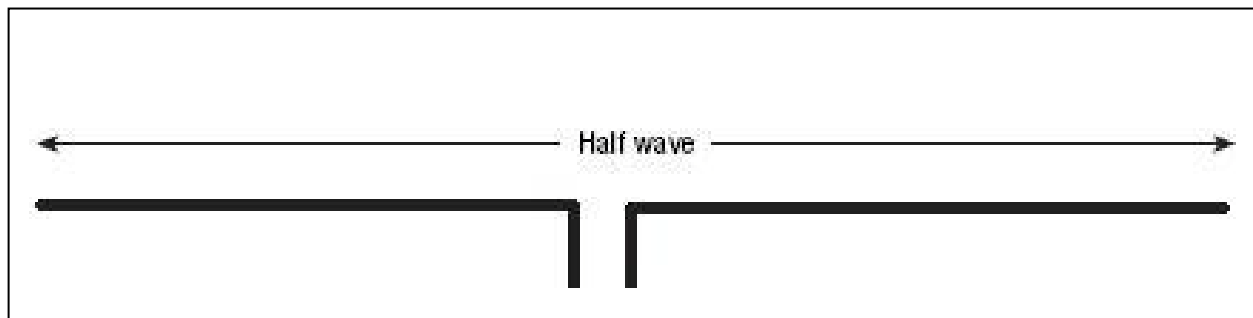


Figure 3-1. A $\lambda/2$ dipole with a total length of approximately 32.4 cm and each segment being approximately 8.2 cm. A source 50 Ohm source is placed between the two vertical sections, matching is not required on the dipole antenna allowing quick and easy simulations in air to confirm the simulation with known theory.

Because additional padding is not necessary with the Liao boundary, simulation time can be reduced, because the simulation space is smaller. Initially, the resonant frequency and input impedance (S_{11}) was first determined over a broad frequency range using a narrow Gaussian-shaped pulse. The antenna was tuned by trimming the antenna length until resonance at the frequency of interest (915 MHz) was obtained. After achieving the correct resonance for the antenna at 915 MHz with acceptable impedance as shown in Figure 3-2, the simulation was modeled using a sinusoidal voltage source and then the radiation patterns was computed.

Simulations were carried out in the FCC regulated ISM frequency 902-928 MHz band, the center of this band, 915MHz was used. After the proper resonance is assured, other parameters such as far-field radiation patterns in multiple directions (more than one request) and a 3D plot can be requested and performed.

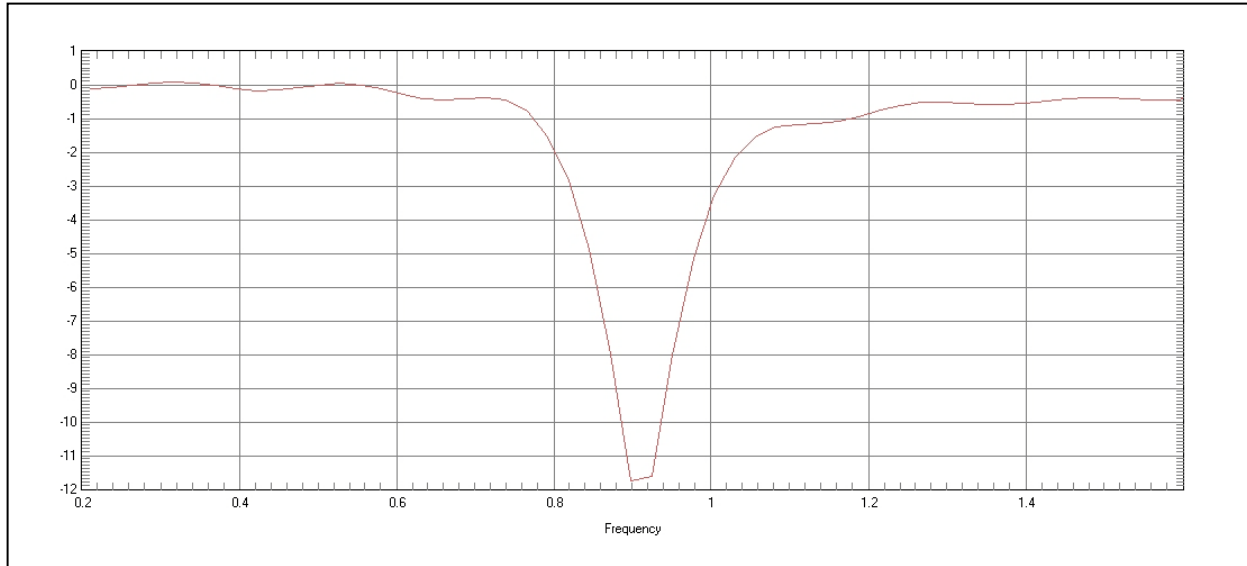


Figure 3-2. A folded dipole demonstrating a tuned and matched configuration at 915 MHz with a reflection coefficient of -11.7dB corresponding to 93.3% of the applied power being transmitted to the antenna.

Once the initial tuning was confirmed the full simulation taking around 40 minutes was performed and the far field results were requested. The far field patterns for the dipole antenna were requested in X-Z, Z-Y and a combined 3D of the entire system.

As shown in Figure 3-3, Phi and Theta plots (overlaid, 360 degrees requested per plane) are shown with the antenna oriented along the 0, 180 degree line. This demonstrates the far field pattern radiating from the dipole antenna with the distance normalized to the default values that are predetermined by REMCOM for ease of use.

While 2D plots are informative, it is very convenient to analyze the data in 3D, especially if the detection of subtle changes due to external forces is being examined. The 3D pattern for the $\lambda/2$ dipole is shown in Figure 3-4, where the antenna is in the x direction, but the graph is rotated slightly in the y direction to give the 3D perspective. The graph in Figures 3-3 and 3-4 yield the expected results of a spherical or donut

pattern for a dipole antenna, and serve as a frame of reference for future simulations involving the human body model

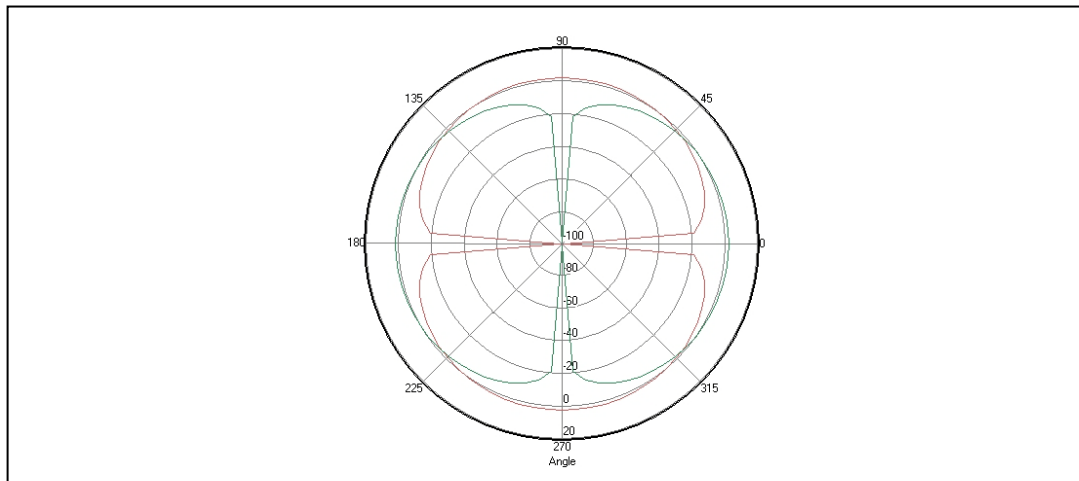


Figure 3-3. The radiation pattern of a standard $\lambda/2$ dipole antenna at 915 MHz in air, the Phi and Theta plane, demonstrate the symmetrical nature of a dipole antenna radiation pattern.

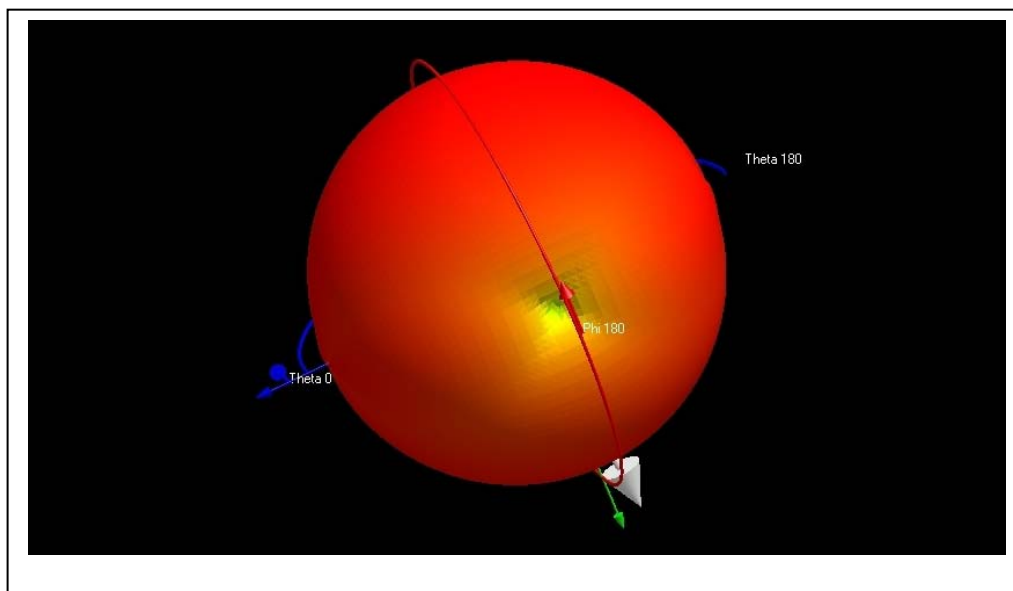


Figure 3-4. The 3D radiation pattern for a dipole at 915MHz is displayed as a reference.

The ability to work in 3D, especially when something other than free space is considered, such as the human body model, is a very important feature to be able to have access to and will be demonstrated in the following simulations.

Folded dipole on the human body

The folded dipole was drawn and placed over the upper abdomen of the subject, simulating signals passing through the stomach. The human torso model with a vertical orientation had the antenna placed in the coronal plane of the torso is shown in Figure 3-1. The folded dipole antenna was first designed to resonate at the aforementioned frequency 915 MHz by forcing a single cell sized gap in the loop and inserting a complex source impedance of the appropriate value (L matching network) and the resonance and impedance was found by applying a Gaussian source excitation.

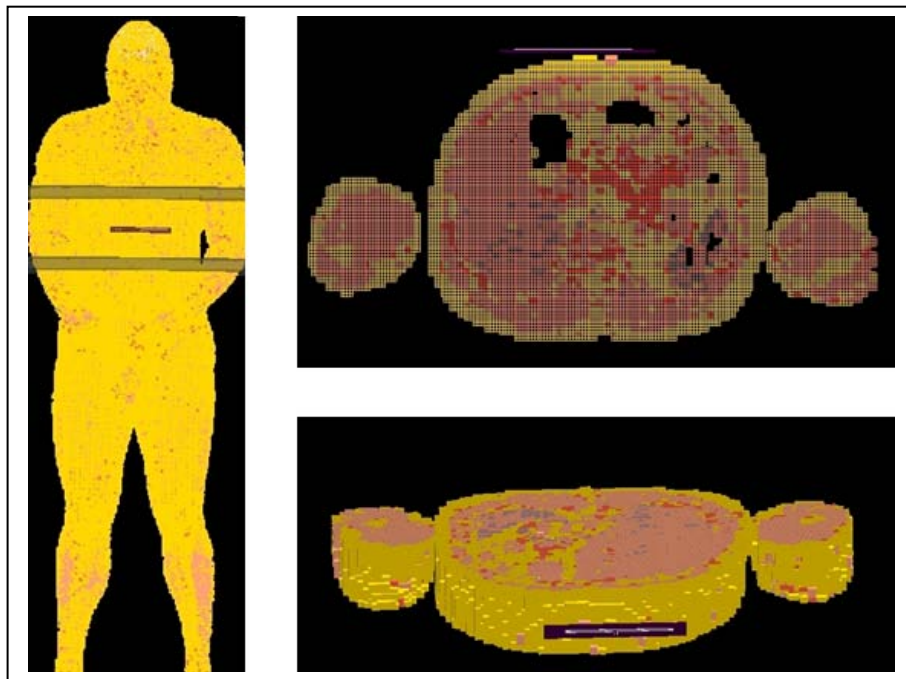


Figure 3-5. A folded dipole that was simulated, showing its location on the human body model.

A narrow band Gaussian pulse was applied to check for resonance and the results are shown in Figure 3-6. After achieving the correct resonance for the antenna, the simulation was modeled using a sinusoidal voltage source and the results were requested.

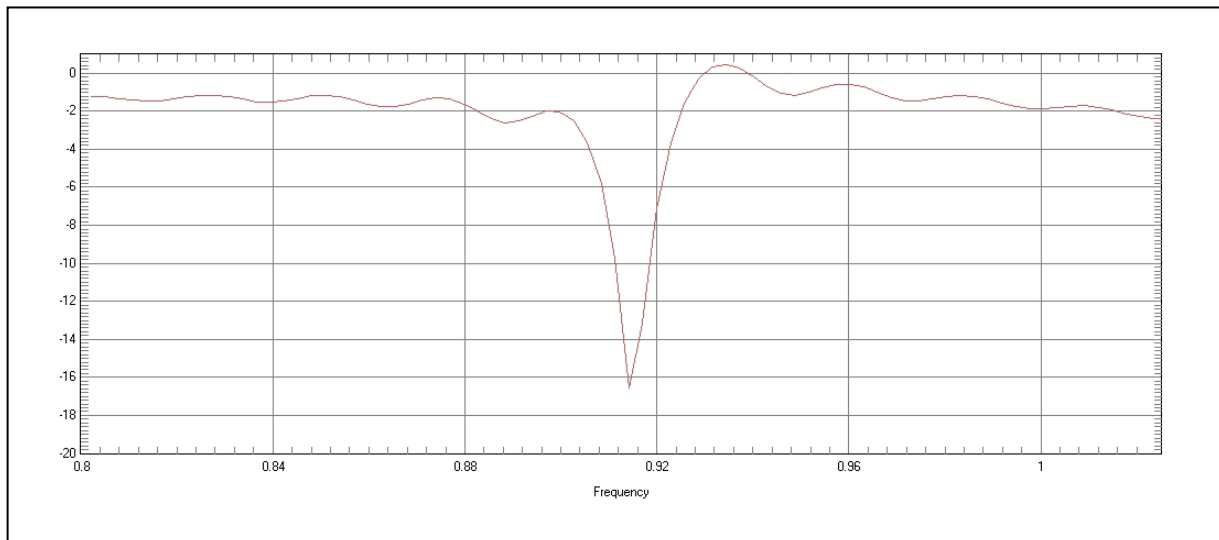


Figure 3-6. A folded dipole demonstrating a tuned and matched configuration at 914 MHz on the human body model with a reflection coefficient of -16.5dB was corresponding to 97.7% of the power being transmitted to the antenna and into the sample.

Once the initial tuning took around 40 minutes per run. After approximately 9 attempts at tuning and matching, a well tuned and matched 914 MHz antenna was used (within ~1% of the desired value) the full simulation using a 914 MHz sinusoidal waveform was performed, taking approximately 36 hours to complete the simulation. At this point, the far field results were requested along with the SAR plots. The far field patterns for the dipole antenna were requested in X-Z, Z-Y and a combined 3D of the entire system. The SAR plots are taken at the slices through the antenna system.

As shown in Figure 3-7, Phi and Theta plots (overlaid, 360 degrees requested per plane) are shown with the antenna oriented along the 0, 180 degree line.

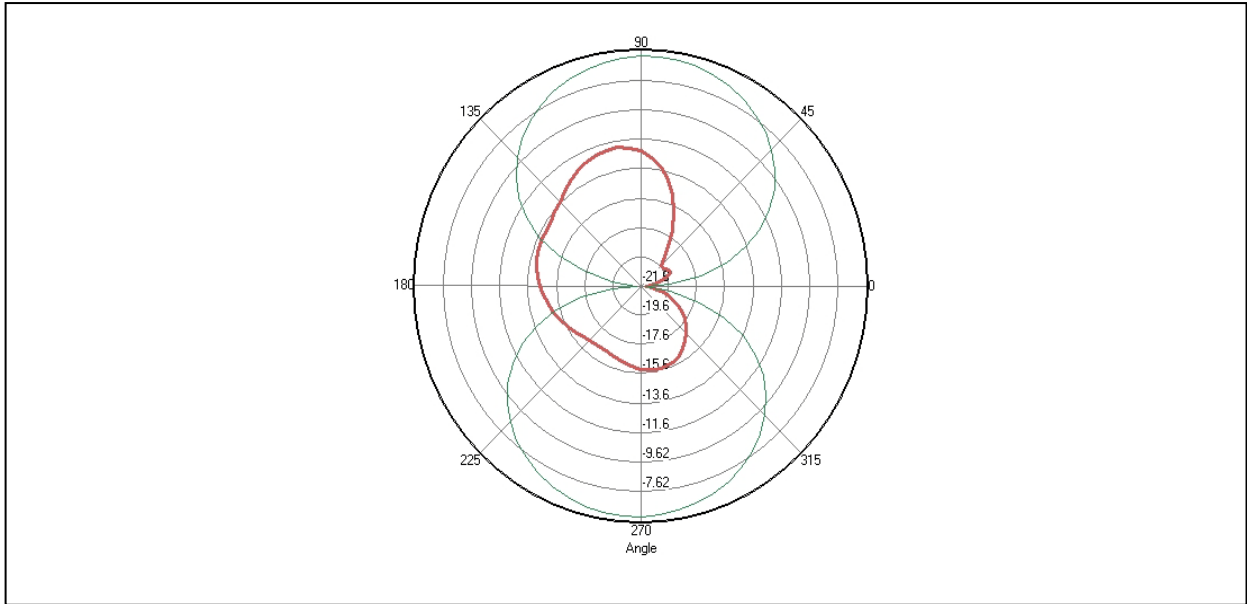


Figure 3-7. The Phi and Theta patterns of the folded dipole antenna, from this we can see that the Phi pattern is disturbed by the human body model.

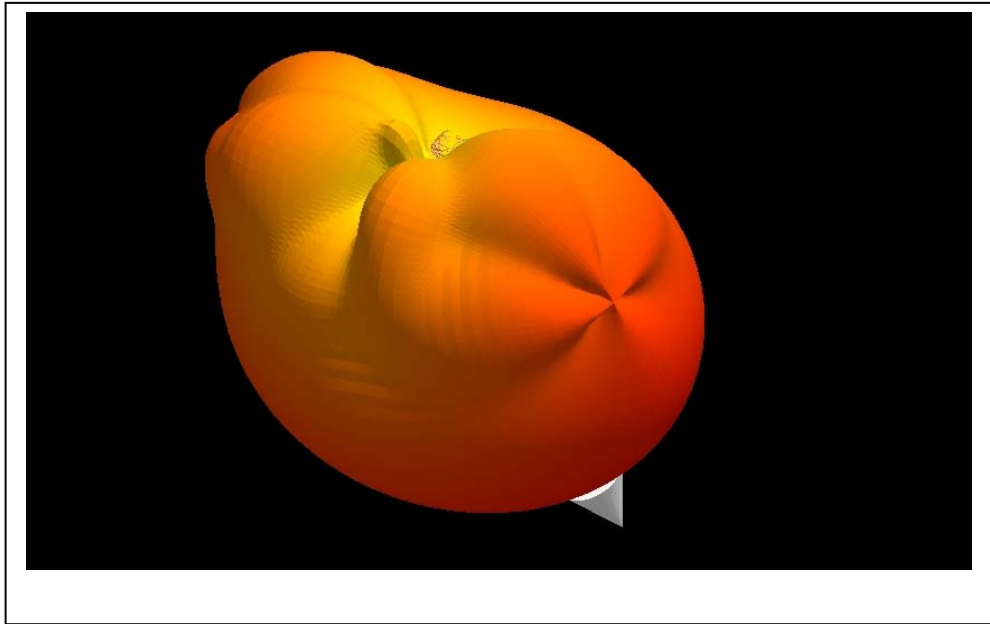


Figure 3-8. A 3D look at the combined Phi and Theta patterns of the folded dipole applied to the human body model at 914 MHz.

This demonstrates human body models interaction with the folded dipole antenna when placed on the body and is also shown in a 3D plot in Figure 3-8. These plots

demonstrate the effect that the human body has upon antennas and that future antenna designs should include a human body model when design and the use of fractal antennas could be used to get the desired directivity and gain. Not only is it important to have the field pattern of an antenna in the human body it is also useful to know the SAR distribution as shown in Figure 3-9. The SAR was calculated using a 2W sinusoidal source (continuous wave), a transmission level that could be considered reasonable for transmitting through the human body.

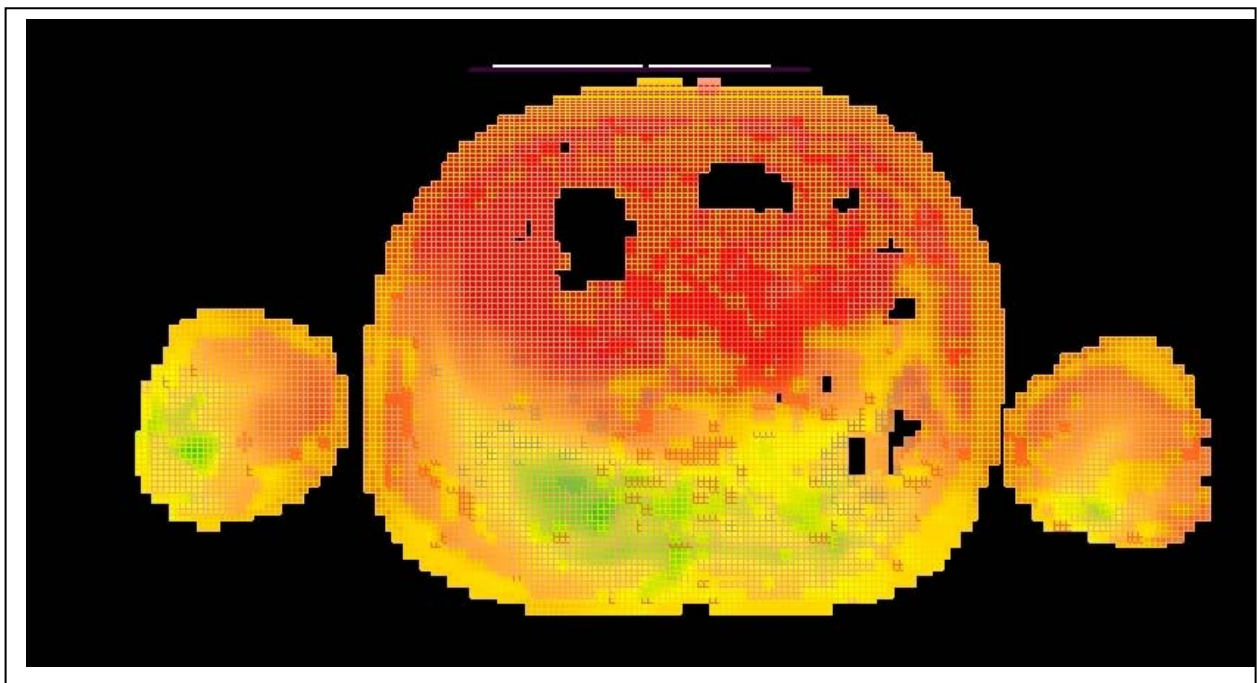


Figure 3-9. The SAR distribution for the folded dipole on the human body model.

The SAR distribution goes from green to red, where the darkest red areas correspond to the highest levels of SAR induced in the human body. In Figure 3-9, it is shown that the highest SAR is toward the middle of the sample. Figure 3-10 describes the SAR statistics, showing that this high value is 9W/kg for a 1 gram average maximum SAR located approximately 13 cm away from the antenna in the body. This value far

exceeds the FCC mandated 1g SAR of 1.6W/kg in 1 gram of tissue. Therefore, if higher transmission powers are required to get the depth penetration, other methods for controlling the transmitted power must be employed and could be things such as controlling the duty cycle of an applied pulse.

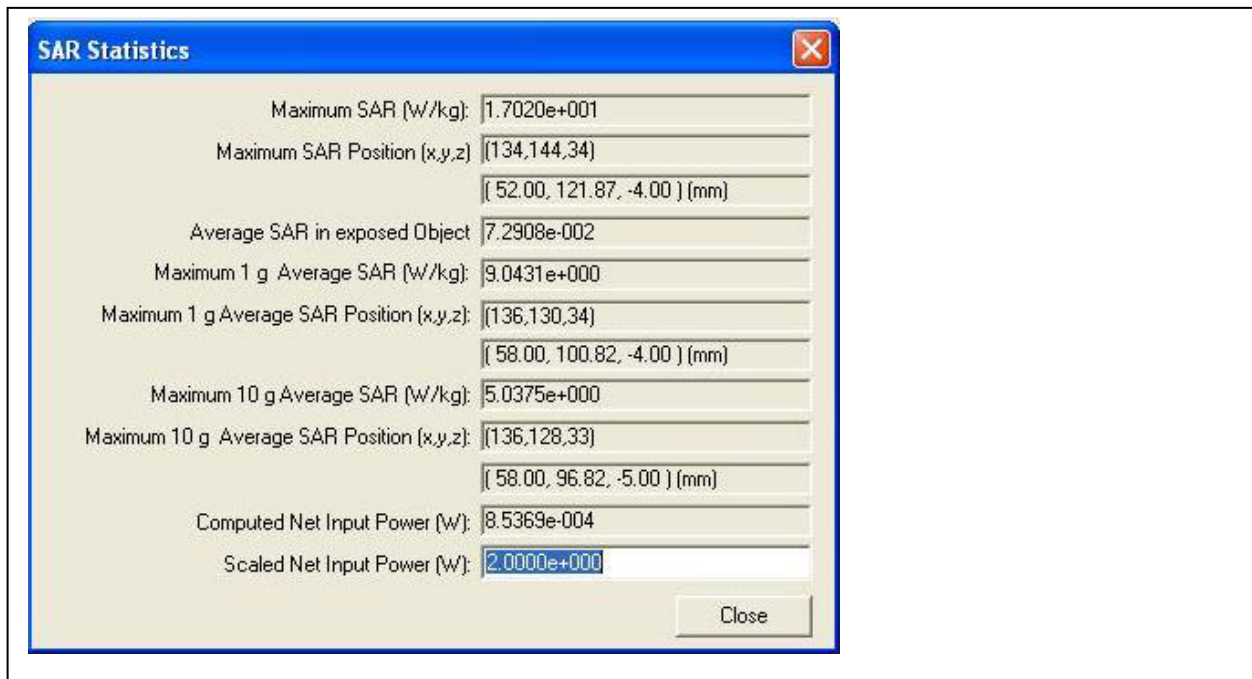


Figure 3-10. SAR for 1 gram average violating the safety guidelines by exceeding 9W/kg.

MRI coil on the human body

The human torso model, a representative cross-section of the torso and the location and orientation of the antenna is shown in Figure 3-11. The MRI coil was located in the stomach area, for comparison to the folded dipole that was also placed over the torso; each antenna was slightly offset from the body axis. The antenna and modeling setup was calibrated extensively for accuracy and rapid convergence. The calibration process comprised of determining the appropriate mesh size, time steps, radiation boundaries, padding cells and source type to yield convergence within a

reasonable time. The MRI coil was designed to resonate at a frequency of 915 MHz by inserting multiple single cell sized gaps around the loop and inserting a complex source impedance of the appropriate value (active at the input and passive capacitors at the other locations) and the resonance and impedance was found by applying a Gaussian source excitation.

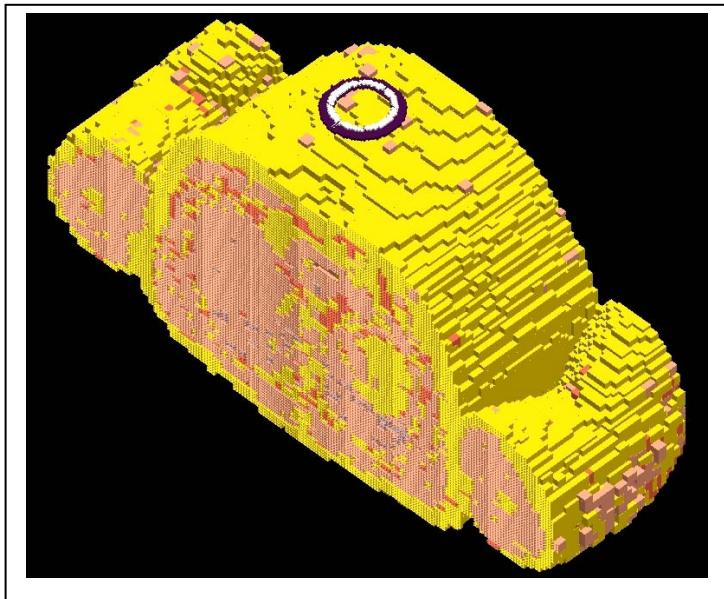


Figure 3-11. The MRI coil that was simulated, showing its location on the human body model, using the same location as the folded dipole.

A narrow band Gaussian pulse was applied to check for resonance and the results are shown in Figure 3-12.

After achieving the correct frequency for the MRI coil, the simulation was modeled using a sinusoidal voltage source and the far-field radiation pattern and SAR results were requested. The initial tuning took around 4 hours per run. After approximately 3 attempts at tuning and matching, a well tuned and matched 915 MHz antenna was used

the full simulation using a 915 MHz sinusoidal waveform was performed, taking approximately 24 hours to complete the simulation. At this point, the far field results were requested along with the SAR plots. The far field patterns for the MRI coil were requested in X-Z, Z-Y and a combined 3D of the entire system. The SAR plots are taken at the slices through the antenna system.

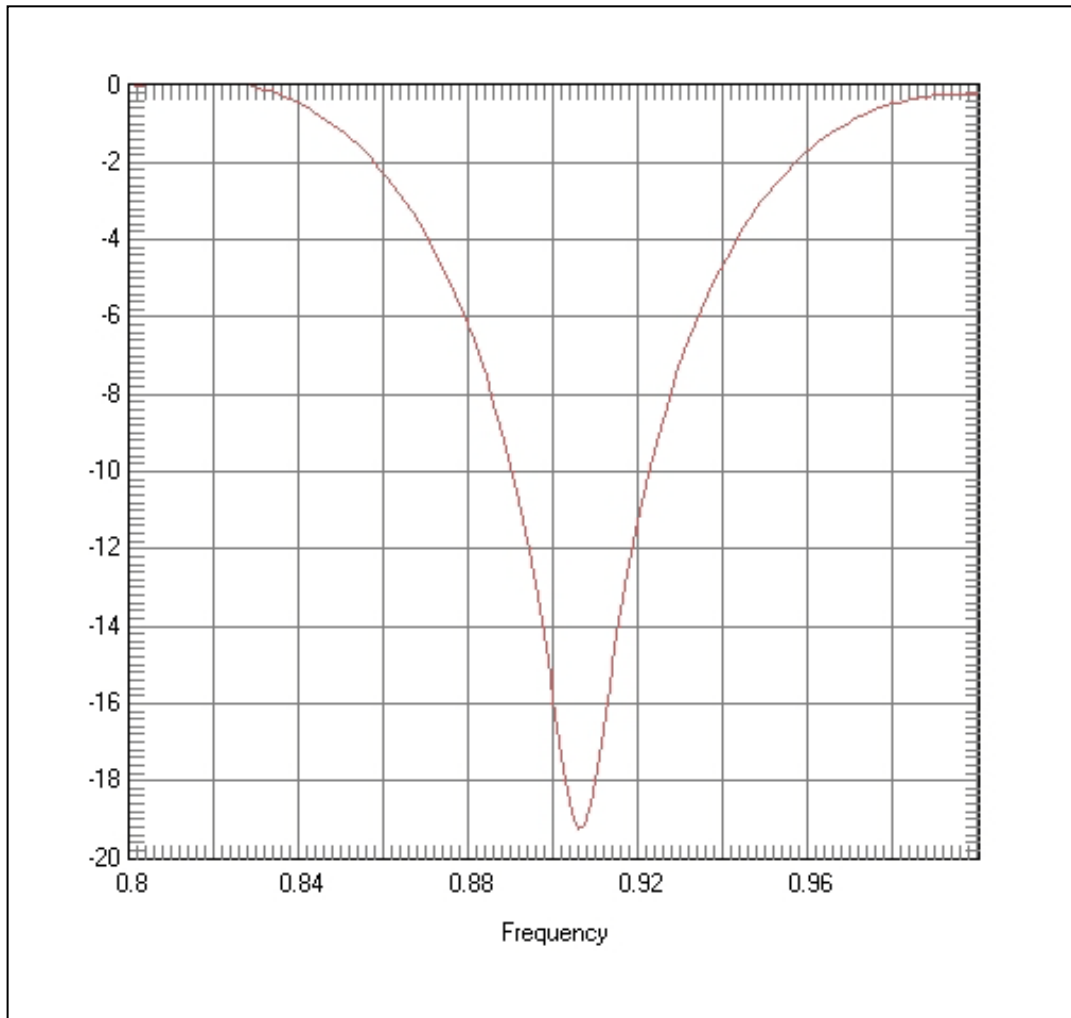


Figure 3-12. The MRI coil that was simulated, showing its location on the human body model, using the same location as the folded dipole, tuned to 915 MHz with a reflection of -19.5dB resulting in approximately 98.9% of the power being applied to the MRI coil.

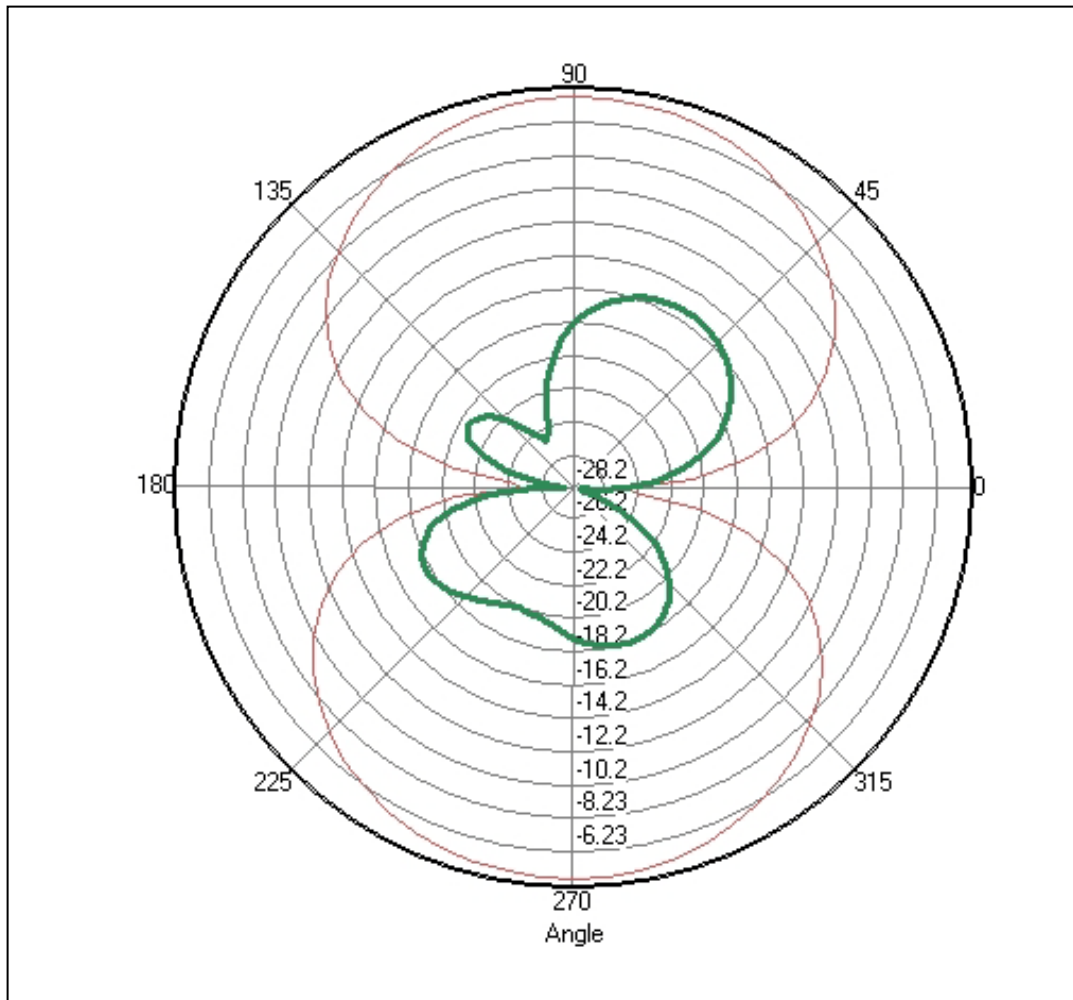


Figure 3-13. The Phi and Theta patterns of the MRI coil, from this we can see that the Theta pattern is disturbed by the human body model.

As shown in Figure 3-13, Phi and Theta plots (overlaid, 360 degrees requested per plane) are shown with the antenna oriented along the 0, 180 degree line. In this case, the Theta field is affected, which is the complement of a loop antenna when compared to a dipole. While the distortions are similar between the antenna and the coil, the balance of the coil pattern is due to the capacitance added around the loop.

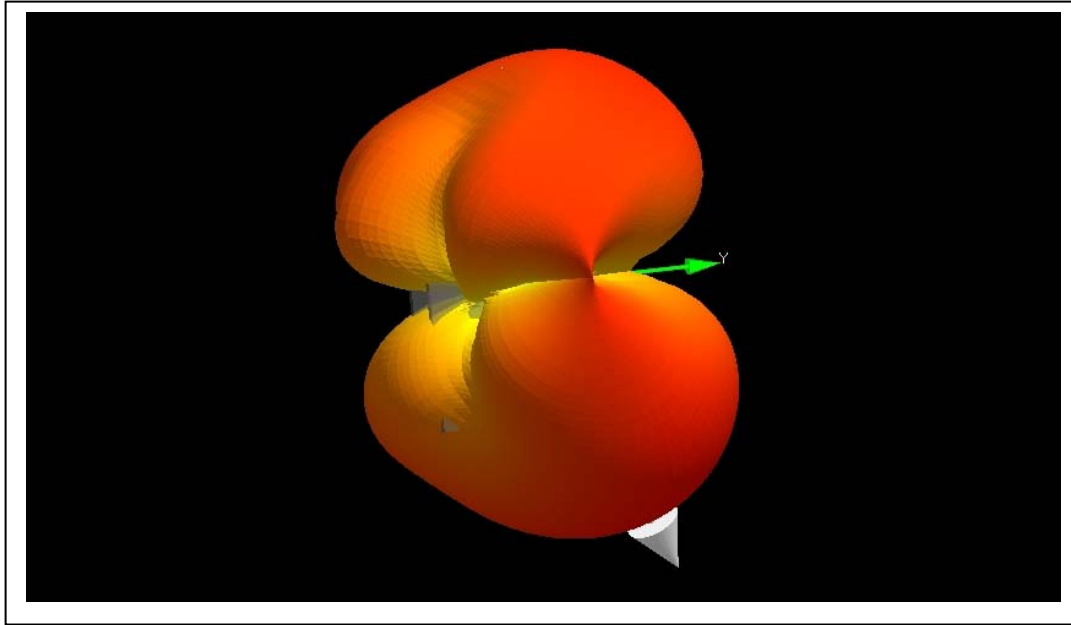


Figure 3-14. A 3D look at the combined Phi and Theta patterns of the MRI coil applied to the human body model at 915 MHz.

It is useful to know the SAR distribution as shown in Figure 3-15. The SAR was calculated using a 2W sinusoidal source (continuous wave), a transmission level that could be considered reasonable for transmitting through the human body, considering a whole body coil at 1.5 Tesla can use 40W of average power with a body coil.

The SAR distribution goes from green to red, where the darkest red areas correspond to the highest levels of SAR induced in the human body. In Figure 3-15, it is shown that the highest SAR is toward the anterior edge of the stomach and a corresponding hotspot 180 degrees away in the X direction. Figure 3-16 describes the SAR statistics, showing that this high value is approximately 6 W/kg for a 1 gram average maximum SAR located approximately 4.4 cm away from the antenna in the body. This value far exceeds the FCC mandated 1g SAR of 1.6W/kg in 1 gram of tissue, however the FCC standard is not applicable to MRI and the IEC 60601-1 standard applies, where the transmitting MRI coil cannot exceed 8W/kg in the torso over

any 5 minute period. This demonstrates the differences between different standards and how they are applied to the human body.

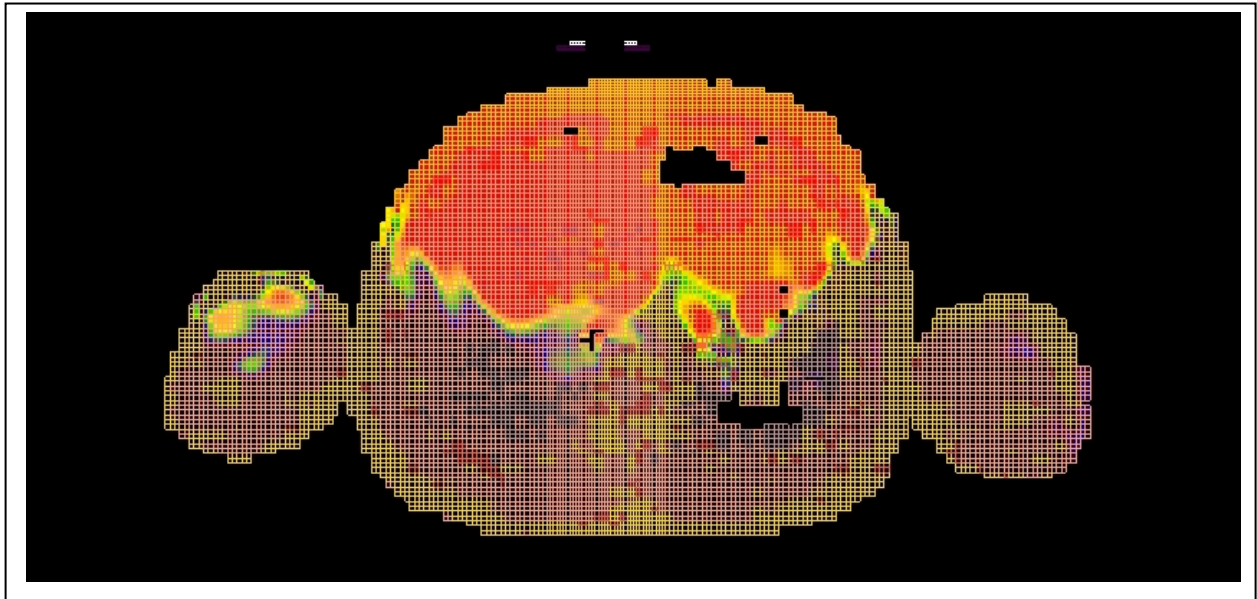


Figure 3-15. The MRI coil simulation, showing its location on the human body model, using the same location as the folded dipole.

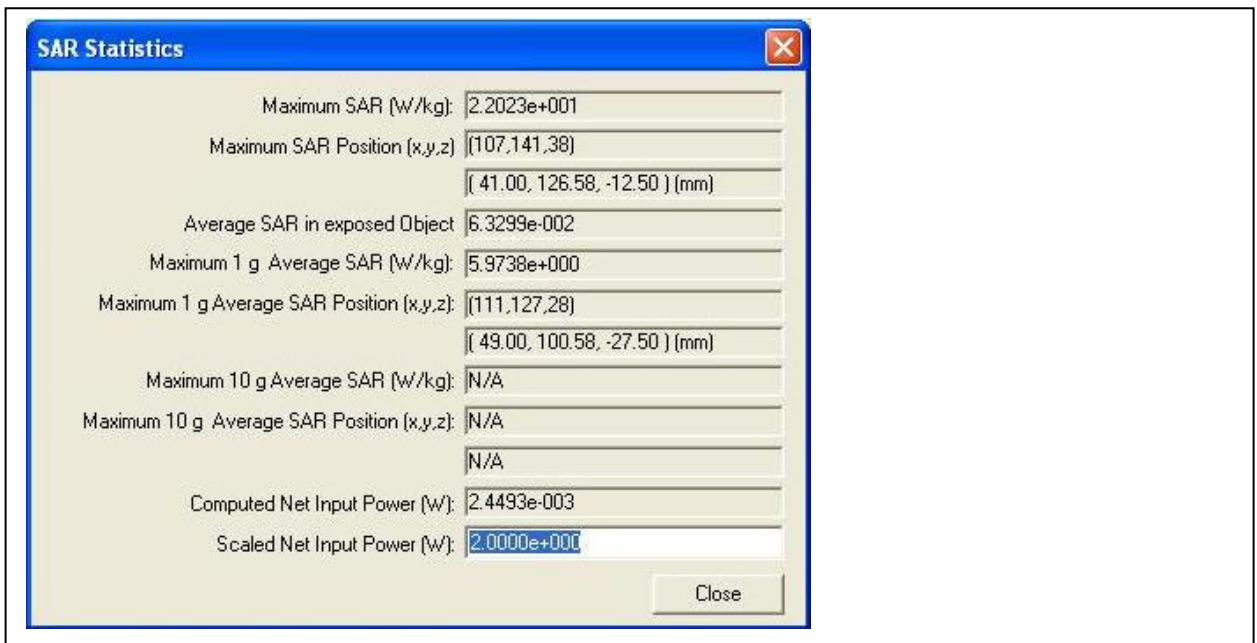


Figure 3-16. SAR for 1 gram average violating the safety guidelines by exceeding 5W/kg.

MRI coil on the 1 S/m saline phantom

A 30 cm x 30 cm x 20 cm box defined to contain a 1 S/m saline solution was created to be a represent a cross-section of the torso and the location and orientation of the antenna is shown in Figure 3-17. The MRI coil was centered on the box since this is a homogenous phantom without a stomach and antenna was slightly offset from the Phantom. The antenna and modeling setup was calibrated extensively for accuracy and rapid convergence. The calibration process comprised of determining the appropriate mesh size, time steps, radiation boundaries, padding cells and source type to yield convergence within a reasonable time. The MRI coil was designed to resonate at a frequency of 904 MHz by inserting multiple single cell sized gaps around the loop and inserting a complex source impedance of the appropriate value (active at the input and passive capacitors at the other locations) and the resonance and impedance was found by applying a Gaussian source excitation.

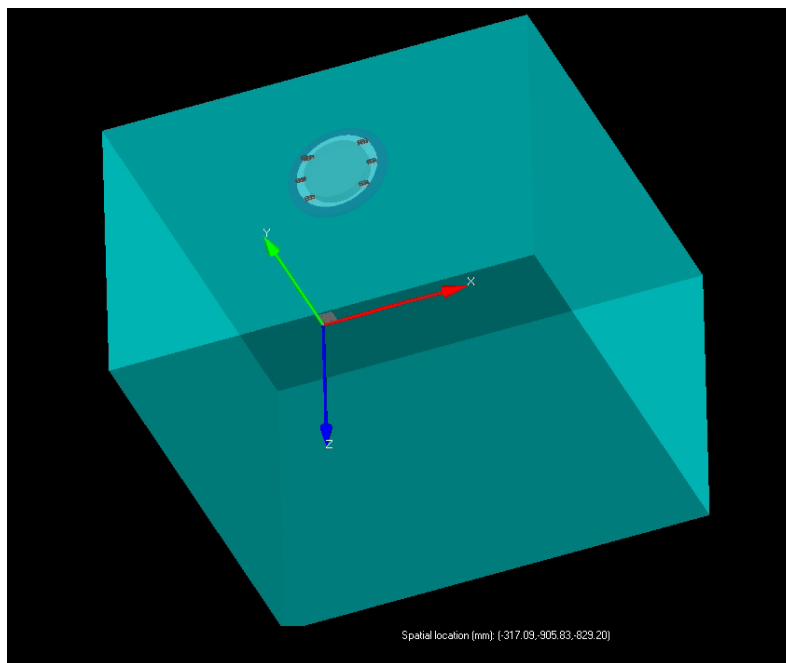


Figure 3-17. The MRI coil that was simulated, showing its location on the saline model.

. A narrow band Gaussian pulse was applied to check for resonance and the results are shown in Figure 3-18.

After achieving the correct frequency for the MRI coil, the simulation was modeled using a sinusoidal voltage source and the far-field radiation pattern and SAR results were requested. The initial tuning took around 4 hours per run. After approximately 6 attempts at tuning and matching, a well tuned and matched 904 MHz antenna was used the full simulation using a 904 MHz sinusoidal waveform was performed, taking approximately 24 hours to complete the simulation. At this point, the far field results were requested along with the SAR plots. The far field patterns for the MRI coil were requested in X-Z, Z-Y and a combined 3D of the entire system. The SAR plots are taken at the slices through the antenna system.

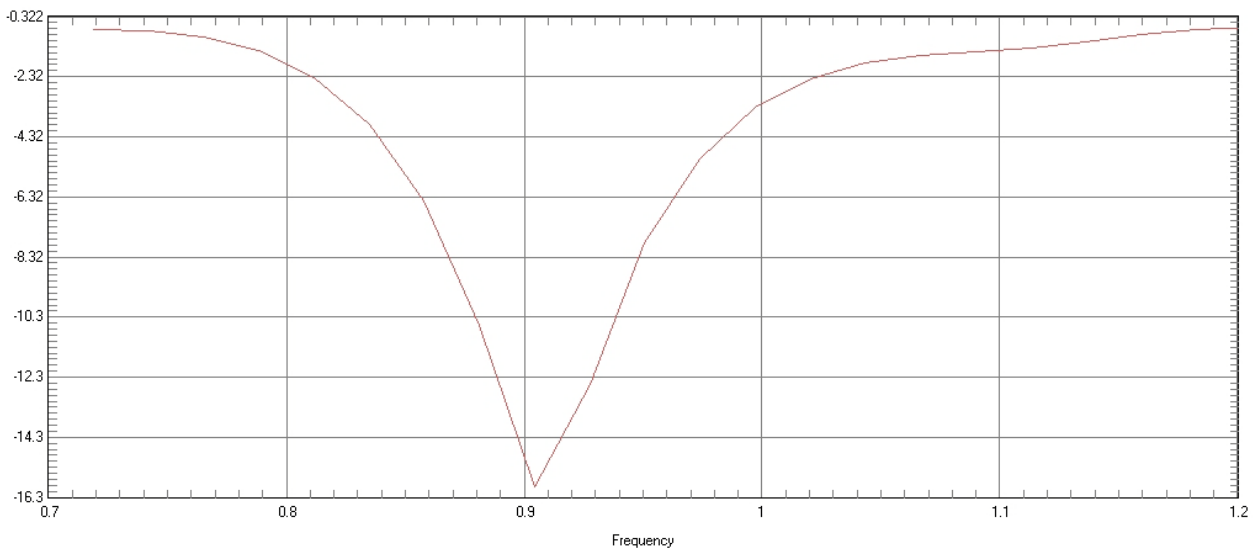


Figure 3-18. The MRI coil that was simulated, tuned to approximately 904 MHz with a reflection of -16.1dB resulting in approximately 97% of the power being applied to the MRI coil.

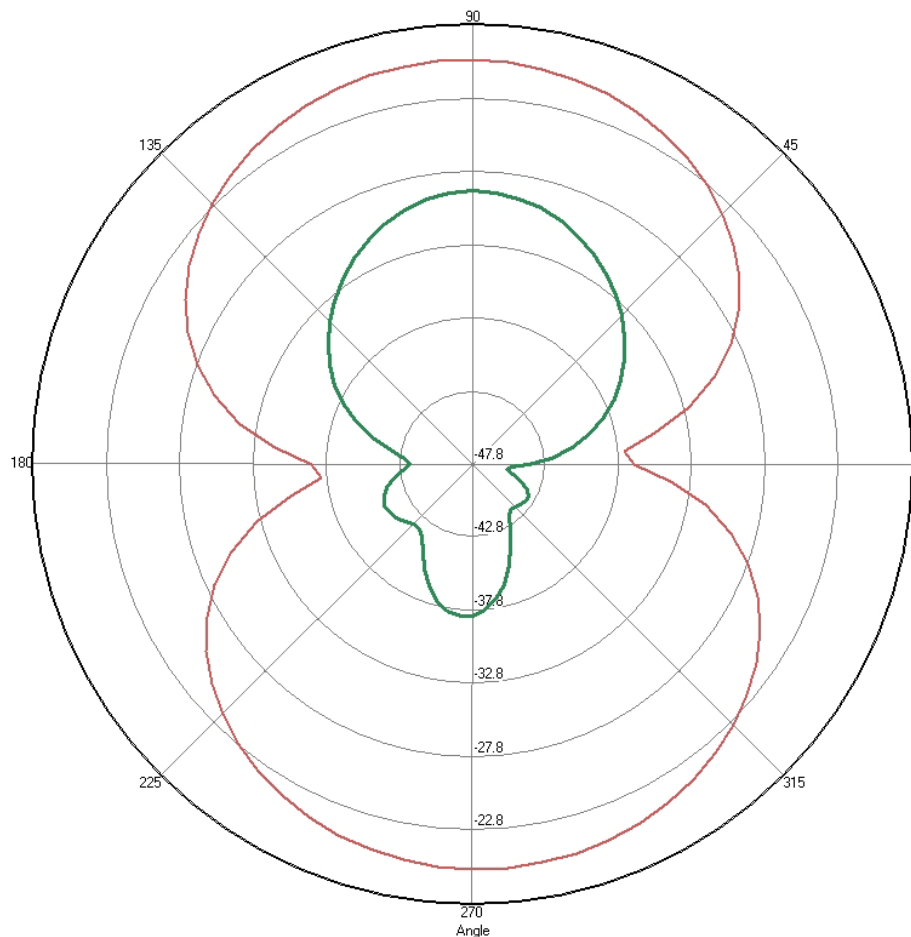


Figure 3-19. The Phi and Theta patterns of the MRI coil, from this we can see that the Theta pattern is disturbed by the saline box.

As shown in Figure 3-19, Phi and Theta plots (overlaid, 360 degrees requested per plane) are shown with the antenna oriented along the 0, 180 degree line. In this case, the Theta field is affected, which is the complement of a dipole antenna when compared to a loop antenna. While the distortions are similar between the antenna and

the coil, the imbalance of the coil pattern is due to the capacitance added around the loop.

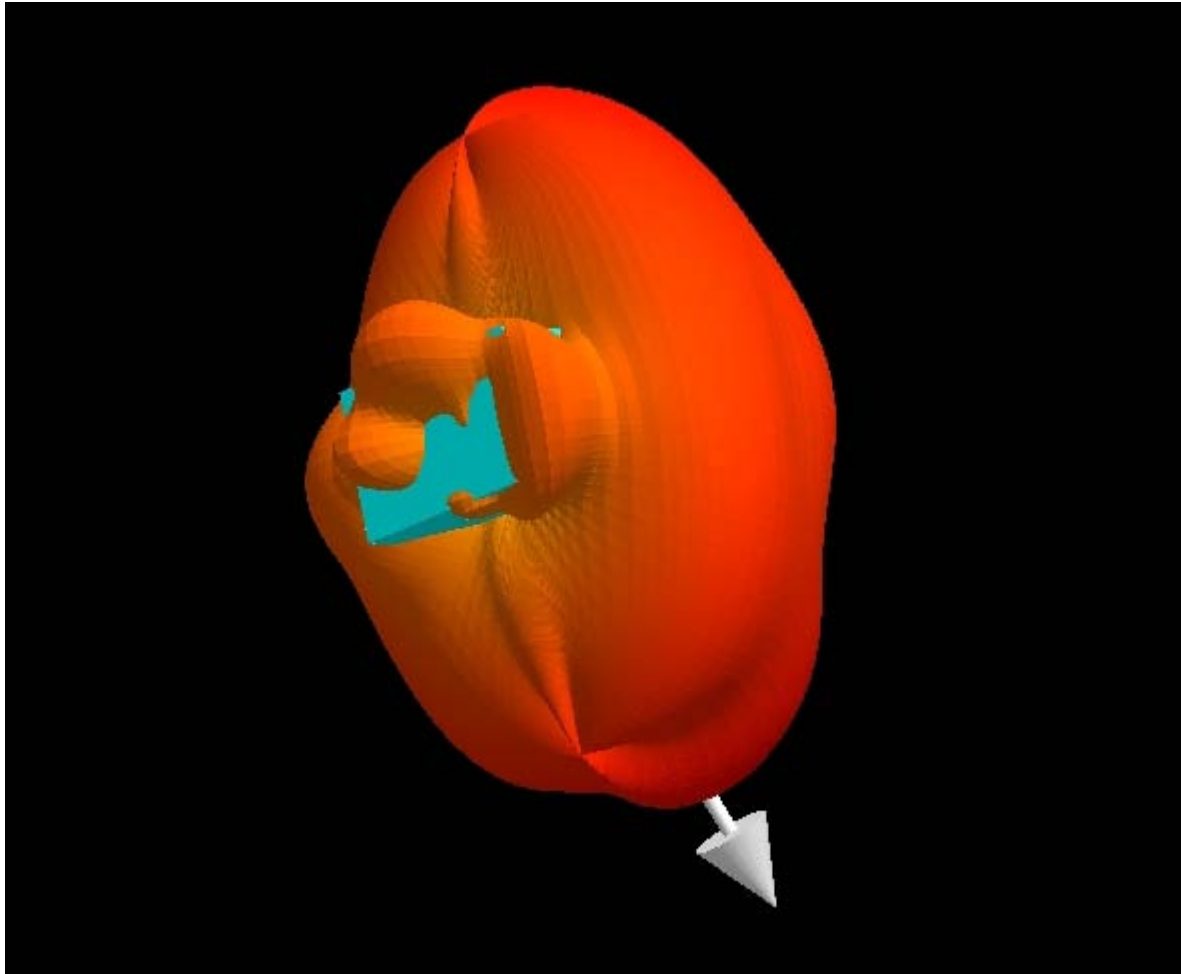


Figure 3-20. A 3D look at the combined Phi and Theta patterns of the MRI coil applied to the saline box at 905 MHz.

It is useful to know the SAR distribution as shown in Figure 3-21. The SAR was calculated using a 2W sinusoidal source (continuous wave), a transmission level that could be considered reasonable for transmitting through the human body, considering a whole body coil at 1.5 Tesla can use 40W of average power with a body coil.

The SAR distribution goes from green to red, where the darkest red areas correspond to the highest levels of SAR induced in the human body. In Figure 3-21, it is shown that the highest SAR is toward the middle of the sample. Figure 3-22 describes the SAR statistics, showing that this high value is approximately 2 W/kg for a 1 gram average maximum SAR located approximately 2 cm away from the antenna in the saline. This value barely exceeds the FCC mandated 1g SAR of 1.6W/kg in 1 gram of tissue, however the FCC standard is not applicable to MRI and the IEC 60601-1 standard applies, where the transmitting MRI coil cannot exceed 8W/kg in the torso over any 5 minute period and is well within the prescribed limits. This demonstrates the differences between different standards and how they are applied to the human body.

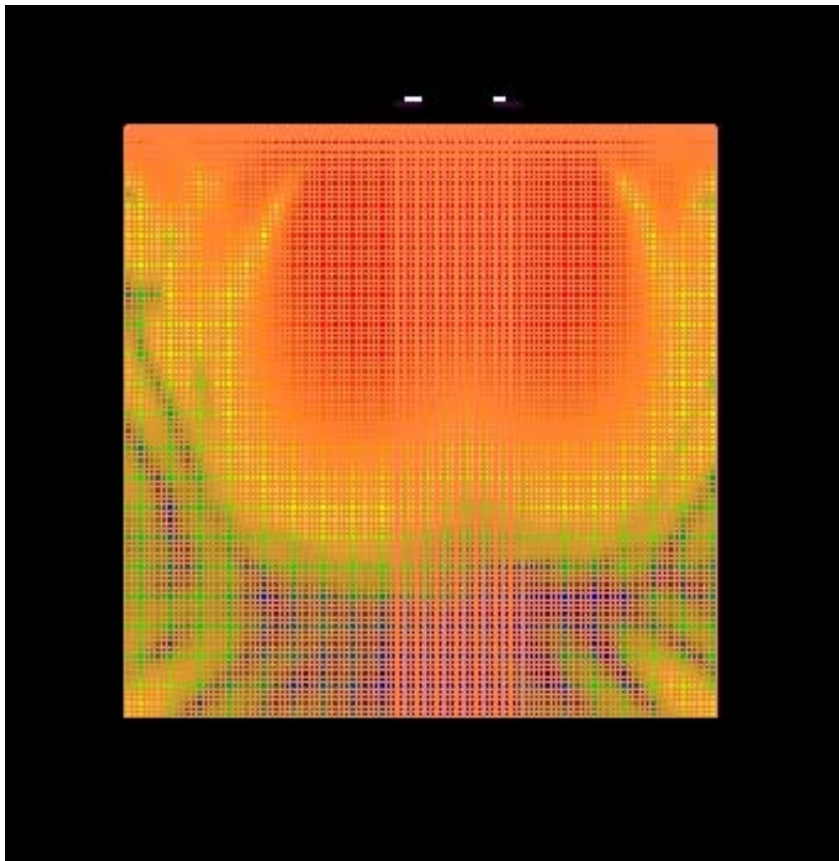


Figure 3-21. The MRI coil simulation, showing its location on the human body model, using the same location as the folded dipole.

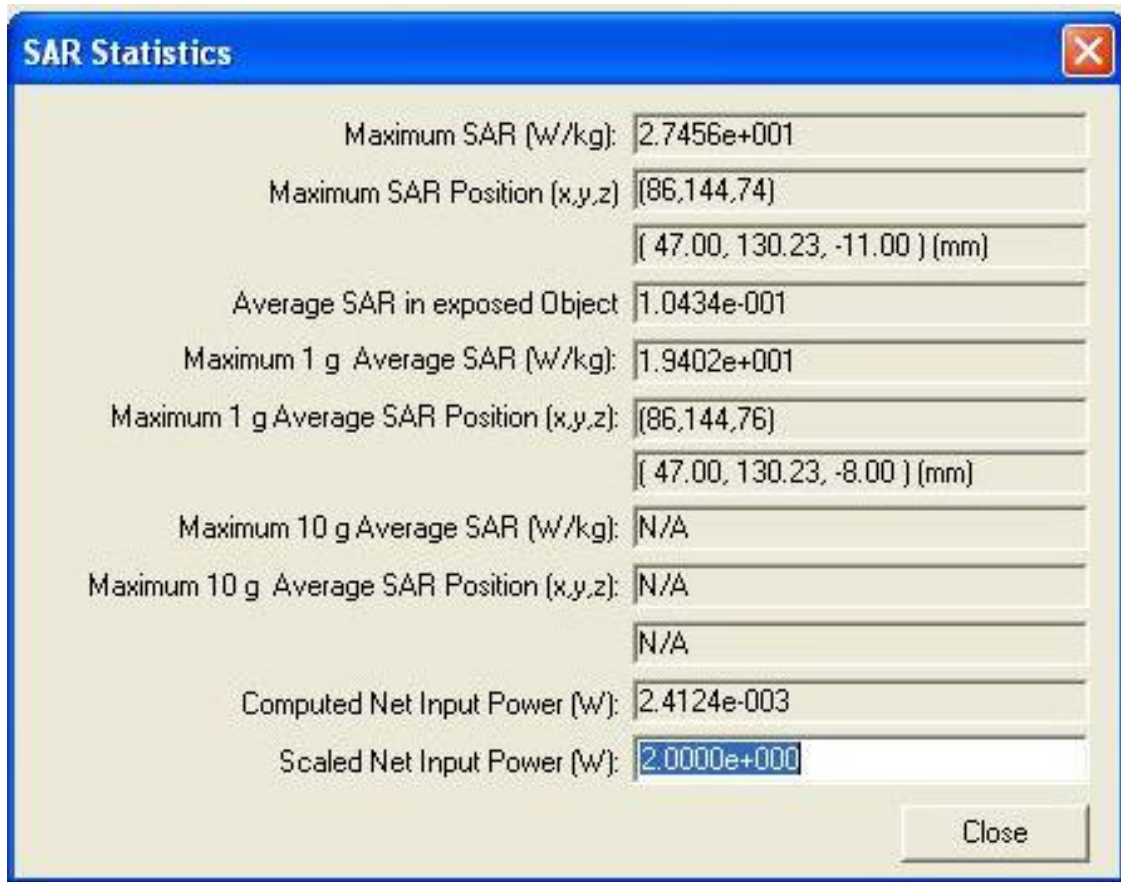


Figure 3-22. SAR for 1 gram average violating the safety guidelines by exceeding 5W/kg.

Folded dipole antenna on the 1 S/m saline phantom

A 30 cm x 30 cm x 20 cm box defined to contain a 1 S/m saline solution was created to be a represent a cross-section of the torso and the location and orientation of the antenna is shown in Figure 3-17. The folded dipole antenna was centered on the box since this is a homogenous phantom without a stomach and antenna was slightly offset from the Phantom. The antenna and modeling setup was calibrated extensively for accuracy and rapid convergence. The calibration process comprised of determining the appropriate mesh size, time steps, radiation boundaries, padding cells and source type to yield convergence within a reasonable time (in this particular case, 48 hours per run). The folded dipole antenna resonated at a frequency of 928 MHz but was designed

for 915 MHz, however, this less than a 2% difference in frequency. A 50Ω active transmission source was used and the resonance and impedance was found by applying a Gaussian source excitation.

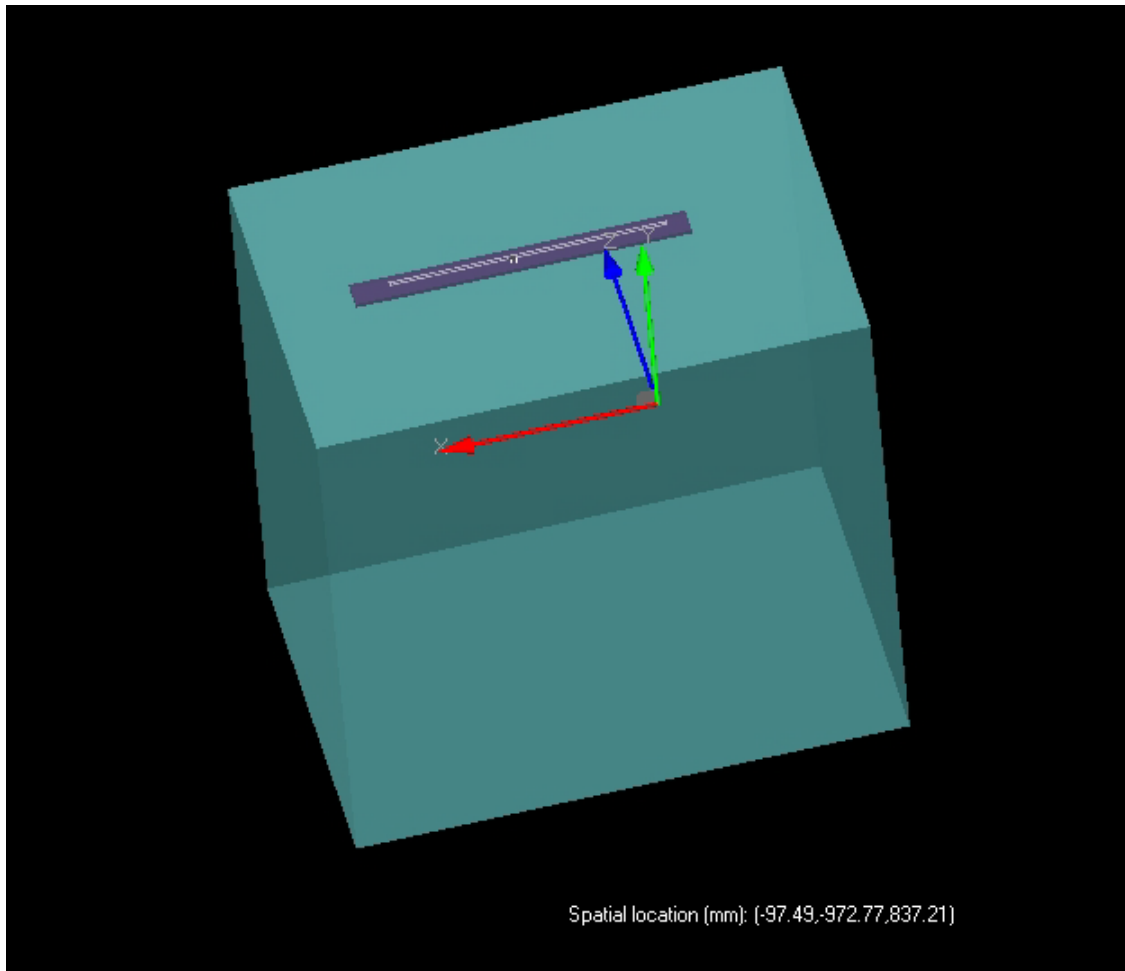


Figure 3-23. The MRI coil that was simulated, showing its location on the human body model, using the same location as the folded dipole.

A narrow band Gaussian pulse was applied to check for resonance and the results are shown in Figure 3-24.

After achieving the correct frequency for the folded dipole antenna, the simulation was modeled using a sinusoidal voltage source and the far-field radiation pattern and SAR results were requested. The initial tuning took around 48 hours per run. After one attempt at tuning and matching, a well tuned and matched 928 MHz antenna was used the full simulation using a 928 MHz sinusoidal waveform was performed, taking approximately 24 hours to complete the simulation. At this point, the far field results were requested along with the SAR plots. The far field patterns for the folded dipole antenna were requested in X-Z, Z-Y and a combined 3D of the entire system. The SAR plots are taken at the slices through the antenna system.

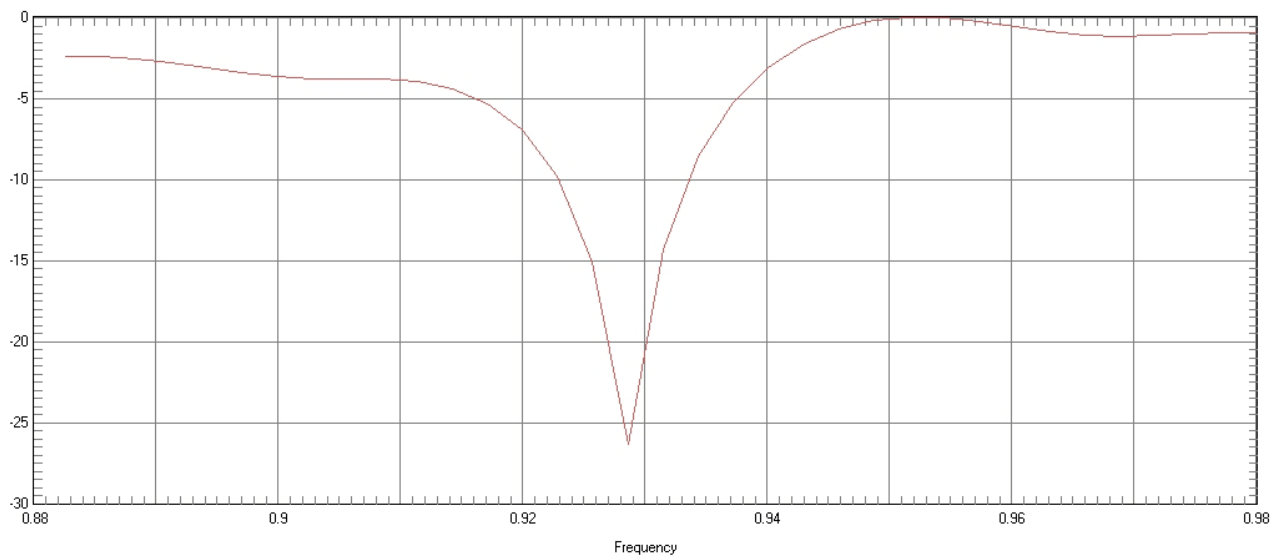


Figure 3-24. The folded dipole antenna was simulated, tuned to approximately 928 MHz with a reflection of -27dB resulting in approximately 99% of the power being applied to the folded dipole antenna.

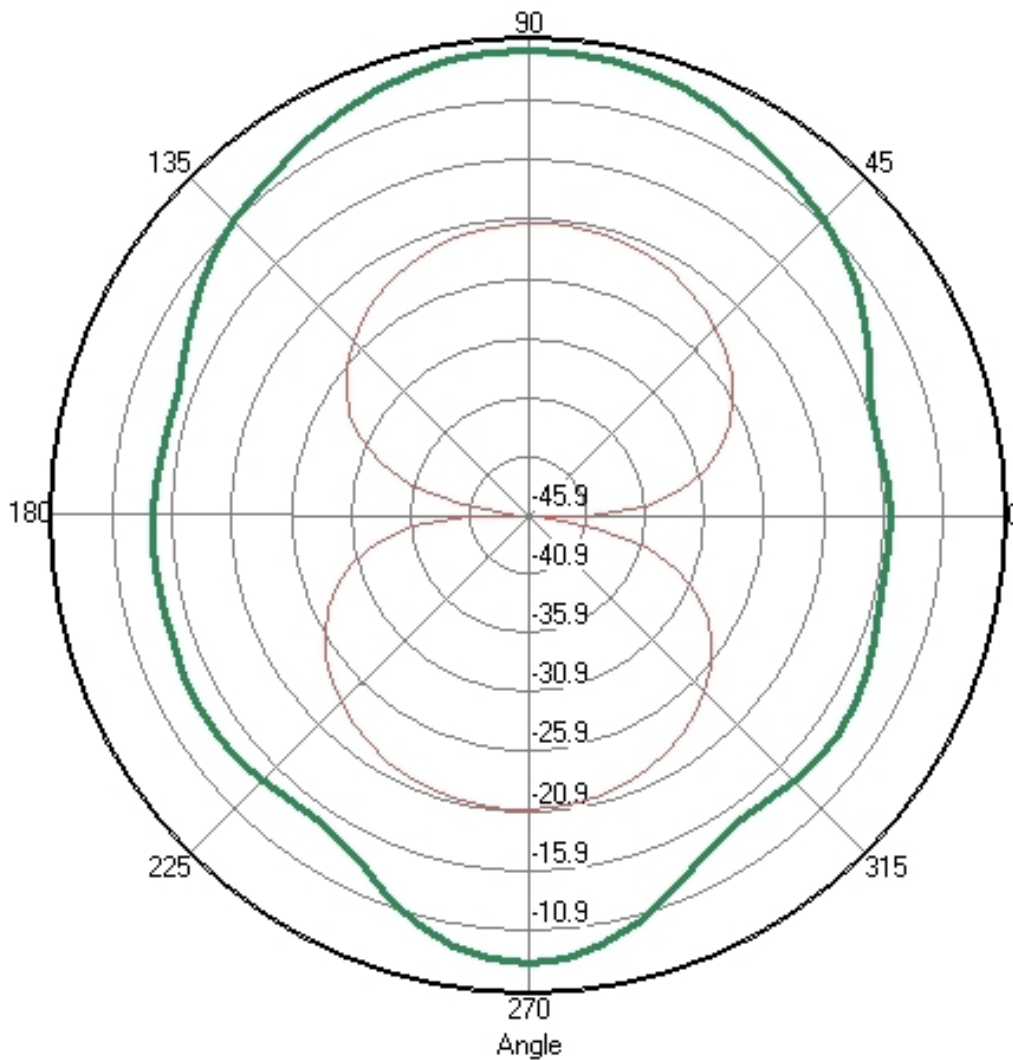


Figure 3-25. The Phi and Theta patterns of the MRI coil, from this we can see that the Phi pattern is disturbed by the saline box.

As shown in Figure 3-25, Phi and Theta plots (overlaid, 360 degrees requested per plane) are shown with the antenna oriented along the 0, 180 degree line. In this case, the Phi field is affected, which is the complement of a loop antenna when compared to a dipole. A 3D data set of the field is shown in Figure 3-26 and provides a complete picture on how the RF field is interacting with the saline box.

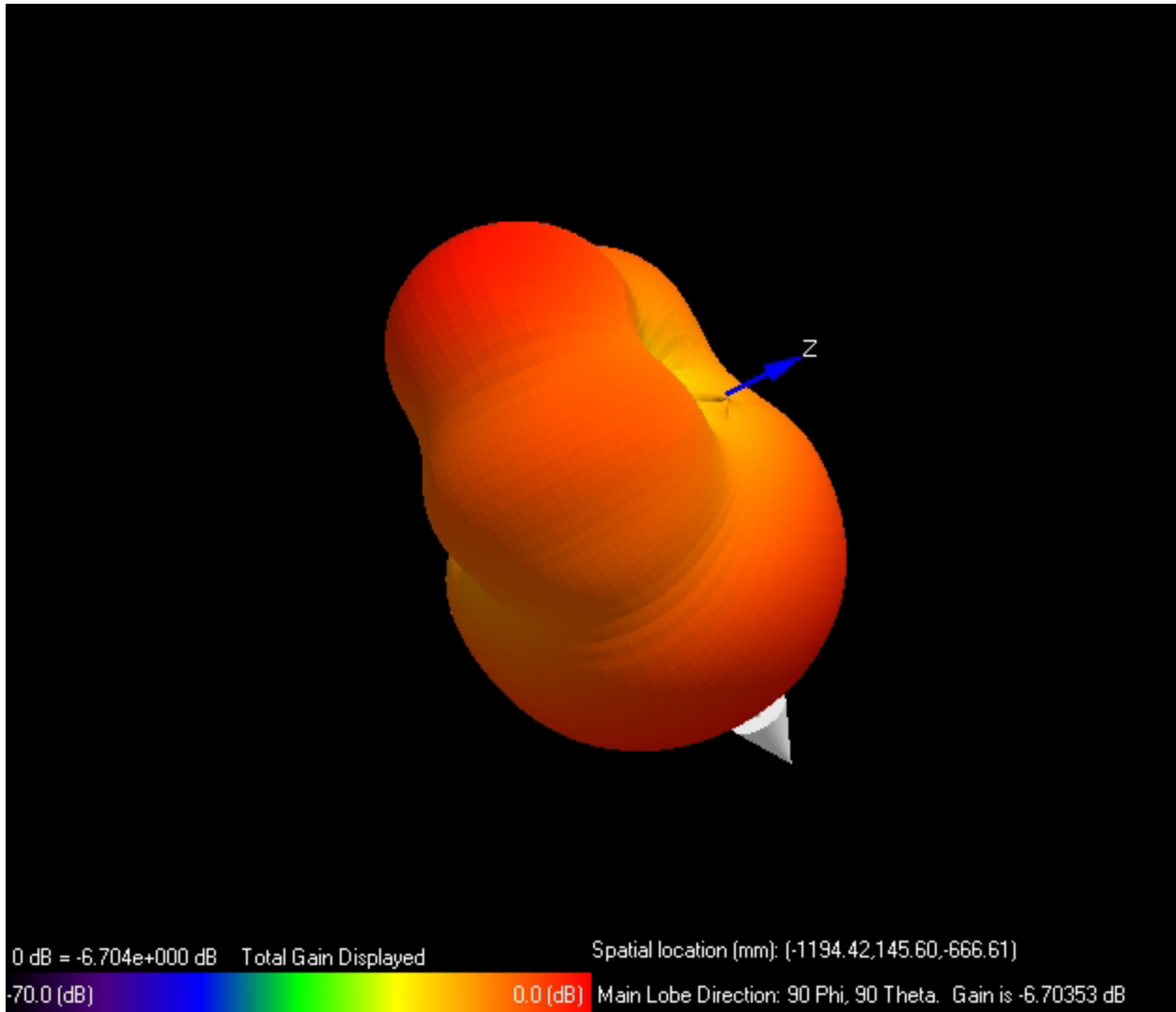


Figure 3-26. A 3D look at the combined Phi and Theta patterns of the MRI coil applied to the saline box at 905 MHz.

It is useful to know the SAR distribution as shown in Figure 3-27. The SAR was calculated using a 2W sinusoidal source (continuous wave), a transmission level that could be considered reasonable for transmitting through the human body, considering the use of cell phones work within this power range. The SAR distribution goes from green to red, where the darkest red areas correspond to the highest levels of SAR induced in the human body. In Figure 3-27, it is shown that the highest SAR is at the

edge of the sample. Figure 3-28 describes the SAR statistics, showing that this high value is approximately 2 W/kg for a 1 gram average maximum SAR located approximately 0.6 cm away from the antenna in the saline. This value barely exceeds the FCC mandated 1g SAR of 1.6W/kg in 1 gram of tissue in the saline phantom model, but contradicts the human body model simulation.

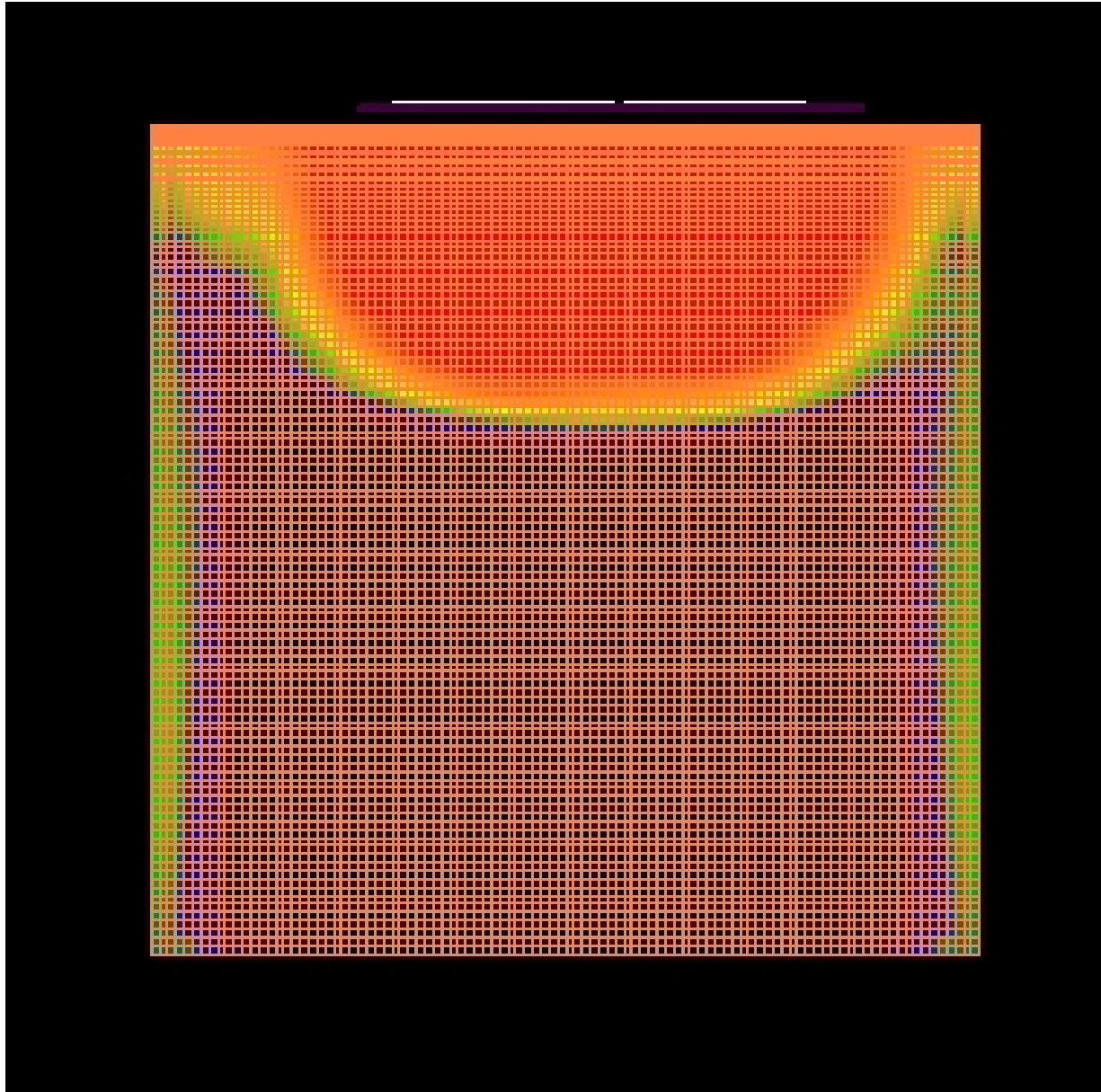


Figure 3-27. The MRI coil simulation, showing its location on the human body model, using the same location as the folded dipole.

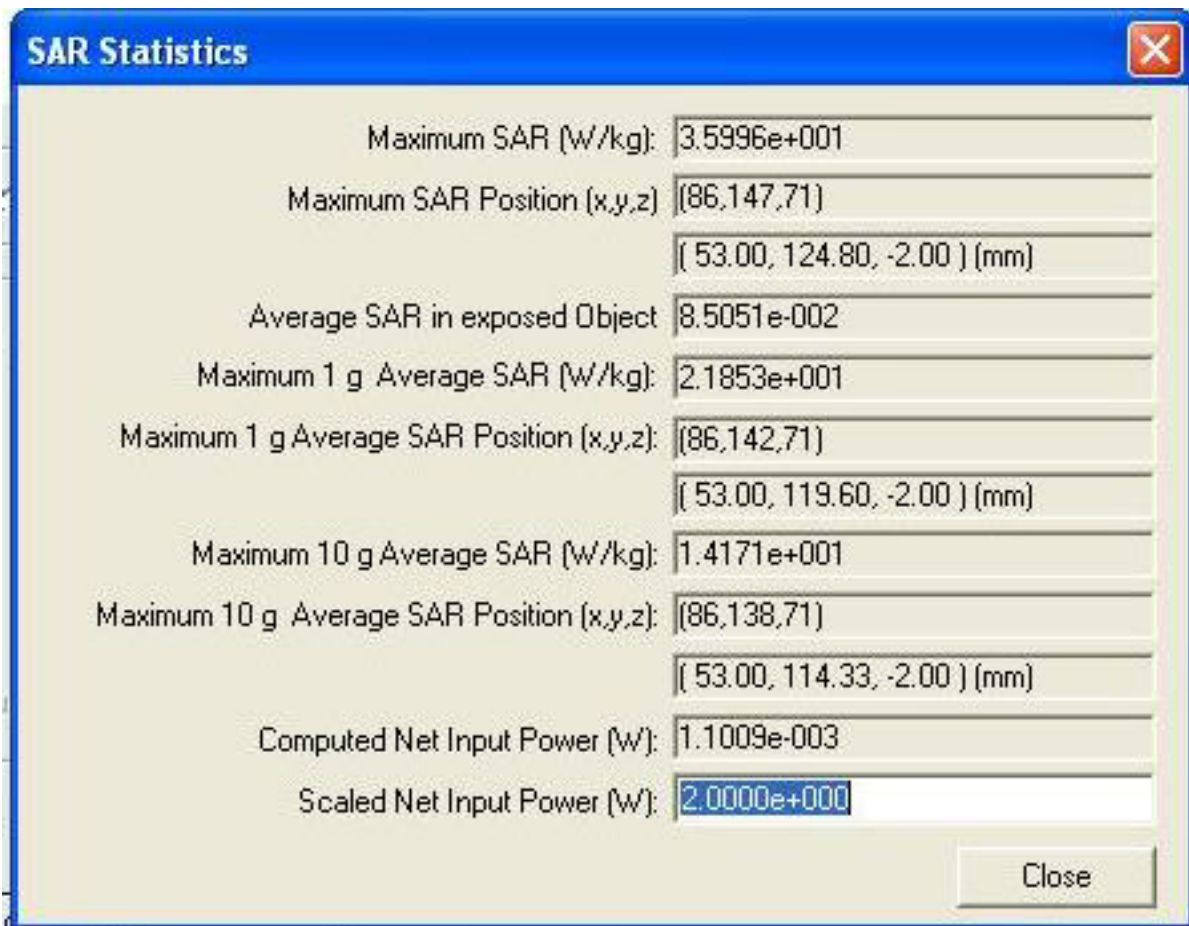


Figure 3-28. SAR for 1 gram average violating the safety guidelines by exceeding 1.6W/kg.

Summary

This chapter has demonstrated the simulation of three different antenna types that could be applied to transmitting and receiving signals for Biomedical Engineering purposes. The first antenna simulated was a dipole antenna in air that exhibited the standard characteristics expected for an antenna transmitting in air. The next two antenna systems, a folded dipole, which makes the antenna easier to wear on the human body and an Alford loop, which in this case is used as an MRI coil. These two antenna systems were applied to the human body model and saline phantom model. When air was no longer the transmission medium, the far field radiation patterns

experienced perturbations. Another factor resulting from use of antennas on the body is the necessity to look at the specific absorption rate.

While simulations provide a useful data, they do not correspond identically to real world conditions, this was evidenced by the folded dipole and the MRI coil which were physically built prior to simulation, known values were plug in and the closest first attempt was within 10%, however, achieving a 1% accuracy in frequency and impedance was an arduous task. Therefore, it is essential to compare real world measurements to simulation, in the next chapter; a phantom will be built to attain this goal.

CHAPTER 4 PHANTOM CONSTRUCTION, TESTING AND ASSESSMENT

Introduction

Any biomedical or electrical engineer that deals with RF fields and human body interactions needs to incorporate phantoms into their development work. This is because of strong interactions between biological materials and the circuit antenna's electromagnetic field. Standard phantoms such as bottles of saline fail to mimic biological interactions because of the water's high dielectric constant and homogeneous nature. The permittivity shortens the electrical wavelength in the phantom. Therefore a new approach needs to be taken in the construction of phantoms.

Prior to phantom construction, in depth thought was put into the phantom construction, including how verify and validate the phantom upon its completion. It was determined that the phantom should be very similar to the human in the REMCOM body model as the access to this model was readily available at UF, thereby allowing an empirical measurement of heating to be compared to a simulation. In recent models, new body models have been introduced of a Korean male, female and child, and while different sized phantoms would probably fit into future research, it is not necessary for the current work. From the RECOM model, measurements were made of the human torso to determine the proper physical size of the phantom. Based on the size of the Torso and the area required for testing (upper torso, under the arms to lower abdomen), an acrylic cylinder was heated and shaped to form an ellipse similar to the torso of the human body with an inner diameter x-axis of 14.5" and a y-axis of 11" with a wall thickness of ¼". After determining the size, the next important step was to identify the tissue types in the torso of the human body model, compare them with standard

anatomy for reference and determine the permittivity and conductivity used in the model.

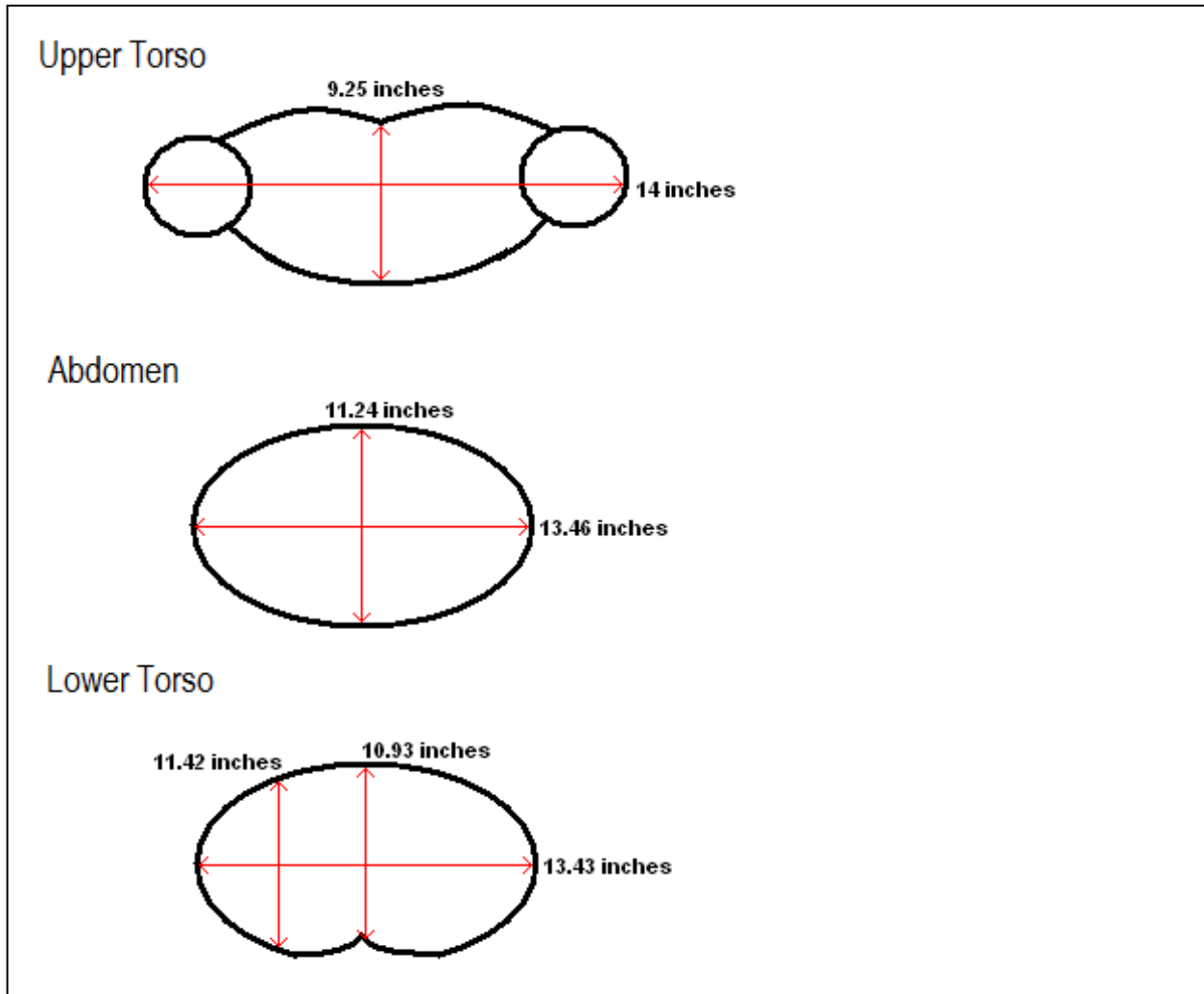


Figure 4-1. Measurements of various geographical locations in the human torso to determine the phantom size requirements based on the REMCOM human body model.

The current challenge lies in using the gels to make concentric rings that have enough rigidity to keep their shape during the construction process. However, prior to constructing a large torso phantom, two smaller phantom boxes were created to see if adding a layer to hold the gel would have any effect on transmission. One phantom had

saran wrap between the sections and the other was constructed with a gel to gel interface, the attenuation of both phantoms were identical, therefore, there are more options for constructing a multilayered phantom

In the torso of the human body model there are only 14 of the 23 available tissue types in the region of interest in the human body model. Based on the available tissue types and similarities, some tissues similar enough to combine, things such as most of the intestinal tissues, organs, etc..., some tissues were left out, such as the skin, which is difficult to emulate at this time, various cartilages, nerves, cerebral spinal fluid. The spinal column and other bones was also omitted due to their relatively low dielectric constant (<20) and conductivity ($<.4$ S/m) to simplify the phantom. The skin deserves a special discussion since it is the first interface on the human body. Currently, the skin is difficult to model, not because of its electrical characteristics, but because of its physical properties, such as being thin, strong and elastic. The phantom being constructed needs a rigid outer structure and therefore skin was replaced with plastic. In the case of torso phantom, acrylic was used to replace the skin and while acrylic does not have the electrical properties of skin, therefore, the skin which is very thin in comparison to most other structures and should have a negligible effect on the electromagnetic wave traveling to deeper structures.

Table 4-1. The table above shows the electrical parameters of skin versus an acrylic outside sheet used for phantom construction.

Tissue	Epsilon	Sigma
Skin (Dry)	41.329163	0.871733
Skin (Wet)	46.021198	0.850166
Acrylic	2.8 - 4	< 0.000001

While the goal is to develop a complex phantom to be used in conjunction with the simulations, certain sacrifices had to be made in order to construct the phantom. It is the goal of this phantom is to add significant complexity to mimic the human body while keeping the structure simple enough to build.

The tissues proposed in the torso phantom are the main organs and tissues that take up the most space in the torso, items such as the heart, lung liver, kidneys and intestines are included. Bones like the ribs and vertebral column are omitted and assumed to be taken on by the outer acrylic structure. These assumptions, significantly simplify the construction process for what is already a very complex system. Smaller organs are either lumped in with other mixtures (spleen, kidneys) or organs that lay outside the region of interest are omitted all together, these would include organs, such as the bladder in the lower edge of the phantom and the trachea in the upper half.

The following tissue types are the main types of tissue for this proposed torso phantom and the dielectric parameters and conductivity are computed for 915 MHz according to the 4-Cole-Cole Model described in "Compilation of the dielectric properties of body tissues at RF and microwave frequencies" by Camelia Gabriel in the U.S. Air Force Report AFOSR-TR-96 and are described in Table 4-2 [29-31]. Table 4-3 then describes the mixtures that would be concocted for use in the phantom. Following table 4-3, in the results section is table 4-4 which is the actual measured values of the tissues made for the phantom and used in its construction. The creation of the mixtures used in each layer was a very empirical process. Each attempt to get the proper conductivity for each tissue sample took anywhere from a single deduction up to eight suppositions to arrive at an accurate representation of a particular tissue type. In the

end it was settled on four distinct tissue types to be used in the torso phantom. Upon construction, the phantom was verified to mimic the human body under RF conditions using a reflection measurement and then a transmission measurement.

Table 4-2. Main tissues in the human torso (excluding bone and skin), that are to be used in the human torso phantom.

Tissue	Epsilon	Sigma
Fat	5.459623	0.051398
Fat(Mean)	11.327779	0.110212
Muscle (Parallel Fiber)	56.844746	1.001017
Muscle (Transverse Fiber)	54.996933	0.948091
Trachea	41.970886	0.775645
Lung (Inflated)	21.971907	0.459232
Lung(Deflated)	51.372128	0.863622
Bladder	18.922573	0.385030
Heart	59.796032	1.237872
Liver	46.763901	0.861202
Spleen	57.087086	1.280117
Stomach, Esophagus, and Duodenum	65.019768	1.193225
Kidney	58.557178	1.400791
Small Intestine	59.387680	2.172682
Colon (Large Intestine)	57.865887	1.086821

Table 4-3. Combined tissues used in the human torso phantom.

Tissue	Epsilon	Sigma
Fat	5.459623	0.051398
Average Muscle	55.928037	0.974554
Heart, Liver, Spleen Average	52.828474	1.251955
Abdomen Average	41.970886	0.775645

The muscle layer had a permittivity of 55.1 and a conductivity of 1.03; the heart/lungs/stomach layer had a permittivity of ~60 and a conductivity of ~1.2 (average effects of that area of the body).

Materials and Methods

Measurement of Tissue Equivalent Mixtures

The permittivity (dielectric constant) and conductivities for phantom development are verified using a 85070B dielectric probe kit with software (Agilent, Santa Clara, CA) and a HP8752A vector network analyzer (Hewlett Packard, Santa Clara, CA) as shown in Figure 4-2.

The probe measures the complex relative permittivity ϵ of the mixtures expressed as $\epsilon = \epsilon' - j\epsilon''$ where ϵ' is the relative permittivity of the material and ϵ'' is the out of phase loss factor associated with it. The conductivity, σ , is derived using ϵ'' , where $\sigma = \epsilon'' \epsilon_0 \omega$, and ϵ_0 is the relative permittivity of free space and ω is the angular frequency of the field.



Figure 4-2. This setup shows the coaxial probe mounted in a fixture, which is hooked to the network analyzer and is software controlled via the laptop and on the right is a close up of the probe inserted into a phantom material under measurement. (Photos courtesy of Barbara Beck, AMRIS RF Lab, University of Florida)

The materials that are tested must be >20mm in diameter, be non-magnetic, homogeneous and have a smooth surface that does not have gaps when interfaced to the probe. Each mixture is mixed in about a 500 ml of total volume, and then a small

amount is poured into a cylindrical container that is approximately 40 mm in diameter and 25mm deep.

Four tissue mixtures were prepared through empirical development; those tissues are fat, average abdomen, average muscle, and an average heart, liver, spleen mixture. The results of those mixtures are shown in table 4-3. The next step was the actual phantom construction; an acrylic cylinder was heated and shaped to form an ellipse similar to the torso of the human body with an inner diameter x-axis of 14.5” and a y-axis of 11” with a wall thickness of ¼”. The first layer added to the phantom was a fat layer composed of shortening a semisolid fat typically used in food preparation and is shown against the outer edge of the phantom, held in place by plastic wrap. The next layer added was the lower abdomen, and both are visible in Figure 4-3, along with a separate stomach compartment made of PVC pipe that can be filled or left as an airspace depending upon the experiment.

Table 4-4. Measured average tissues used in the human torso phantom.

Tissue	Epsilon	Sigma
Fat	5.459623	0.051398
Average Muscle	52.569	1.01197
Heart, Liver, Spleen Average	57.0573	1.371084
Abdomen Average	43.3249	0.871451

The next layer to be added was the heart, liver, spleen mixture, which covered over the stomach and lower abdomen was composed of plastic bags doped with Diethylene glycol (DEG), distilled water, NaCl, and TX-151 shown in Figure 4-4 and Figure4-5. Finally, the phantom was filled to the top with the final layer simulating muscles of the upper chest back and shoulders.



Figure 4-3. Phantom construction, outer most layers are acrylic, followed by fat and then plastic wrap, in the bottom of the phantom is the lower average abdomen and the PVC piping on the center and to the left represent the esophagus and the stomach.



Figure 4-4. Heart, liver spleen mixture shown in the plastic bags.

Figure 4-6 shows the completed phantom with the PVC esophagus sticking out for use with studies involving the stomach or alternatively as an access port for any type of

study that would involve putting an RF circuit in the central portion of the body. The completion of this phantom requires some verification which is demonstrated and discussed in the next section. The phantom is verified through both reflection and transmission measurements and is compared against saline and the human body.



Figure 4-5. Another view showing the central organ mixture of heart liver and spleen, demonstrating the concentric nature of the phantom.

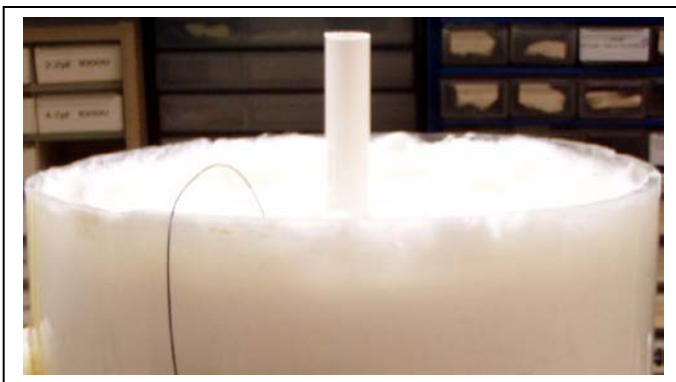


Figure 4-6. Final muscle layers filling in the area between the fat and the central organs, topping off the phantom with upper chest, back and shoulder muscles.

Results

Phantom Confirmation via Reflection Measurements

Upon completion of the phantom, a test was performed to demonstrate the electrical loading of the phantom torso versus a human torso. The test devised to exhibit equivalence between the phantom and the human body was a reflection measurement. An MRI coil that had been tuned and matched to a 90kg human body at 915MHz, which is similar the human body used in the REMCOM model was used. The measurement was made using an HP 4396B vector network analyzer on a human subject, with approximately with a ¼" spacing. A ¼" pad was placed between the subject and the coil to account for the 1/4" wall thickness of the phantom. The identical reflection measurement was then made with the MRI loop placed directly against the tissue equivalent phantom (TEQ). In the Figures below are the results showing very good agreement between the human subject and the TEQ phantom. The performance of the TEQ phantom can be verified via bench measurements and simulation utilizing electromagnetic field simulators. As shown below, a vector network analyzer was used to demonstrate the difference between real human tissue shown in blue on Figure 4-7 and a crude bulk loading phantom filled with a 1S/m saline solution (average conductivity of most muscle and organ tissue) shown in red on Figure 4-7. The deep "dip" or reflection (S_{11}), demonstrates good tuning and matching on the human load, when the same antenna is applied to the bulk loading phantom (saline box), the S_{11} parameters show poor agreement with the actual human load. This can be rectified through better phantom design and is demonstrated by the tissue equivalent phantom used to make the reflection measurements shown in green on Figure 4-7.

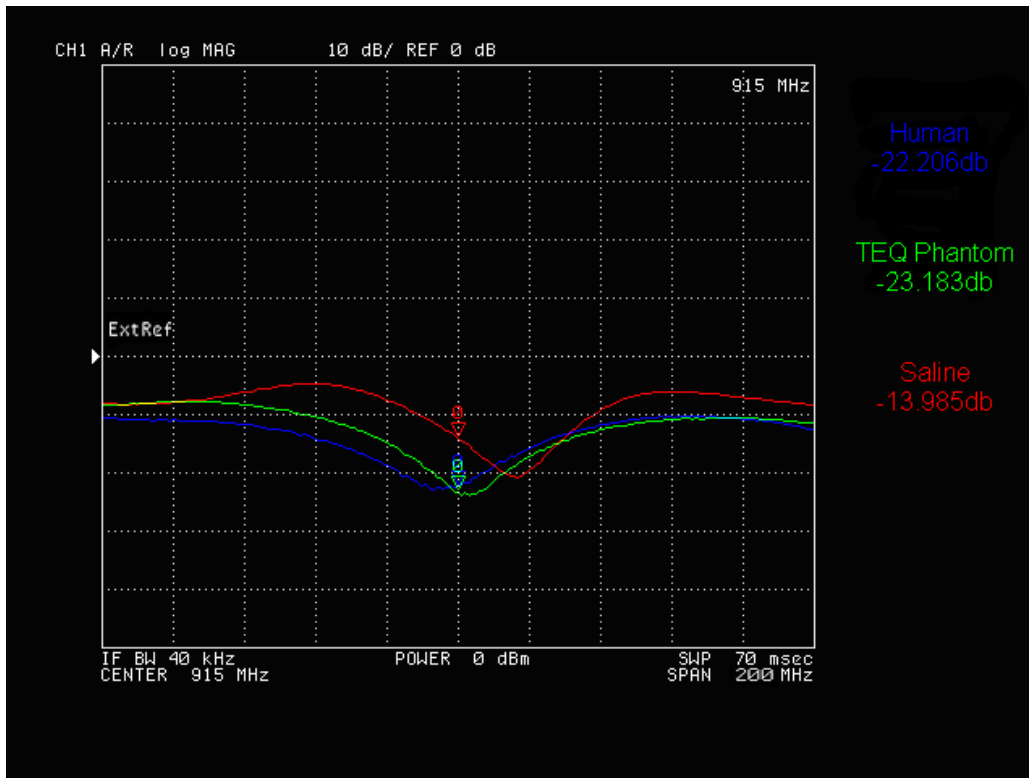


Figure 4-7. A 45 mm MRI surface coil matched to the human body in blue, the tissue equivalent phantom in green and the 1 S/m saline phantom in red at 915MHz.

Additionally, a folded dipole antenna was tuned and matched to a 90kg human body at 915MHz, the tuning and matching was within 1% of the simulation on the human body model used in the REMCOM and was also tested on phantoms via reflection measurement. The measurement was made using an HP 4396B vector network analyzer on a human subject, with approximately with a ¼” spacing. A ¼” pad was placed between the subject and the coil to account for the 1/4” wall thickness of the phantom. The identical reflection measurement was then made with the folded dipole placed directly against the phantom. In the Figures below are the results showing very good agreement between the human subject and the TEQ phantom. The performance of the phantoms can be verified via bench measurements and simulation utilizing

electromagnetic field simulators. As shown below, a vector network analyzer was used to demonstrate the difference between real human tissue and a crude bulk loading phantom filled with a .9% saline solution. The deep “dip” or reflection (S_{11}), demonstrates good tuning and matching on the human load shown in blue on Figure 4-8. However, when the same antenna is applied to the bulk loading phantom (saline box), the S_{11} parameters shown in red on Figure 4-8 demonstrates poor agreement with the actual human load. Although the matching is better with a folded dipole compared to the MRI coil (probably due to its surface area), the quality factor of the match is poor as demonstrated by the wide bandwidth compared to the human and the tissue equivalent phantom shown in green on Figure 4-8.

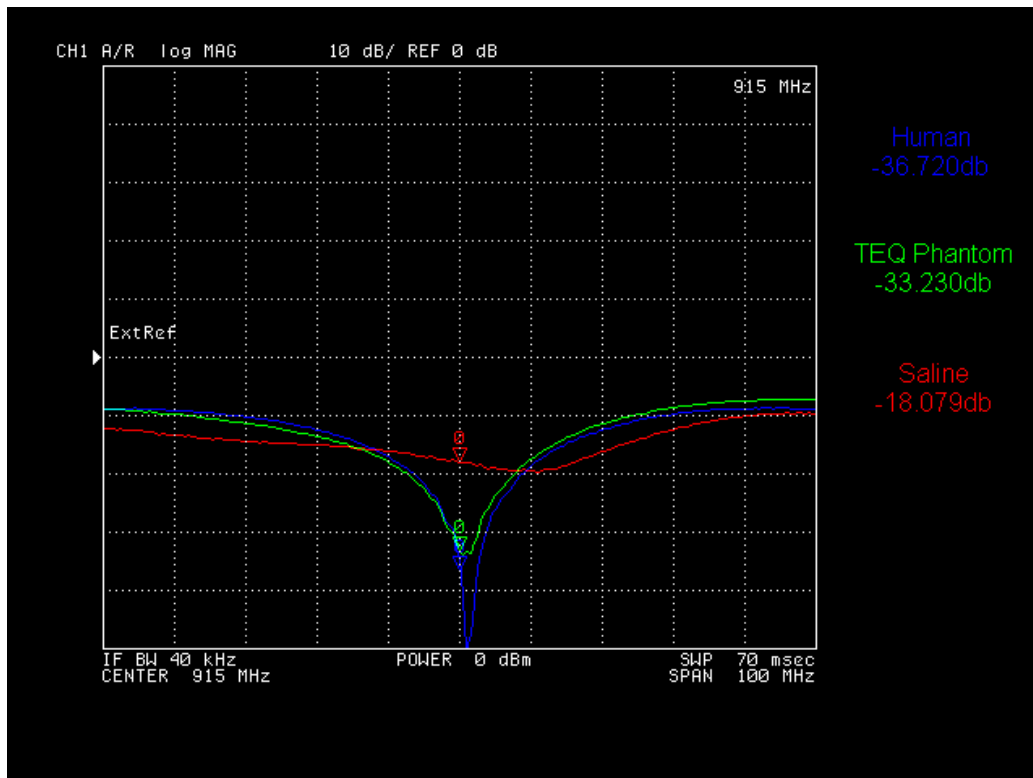


Figure 4-8. Folded dipole tuned and matched to the human body in blue, the tissue equivalent phantom in green and the 1 S/m saline phantom in red at 915MHz.

Phantom Attenuation Using A VCO To Determine Losses When Transmitting Signals From Inside The Body And Receiving Signals Outside The Body

Simulation has shown that there is approximately 40 dB of attenuation in each direction (80 dB for a round trip) [70]. The purpose of these experiments was to confirm or disprove the losses associated with the human body that have been shown through simulation by transmitting from inside a medium and receiving the signal outside the medium. Three mediums were used, a saline phantom, the tissue equivalent torso phantom and a human volunteer.

Materials and Methods

A VCO and antenna setup was constructed using a Crystek VCO that has the following properties: a frequency range of 770-870MHz, phase noise @ 100kHz - 104dBc/Hz, 2nd harmonic -10dBc, Power =3.0 +/- 2.0 dBm with a source of 5V and 12mA. (<http://www.crystek.com/microwave/admin/webapps/welcome/files/vco/CVCO33CL-0770-0870.pdf>). The antenna was custom patterned dipole antenna designed by Hong Yu at the University of Florida (UF) and put on a polyimide substrate with 1 oz copper (Uniflex, San Jose, CA). The antenna was matched at 50 Ohms to the VCO using an L network.

Measurements were made using an Agilent Technologies (Santa Clara CA) 4396B RF Network/Spectrum/Impedance Analyzer, 100 kHz to 1.8 GHz/2 Hz to 1.8 GHz used in the Spectrum Analyzer mode and having the following properties: Frequency range: 2 Hz to 1.8 GHz, -147 dBm/Hz sensitivity @ 1 GHz , Lower than +/- 1.0 dB level accuracy (<http://cp.literature.agilent.com/litweb/pdf/5965-6311E.pdf>) and the 3 cm H-field loop (902B) from an ETS-Lindgren E&H Near Field Probe Set Model 7405 (Cedar Park, TX) that has

29dB of E/H rejection and an upper resonant frequency of 1.5GHz (<http://www.ets-lindgren.com/pdf/7405.pdf>).

The first experiment consisted of a saline phantom with a permittivity of ~77 and a conductivity of one Siemens/meter (1S/m). The H-field probe was fixed to the outside of the saline phantom to prevent errors from movement; the VCO/antenna setup was wrapped in plastic to prevent fluid ingress and immersed in the phantom at 15 cm.

Experiment two was identical to experiment one, except that a gel tissue equivalent phantom with varying permittivity and conductivity for different tissue segments was used. The gel phantom had four layers, consisting of fat, lower abdomen, muscle.

Experiment three, consisted of a human volunteer and the VCO was also “swallowed” while contained in the nasopharyngeal tube, measurements were made and then the tube containing the VCO was removed. According measurements of the human body, it was calculated that the esophagus was between 12 and 15 cm away from the chest wall.

Results

Table 4-5. Transmission attenuation through various mediums

Object	Distance	Attenuation
Saline Box Phantom	~15cm	35dB
Tissue Equivalent Phantom	~15cm	34dB
Human Volunteer	~12-15cm	34dB

Conclusions

In this case the saline and gel phantoms are in good agreement with the simulations that suggests there is approximately 40dB of signal loss when transmitting from deep structures. The human subject compared to the phantoms also demonstrates this; however, there is not a good measurement for the depth of the VCO

in the human, but on the subject used it is expected that it was ~12 -15 cm deep and agrees with the phantom measurements.

CHAPTER 5 COMPARISON OF SIMULATION AND PHANTOM RESULTS

Introduction

The phantoms were compared to the simulations. A few tests were devised to check the phantom versus a person for electrical loading and transmission attenuation characteristics. While the TEQ results modeled a human body well, the true test for a phantom is to be able to confirm an SAR simulation; this is done via a heat test.

In order to evaluate the field distributions and SAR of the transmitting antenna placed against the human body, in the above FCC regulated frequency band (ISM 902-928 MHz, center frequency at 915 MHz) the finite difference time domain (FDTD) method was employed. To confirm the SAR simulation, an antenna was tuned and matched at the desired frequency and 2W of power was applied to the antenna. The SAR measurement procedure via the calorimetric method as stated in IEC 600-601-1 was used to compare to the simulations and SAR results from the FDTD method.

Description of the Experimental Setup

The SAR measurement procedure described in IEC 60601-1 is the basis for the procedure used to confirm the SAR simulations in chapter 3. The phantom used must not exceed 25 liters. Two phantoms were evaluated, the first phantom used for these studies was the tissue equivalent phantom and it contained approximately 22.5 liters of material and the filler material weighed 21.3kg. The second consisted of a plastic box containing 10 liters of 1 S/m of saline solution and weighing 10.01 kg. The basic steps include measuring the temperature of the environment of the working area, measuring initial the temperature of the phantom which must not vary by more than 1° C. The temperature measurement system must be capable of measuring accuracy .1° C and

the object must remain under test until a temperature rise of 20 times the measurement accuracy is obtained, therefore a 2 ° C rise needs to be observed to ensure accuracy. Upon reaching the final temperature, the room temperature must again be measured, if it varies by more than .5 ° C, then the experiment should be repeated under more stable conditions. Upon reaching at least a 2 ° C rise, the energy can then be calculated.

$$E = M \times c \times (T_f - T_i)$$

Where E equals the energy, M equals the mass of the phantom in kg, c equals the specific heat of the phantom in J/kg °C, which for human tissue is .85 and T equals the temperature in °C. Saline has range for the specific heat of .7 to .9 J/kg °C, to keep with the assumption that saline is a good predictor of the human body, a specific heat of .85 J/kg °C . After the energy is calculated, the average power is calculated.

$$P = E/t$$

Where P is the average power in Watts, and t is the total acquisition time in seconds. After this the SAR can be calculated.

$$SAR = P/M$$

Where P is the average power applied in Watts which is divided by the mass of the area where in the SAR is calculated. In this case the mass is equal to 1 gram or .001 kg.

Identical setups were used for the folded dipole and the 45mm MRI coil and are shown in Figures 5-1 through 5-4 for the tissue equivalent and saline phantom.

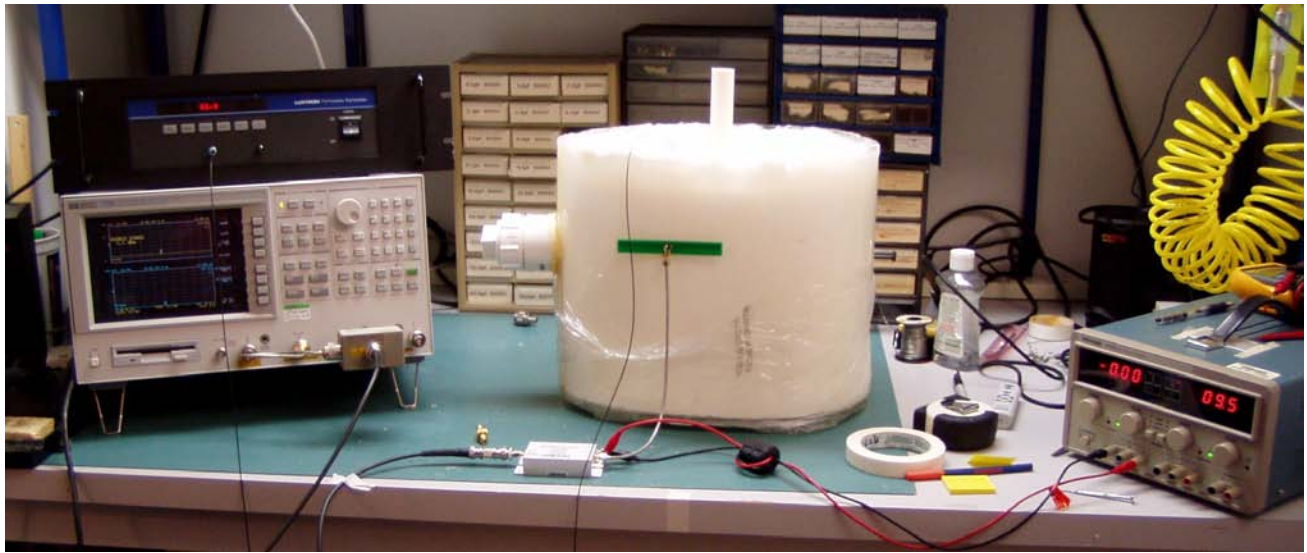


Figure 5-1. Folded dipole matched to the human body placed on the tissue equivalent phantom at 914 MHz with a 2W sinusoidal waveform applied.



Figure 5-2. MRI coil matched to the human body placed on the tissue equivalent phantom at 915 MHz with a 2W sinusoidal waveform applied.

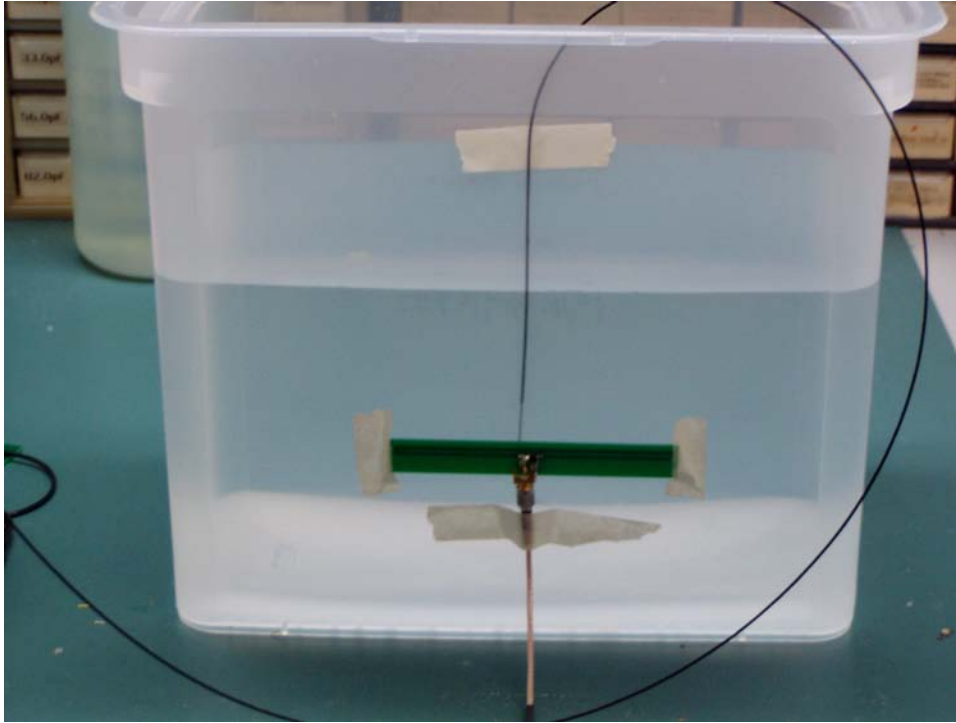


Figure 5-3. Folded dipole matched to the human body placed on the saline phantom at 914MHz with a 2W sinusoidal waveform applied.

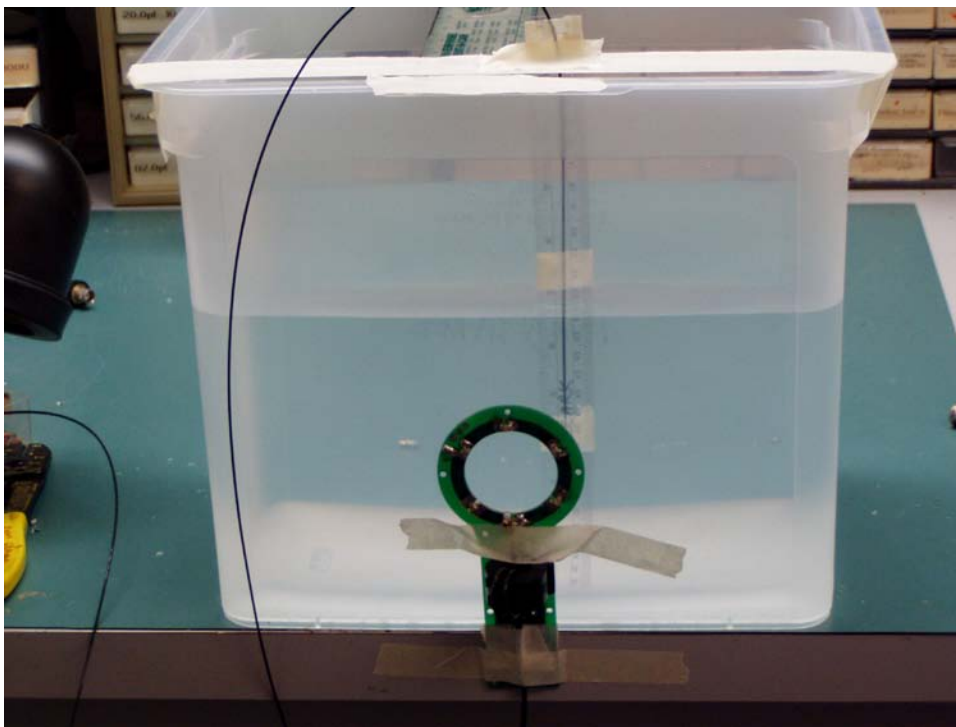


Figure 5-4. MRI coil matched to the human body placed on the saline phantom at 904 MHz with a 2W sinusoidal waveform applied.

Results

The temperature of the laboratory at the beginning of the experiment was 22.5 °C; the initial temperature in the tissue equivalent phantom was 22.8 °C. Initially the fiber optic probe was placed at depth of 3.9 cm from the dipole antenna where the maximum SAR was observed in the simulation. The phantom was allowed to cool and the experiment was repeated for the MRI coil, where the probe was placed at a depth of 4.4 cm from the MRI coil as this area was shown to have maximal SAR in the simulation. The tissue equivalent phantoms required 90 minutes to reach the required greater than 2°C of temperature rise.

The temperature of the laboratory at the beginning of the saline heating experiment was 23.8 °C; the initial temperature in the saline phantom was 24 °C. Initially the fiber optic probe was placed at depth of .6 cm from the dipole antenna where the maximum SAR was observed in the simulation on the surface of the phantom. The phantom was allowed to cool and the experiment was repeated for the MRI coil, where the probe was placed at a depth of 2 cm from the MRI coil as this area was shown to have maximal SAR in the simulation. The saline phantoms required 90 minutes to reach the required greater than 2°C of temperature rise for the dipole antenna, however, the MRI coil took 120 minutes to reach the threshold to perform and SAR calculation.

Folded Dipole Heating and SAR in the Tissue Equivalent Phantom

The folded dipole showed a 3.1 °C degree rise over a 90 minute period, which corresponded to a 1g SAR of 10.4 W/kg for the 21.3kg phantom, which is close to the simulation prediction of 9 W/kg, making the measurement within approximately 15% of the simulation.

Folded Dipole Heating and SAR in the Saline Phantom

The folded dipole showed a 2.5 °C degree rise over a 90 minute period, which corresponded to a 1g SAR of 3.9 W/kg for the 10.01 kg phantom, roughly double the simulation prediction of 2 W/kg. However, this was probably due to thermal conduction as well as RF fields because the dipole input was very warm and the proximity of the calculated hotspot was close to the surface of the phantom.

MRI Coil Heating and SAR in the Tissue Equivalent Phantom

The MRI coil showed a 2.6 °C degree rise over a 90 minute period, which corresponded to a 1g SAR of 7W/kg versus the 5.9W/kg that was predicted via simulation. This equates to a roughly a 19% error between the estimated and the measured.

MRI Coil Heating and SAR in the Saline Phantom

The MRI coil showed a 2.1 °C degree rise over a 120 minute period, which corresponded to a 1g SAR of 2.5W/kg versus the 1.9W/kg that was predicted via simulation. This equates to a roughly a 32% error between the estimated and the measured.

Conclusions

The measurements versus simulations are accurate for the tissue equivalent phantom and deviations in the accuracy are probably due to human error in placing the probes along with sub-optimal simulation performance. However, this study has shown that a phantom developed from basic tissue parameters does mimic the simulation giving both confidence in segmented tissue equivalent phantoms and associated simulations. Saline phantoms on the other hand had much greater errors when

compared to the simulations of saline, and in no way accurately represented the human body in the 900MHz band.

CHAPTER 6 EXAMPLE APPLICATIONS APPLIED TO PHANTOMS

Introduction

The majority of this work focused on the development of a segmented tissue equivalent phantom, however, in the beginning stages of the project it was necessary to use “bulk” loading saline phantoms, these applications will be shown along with results in the tissue equivalent phantom. The specific applications that this phantom development is applied to is medication compliance through electronic pill monitoring in the ISM band of 902-928 MHz and MRI coil results at 900 MHz to determine the effectiveness of the tissue equivalent phantom for specific animal applications at 900 MHz.

Medication Compliance Through The Use Of a Passive Electronic Pill

The field of medication compliance is extremely important in many facets of medicine, particularly in mental health, addiction medicine, geriatric and pharmaceutical clinical trials [71-76]. However, the only proven method for accurately determining medication compliance is through direct observation by medical personnel who are present during ingestion by the patient. Even new methods suggested, such as a fast dissolving tablet [77], in the pharmacology arena still require direct observational therapy in order to determine compliance. While this technique is labor intensive, it is effective, however the adherence rate is still only approximately 80% [78, 79]. However, a rapidly growing biomedical engineering field is *In vivo* biotelemetry [2-7, 10, 13, 16, 23, 80], which may provide the next major breakthrough in medicinal compliance monitoring, logging data that can be remotely assessed by the clinician or study coordinator. In particular, proven medicinal compliance will benefit and greatly reduce

the costs associated with FDA approval of pharmaceuticals (average cost of drug development is over \$800 million per drug, due to regulations and the clinical trial period that is required by the FDA) [81]. It will also provide improved data for accurate determination of the probability of side effects associated with the medication under test. As the population in general ages, as well as the increased number of medications per patient, a reliable technology that can ensure medication compliance with a convenient portable device that monitors, reminds, distributes and communicates with the patient's physician will directly benefit society as a whole through remote monitoring or by having the patient bring the device to the next office visit. Lastly, this technology can be applied to certain populations of mental health and/or addiction patients that require dedicated care. This will ensure that they are properly and accurately medicated through remote monitoring. All of these applications and others will benefit from the development of new technology, specifically, biodegradable passive miniature circuits which will be an important step toward the future of bio-implantable chips and sensors.

RFID: Translation to Biomedicine and the Use of Far Field Electromagnetic Radiation

One of the most powerful techniques available for tracking goods in many service industries, such as purchasing, distribution logistics, industry, manufacturing, material flow and retail is automatic identification (Auto ID) procedures that were revolutionized by the bar code and optical reader. A subset of Auto ID technology is Radio Frequency Identification (RFID) tracking can be applied to the same industries, but with greater utility for expansion based on using a silicon chip [82]. The move to biomedicine can be seen in the animal industry where these biocompatible devices using inductive coupling

for communication are implanted for the purpose of identification [10, 82]. While the vast majority of RFID relies on inductive coupling as the method of transmission [2, 5, 80, 82], new topologies have arisen that force one to transmit using far field electromagnetic radiation [82, 83]. At higher frequencies, i.e. 902-928 MHz of the ISM band, the near field is contained in a $\lambda/2\pi$ sphere which is approximately equal to 5.22 cm at 912MHz [42, 56]. For applications that need detection or communication beyond this point ($R=2D^2/\lambda$), the far field must be used [64].

Therefore, it stands to reason that a method for tracking medications in humans is possible through the use of RF technologies using far field radiation techniques for the purpose of medication compliance and needs to be investigated. In order to consider the use of far-field radiation as a viable means in medication compliance, we must take into account the Federal Communications Commission (FCC) regulations [50] and Food and Drug Administration (FDA) guidelines [52].

There are three primary bands designated by the FCC for medical devices and 3 recognized regions, where Region 1 comprises Europe, Africa, the Middle East west of the Persian Gulf and including Iraq, the former Soviet Union and Mongolia, Region 2 covers the Americas and some of the eastern Pacific Islands and Region 3 contains most of non-former Soviet Union areas of Asia east of and including Iran, and most of Oceania[84]. The three bands can be described as follows, the unlicensed band for use in the human body of 402-405 MHz for Medical Implant Communications Systems (MICS), the Wireless Medical Telemetry Service (WMTS) Equipment operating in the WMTS bands (608-614 MHz, 1395-1400 MHz, and 1427-1432 MHz) is operating under primary status, and therefore, protected from interference by other devices and the

Industrial, Scientific and Medical (ISM) bands operating at 7.765-6.795 MHz, 13.553-13.567 MHz, 26.957-27.283 MHz, 40.66-40.70 MHz, 433.05-434.79 MHz in Region 1, 902-928 MHz in Region 2, 2.4-2.5 GHz, 5.725-5.875 GHz and various other bands extending to 245 GHz [82]. However, many of these would be impractical for use in the human body due to the body's suppression of the short free space wavelength [26, 41, 85], which becomes even shorter in the body reducing the transmit efficiency by damping the electromagnetic radiation.

Individual countries' use of the bands designated in these sections may differ due to variations in national radio regulations. In the United States of America ISM is governed by Part 18 and Part 15 of the FCC rules; however my discussions with the FCC have indicated that this device will fall under Part 15 rules [86]. While there are defined bands for medical needs, they may not be the best bands for passive devices that can be implanted or pass through the human body. Some reasons why the lower frequency bands are not a good option is because of the extra high capacitance values required for resonating the passive pill antennas or alternatively, the large size required for a pill antenna because of long wavelengths. Another option when considering the implementation of such devices is the use of the WMTS band because WMTS is the only frequency spectrum designated exclusively for wireless medical telemetry systems. However, development in this band could be problematic because hospitals deploying telemetry systems in the WMTS bands must ensure that device registration has been completed before the equipment is operational and this also limits the scope of where the device could be used.

The ideal detection scheme is a completely passive device that is detected via an externally applied power. However, many challenges exist in this area. In order to improve signal detection, the radio frequency radiation of the device to be detected needs to be increased. When electrically small antennas are used (8mm x 15mm capsule) they have poor efficiency when compared to their full-size counterparts. As the antenna size decreases, the radiation resistance also decreases in comparison to the Ohmic losses. However, when an antenna is self resonant or forced to resonate, the antenna becomes purely resistive which can improve bandwidth and add control to the radiation pattern[87-89]. Radiation resistance also increases with frequency, so determining the highest optimal frequency that will not be suppressed by the conductivity of the human body is an important aspect. An additional factor that needs to be addressed is the detection of the pill regardless of its orientation. This may entail multiple antenna modes on the pill (i.e. quadrature), or this may be addressed by a multiple receiving antenna setup.

Fundamental Operating Procedures of the Proposed Passive RF Detection System and its Theory of Operation

The entire system is a 1-bit transponder. It consists of a passive “pill” antenna system, a transmitter and receiver. Specially designed transmit and receive antennas are used with the transceiver and an external computer for monitoring and data processing was employed. The pill antenna had to be isolated either electromagnetically, through time shift, or phase shift in order to detect the presence of the pill located between transmit and receive antennas which were separated by 20-30 centimeters. The electromagnetic method uses either the antenna pattern or polarization to enhance detection of the pill antenna. The time-shift method could utilize

ringing in the pill antenna if it has a high-Q tank circuit. However, these type of schemes require pulsed transmit and detection similar to a spectrometer. Alternatively, the time shift method could use an active device to store the incoming energy and then re-transmit after the pulse had ended [39, 90-93]. In this case, a phase sensitive detection experiment is proposed. Where the transmit system consists of a swept source, power amplifier, and a transmitting antenna. The pill is a resonant loop (tank circuit) structure and the receiving system consists of a receiving antenna, preamplifier, double balanced mixer, a low pass filter a data storage and display device (oscilloscope).

In terms of implementation, the phase shift method seems to be the most straightforward method with a high probability of success. In this method, transmit antenna sends out a sine wave at $f \sim 900$ MHz. The transmit and receive antennas are broadband with a Q of < 5 while the pill antenna has a much higher Q of ~ 100 . This method requires phase sensitive detection where the received signal is mixed down to baseband using either the in-phase or quadrature component of the transmitted signals and then the signals are low pass filtered [90]. The received signal, S_R , can be represented as

$$S_R(t) = A_1 \sin(2\pi f_0 t) + A_2 \sin(2\pi f_0 t + \delta(f)) ,$$

Where A_1 and A_2 are the amplitudes of the received signal directly from the transmit antenna and from the pill antenna, respectively, where, A_2 is significantly smaller than A_1 by a factor of 10 or more. The phase shift is produced by the pill tank circuit. We can write δ by modeling the tank circuit as a capacitor, inductor, and resistor in series.

$$\delta(f) = \pi + \tan^{-1} \left[\frac{2\pi fL - \left(\frac{1}{2\pi fC} \right)}{R} \right],$$

Where the values for the resistor, inductor and capacitor are: $R \sim 1\Omega$, $L \sim 20\text{nH}$, and $C \sim 1.6\text{pF}$. The π phase shift is produced by Lenz's Law, which states that an electromagnetic field interacting with a conductor will generate electrical current that induces a counter magnetic field that opposes the magnetic field generating the current. (Note: To improve accuracy of the calculation, we could also include a capacitor in parallel with the resistor and inductor to represent the self-resonance of the pill coil - this will produce a more complicated phase shift but won't add much to the discussion).

In the case of direct detection, on resonance, the pill signal will be 180 degrees out of phase with the transmit signal and the received signal will have a dip corresponding to the pill resonance. The received signal is:

$$\begin{aligned} S_R(t) &= A_1 \sin(2\pi f_0 t) + A_2 \sin(2\pi f_0 t + \delta(f)) \\ &= A_1 \sin(2\pi f_0 t) + A_2 \sin(2\pi f_0 t) \cos(\delta) + A_2 \cos(2\pi f_0 t) \sin(\delta) \end{aligned}$$

Exactly on resonance ($\delta = \pi$), the received signal will be

$$S_R(t) = (A_1 - A_2) \sin(2\pi f_0 t)$$

Since A_1 is so much bigger than A_2 , it may be hard to measure this dip in the frequency response using a network analyzer. However, after mixing with the quadrature (90 degree shifted) component of the transmit signal, the received and mixed signal, S_M , can be represented as:

$$\begin{aligned} S_M(t) &= \left[A_1 \sin(2\pi f_0 t) + A_2 \sin(2\pi f_0 t) \cos(\delta) + A_2 \cos(2\pi f_0 t) \sin(\delta) \right] \cdot \cos(2\pi f_0 t) \\ &= \left[\frac{A_1}{2} \sin(4\pi f_0 t) + \frac{A_2}{2} \sin(4\pi f_0 t) \cos(\delta) + \frac{A_2}{2} \sin(\delta) + \frac{A_2}{2} \cos(4\pi f_0 t) \sin(\delta) \right] \end{aligned}$$

After we filter out the 1.8 GHz signals by low pass filtering, we end up with

$$S_F(t) \approx \frac{A_2}{2} \sin(\delta),$$

$$\delta(f) = \pi + \tan^{-1} \left[\frac{2\pi fL - \left(\frac{1}{2\pi fC} \right)}{R} \right].$$

Where:

The phase shift is shown below.

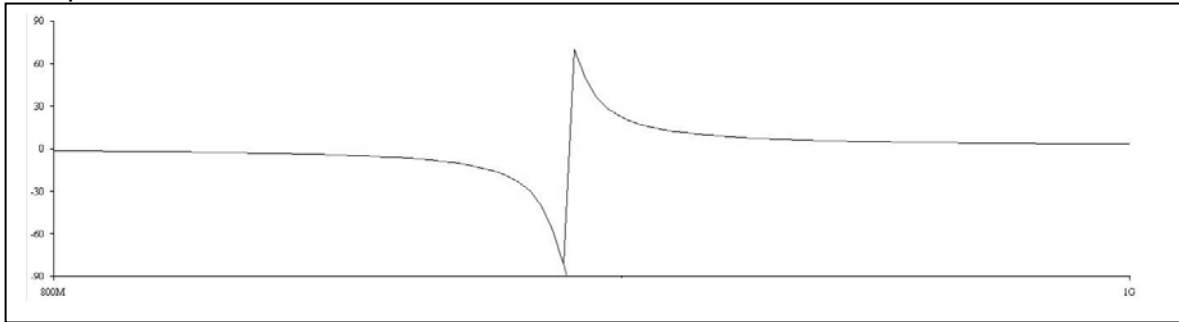


Figure 6-1. The phase detected signal in the time domain after filtering. The distinct peak is the actual transition of a 180 degree phase shift at resonance.

By acknowledging that A_2 is also a function of frequency, because the pill circuit has such a high Q , we could make a more accurate prediction utilizing:

$$A_2(f) \propto \left(\frac{(2\pi)^2 f^2 R}{L^2 (2\pi)^4 (f^2 - f_0^2)^2 + (2\pi)^2 f^2 R^2} \right)^{1/2}$$

It may not be possible to generate a quadrature signal that is exactly 90 degrees out of phase with the transmit signal because of the frequency sweep not having the same starting at the beginning of each sweep, a common occurrence even in modern circuits. If we have a phase error of ε , we end up with a background signal (an unwanted DC offset) represented below showing the phase errors added to the previous equation:

$$S_M(t) = [A_1 \sin(2\pi f_0 t) + A_2 \sin(2\pi f_0 t) \cos(\delta) + A_2 \cos(2\pi f_0 t) \sin(\delta)] \cdot \cos(2\pi f_0 t + \varepsilon)$$

$$= \left[\begin{aligned} &\frac{A_1}{2} \sin(4\pi f_0 t + \varepsilon) + \frac{A_1}{2} \sin(\varepsilon) + \frac{A_2}{2} \sin(4\pi f_0 t + \varepsilon) \cos(\delta) + \frac{A_2}{2} \sin(\varepsilon) \cos(\delta) \\ &+ \frac{A_2}{2} \cos(\varepsilon) \sin(\delta) + \frac{A_2}{2} \cos(4\pi f_0 t + \varepsilon) \sin(\delta) \end{aligned} \right]$$

After filtering via a low pass filter, we end up with the more accurate expression of:

$$S_F(t) = \left[\frac{A_1}{2} \sin(\varepsilon) + \frac{A_2}{2} \sin(\varepsilon) \cos(\delta) + \frac{A_2}{2} \cos(\varepsilon) \sin(\delta) \right]$$

However, if we have a phase error of a few degrees, where the first term, A_1 , may be equal to or greater than the A_2 components, therefore it is extremely important to control the phase of the proposed system. The measurement will consist of a true DC signal and this DC signal is measured by sweeping frequency from 902-928 MHz, amplifying and averaging the response over time [94-96].

Resonance of an Electronic Pill Antenna

In order to characterize a resonant pill, a loosely coupled probe set consisting of 2 H-field probes separated by d (the diameter of each loop) was constructed. Each probe was 2.54 cm in diameter and fixed into a rigid box to ensure standard measurements were made for each resonant circuit. The probe set had isolation between transmission and reception of approximately 30 dB from 300 kHz to 1.3 GHz, the frequency limit of the vector network analyzer that was used. Each loop was tuned to the corresponding the corresponding frequencies in each band and evaluated for realistic values that can be manufactured using our printing methods. From this it was determined that the frequencies of 40 MHz, 138 MHz had to be eliminated because of the extraordinarily high capacitance values required to make the loops resonate at those frequencies. As the frequency goes up the capacitance goes down as described by the formula $f=1/\sqrt{LC}$.

This exercise demonstrates how much capacitance is required for various frequencies and whether these structures can be manufactured without discrete components.

Each trace width value was resonated with a standard 3.0 pF capacitor (American Technical Ceramics, Huntington, NY). The values for various proposed test frequencies were extrapolated and shown in the tables shown on the subsequent pages. Based on the calculations shown in the table on the following pages, all frequencies below 402MHz, the lower cutoff of the MICS band, have been excluded from further study. This is due to their unrealistic capacitor values that would be required for printed capacitance in the circuits. The goal was to find a balance between small antennas and realizable capacitance values that could be printed using silver inks and dielectrics.

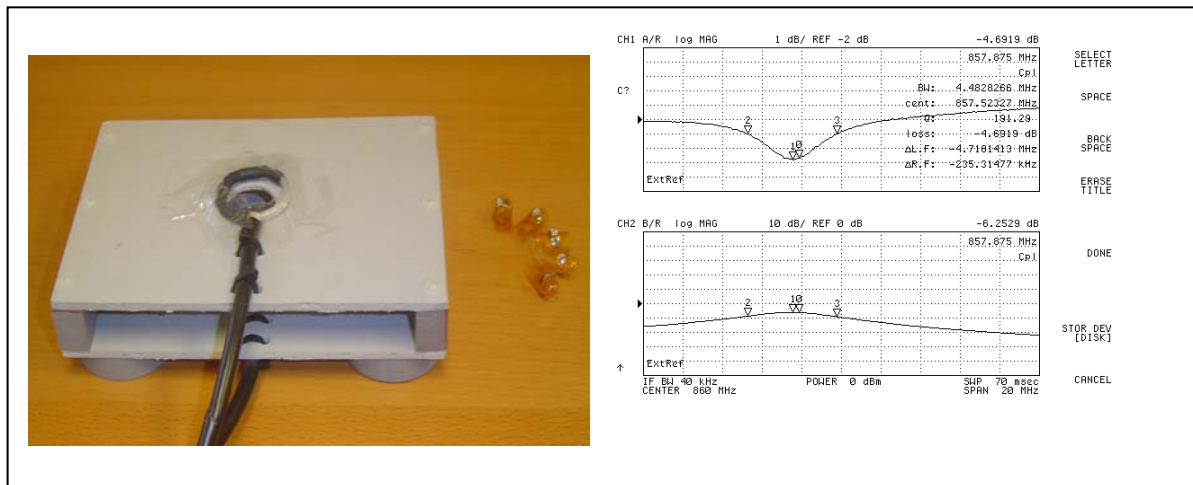


Figure 6-2. Shows the probe set and pills with 1mm – 5mm traces. and on the right is the Q of a 5 mm wide trace pill resonated with a 4.7pF capacitor. The Q of greater than 100 (5mm Q= 191) is typical of all the pills utilizing 1mm – 5mm traces. The Q of the circuit is directly related to the Q of the capacitor with the inductance having a minimal effect.

Table 6-1. Capacitance versus inductance values for a given frequency. *Actual capacitor used, #corresponding frequency.

Inductance (1mm trace width)	Capacitance	Resonant Frequency
+12.5nH	1267pF	40MHz
+12.5nH	109pF	138MHz
+12.5nH	10.8pF	433MHz
+12.5nH	3.0pF*	822MHz#
+12.5nH	2.42pF	915MHz
+12.5nH	1.41pF	1200MHz

Table 6-2. Capacitance versus inductance values for a given frequency. *Actual capacitor used, #corresponding frequency.

Inductance (2mm trace width)	Capacitance	Resonant Frequency
+9.8nH	1608pF	40MHz
+9.8nH	135pF	138MHz
+9.8nH	13.7pF	433MHz
+9.8nH	3.1pF	915MHz
+9.8nH	3.0pF*	926MHz#
+9.8nH	1.79pF	1200MHz

Table 6-3. Capacitance versus inductance values for a given frequency. *Actual capacitor used, #corresponding frequency.

Inductance (3mm trace width)	Capacitance	Resonant Frequency
+8.6nH	1841pF	40MHz
+8.6nH	155pF	138MHz
+8.6nH	15.7pF	433MHz
+8.6nH	3.52pF	915MHz
+8.6nH	3.0pF*	991MHz#
+8.6nH	2.05pF	1200MHz

Table 6-4. Capacitance versus inductance values for a given frequency. *Actual capacitor used, #corresponding frequency.

Inductance (4mm trace width)	Capacitance	Resonant Frequency
+7.5nH	2107pF	40MHz
+7.5nH	200pF	138MHz
+7.5nH	17.99pF	433MHz
+7.5nH	4.03pF	915MHz
+7.5nH	3.0pF*	1060MHz
+7.5nH	2.34pF	1200MHz

Table 6-5. Capacitance versus inductance values for a given frequency. *Actual capacitor used, #corresponding frequency.

Inductance (5mm trace width)	Capacitance	Resonant Frequency
+7.1nH	2228pF	40MHz
+7.1nH	187pF	138MHz
+7.1nH	19.01pF	433MHz
+7.1nH	4.26pF	915MHz
+7.1nH	3.0pF*	1090MHz#
+7.1nH	2.5pF	1200MHz

Empirical measurements in Solution, ISM 902-928 MHz Band

Detection at 912MHz is possible, therefore, miniaturization of the antenna and associated circuits mounted on the outside of the capsule, reserving the inside for the medication.



Figure 6-3. Plot on the left is from a swept source (frequency generator), 908-916MHz, with the transmit and receive antennas placed 30 cm apart no pill transmitting through air, on the right a passive electronic pill is introduced with air as the media. Notice that the total signal rise about 200mV (-0.97dBm) when the pill is introduced.

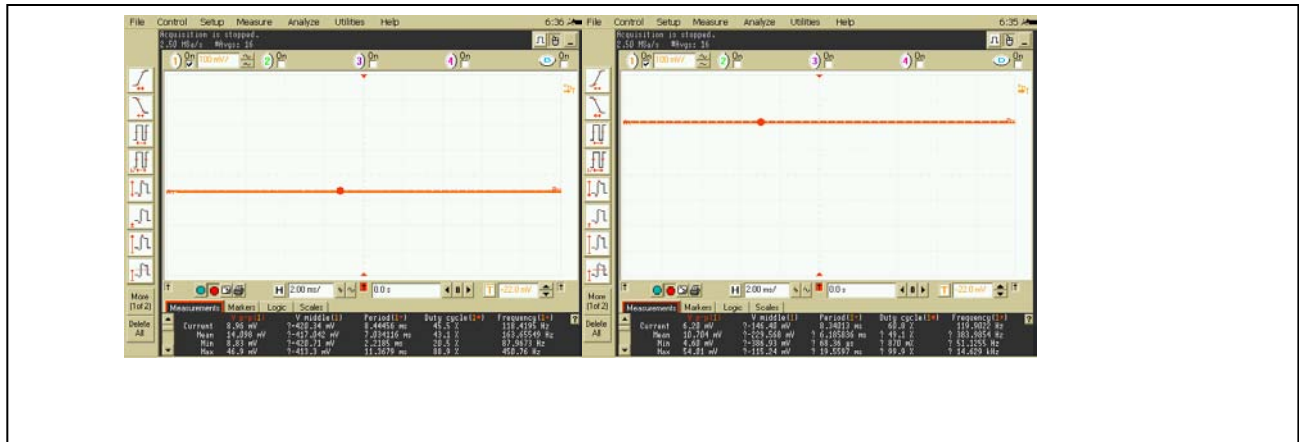


Figure 6-4. Plot on the left shows single frequency transmitted at 912MHz (resonant frequency of the pill) with the transmit and receive antennas placed 30 cm apart, no pill through air, the plot on the right with the pill in air. Notice that there is a 275mV (1.8dBm) change when introducing the pill, which demonstrates detection.



Figure 6-5. Plot on the left shows a continuous wave (CW) at a single frequency of 912MHz (resonant frequency of the pill) with the transmit and receive antennas placed 30 cm apart, no pill in solution and the plot on the right shows the pill in solution. Notice not only is there a change of 90 mV (-7.9dBm), but that it is negative, indicating a change in the direction of the phase when compared to air. This can be corrected by zeroing the phase with the solution in place.

Applications to MRI at 21T (900MHz)

The role of MRI research is almost always directly related to improving image resolution or decreasing the time of the acquisition. Because of this there is always a drive to higher static magnetic field strengths. The result of moving to higher field strengths is an increase in signal-to-noise ratio (SNR), which can then be traded for time or resolution.

MRI theory, Quantum Mechanics of NMR/MRI

Magnetic resonance (MR) is a technique for using the interactions of atoms and molecules with external magnetic fields to extract image and/or chemical data from a sample. In order to use the classical description, first an overview of the quantum mechanics must be given.

In Quantum mechanics, a property of atomic nuclei exists, called a spin. If spin $\frac{1}{2}$ nuclei are placed in an external static magnetic field B_0 , there are only two possible energy states for spin $\frac{1}{2}$, separated by an energy gap, $E = \hbar\omega_0$, that is proportional to B_0 . A quantum mechanical transition between the two energy states, requires a radio frequency magnetic field, B_1 , which is perpendicular to the static field and oscillating at a frequency, ω_0 . The result is what is known as the Larmor equation:

$$\omega_0 = \gamma B_0$$

Quantum mechanics states that the spin does not have to purely reside in one state or the other, but that a spin exists in some linear combination of two states. For simplicity, a statistical-classical description will be used to describe MRI, whereby macroscopic properties of an ensemble of spins are used [97].

Classical Description of NMR/MRI

A classical description of NMR/MRI relies upon the Larmor equation that is shown to be existent using quantum mechanics. The ^1H nucleus that possesses a spin, \mathbf{S} , and a gyromagnetic ratio, γ , which gives rise to a magnetic dipole moment, μ .

$$\mu = \gamma \mathbf{S}$$

NMR uses the spin of the magnetic moment to obtain a signal from the nuclei of interest. The more spins that are available the easier it is to distinguish the signal (which are determined by Boltzmann statistics). The most abundant source in the human body is the hydrogen proton. Hydrogen and other nuclei that possess an odd total number of protons and neutrons (such as hydrogen-1, 1 proton, 0 neutrons, that is also why ^1H imaging is sometimes referred to as proton imaging) possess magnetic moments whereas even-even and odd-odd nuclei have zero net magnetic moment [98].

When a material with the nuclei of interest is placed into a strong and uniform static magnetic field (\mathbf{B}_0), the magnetic field causes the spins to attempt to align with the static magnetic field. At this point, the spins precess around the magnetic field like a spinning top [99].

The nuclei precess at the Larmor frequency, which was described in the previous section on quantum mechanics. The rate of precession, ω_0 , which is measured in radians per second, and \mathbf{B}_0 is the main magnetic field, which is measured in Tesla. One Tesla is equivalent to 10,000 Gauss.

The Larmor equation describes what is referred to as the nuclear magnetic resonance condition, thus explaining the term Nuclear Magnetic Resonance or NMR. However, when NMR became clinically useful for medical imaging, the N was dropped

and changed to MR imaging or MRI, but NMR is still used on vertical spectroscopy systems. For clinical imaging dropping the N was done to prevent fear or confusion from the term nuclear.

The MRI experiment

In the basic MRI experiment, a sample consists of an ensemble of spins, possessing a magnetic moment, which is placed in a static magnetic field (\mathbf{B}_0). A magnetic moment placed in a \mathbf{B}_0 field will experience a torque. This torque will cause the nuclei's magnetic moments to align with \mathbf{B}_0 , and some to align anti-parallel \mathbf{B}_0 , populating the two energy states of the system. Boltzmann statistics predicts that there will be a small net magnetic moment, \mathbf{M} , aligned with \mathbf{B}_0 . This is referred to as net magnetization and is proportional to \mathbf{B}_0 . For higher static magnetic fields, \mathbf{B}_0 , there is more magnetization, \mathbf{M} ; hence there is more available signal. If an external oscillating radio-frequency (magnetic) field (\mathbf{B}_1) with frequency identical to the precession frequency of the nucleus of interest (the Larmor frequency) is applied perpendicular to the static magnetic field (\mathbf{B}_0), \mathbf{M} will absorb energy and tip away from alignment with the static magnetic field. If the \mathbf{B}_1 field is applied for a certain time, the combined magnetization rotates into the transverse plane. After the RF (\mathbf{B}_1) field has ceased, the magnetic moment precesses at the Larmor frequency. During precession, the magnetic moment slowly loses energy to its surrounding. A RF signal is induced in the receiver RF coil (whose \mathbf{B}_1 is in the transverse plane) by the rotating magnetic moment in the transverse plane. The receiver coil can be the same or different from the RF transmitting coil, but both must have \mathbf{B}_1 in the transverse plane. A damped sinusoidal varying signal at the Larmor frequency is then produced and is known as the free

induction decay (FID). In order to produce a RF receive signal, the net magnetic moment must be non-zero [98].

In order to go from NMR spectroscopy to MRI, which is a 1D, 2D or 3D image, gradients must be added in. Gradients are the change in field from the static magnetic field in the positive or negative direction of any plane. For example, if a gradient were applied in the x-direction, the gradient would provide spatial information by slightly changing the Larmor frequency at different locations along x. Thus, frequency encoding the spatial information, such that a Fourier transformation (FT) of the time domain sampled FID, provides a 1D-image projection. If successive FID's were collected after the application of different gradient values in the y-direction, thus varying the phase of the FID, a FT with respect to the phase then gives spatial information along the y-direction. Therefore, a 2DFT method gives spatial information in two dimensions, thus producing a 2D image.

NMR is a non-invasive technique that is sensitive to the molecular environments of the atoms, which has led to Magnetic Resonance Imaging (MRI) via the addition of gradients. Based on this basic discussion of the MRI phenomenon, the problem of this research project can now be described.

The benefits of using extremely high fields in the future such as a 21T Human MRI system (currently only available for small rodents), will be the increased SNR which can then be traded for resolution. The increase in SNR can be used for imaging or in the analysis of metabolites in spectroscopy. While this is still in the distant future, currently an 11.7T human whole body MRI system has been commissioned and there are

currently whole body systems available at 9.4T for research. Therefore the results shown in chapters 3-5 are directly applicable to future MRI systems.

MRI Bench Experiments and Results

The tissue equivalent phantom (TEQ) was compared between a human, a saline loading phantom and demonstrated the usefulness of the TEQ. The electrical loading was demonstrated between the human torso, tissue equivalent phantom and a saline phantom. The test devised to check for equivalence between the phantoms and the human body was a reflection measurement, using a MRI coil that had been tuned and matched to a 90 kg human body at 915 MHz, which is similar the human body used in the REMCOM model. The measurement was made using an HP 4396B vector network analyzer on a human subject, with approximately with a ¼” spacing. A ¼” pad was placed between the subject and the coil to account for the 1/4” wall thickness of the phantom. The identical reflection measurement was then made with the MRI loop placed directly against the phantom. Figure 6-6 demonstrated very good agreement between the human subject and the tissue equivalent phantom. The performance of the phantom was verified via bench measurements and simulation utilizing electromagnetic field simulators. As shown in Figure 6-6, a vector network analyzer was used to demonstrate the difference between real human tissue shown in blue and a crude bulk loading phantom filled with a 1S/m saline solution (average conductivity of most muscle and organ tissue at 900 MHz) shown in red. The deep “dip” or reflection (S_{11}), demonstrates good tuning and matching on the human load, when the same antenna is applied to the bulk loading phantom (saline box), the S_{11} parameters show poor agreement with the actual human load. This can be rectified through better phantom

design and is demonstrated by the tissue equivalent phantom used to make the reflection measurements shown in green on Figure 6-6.

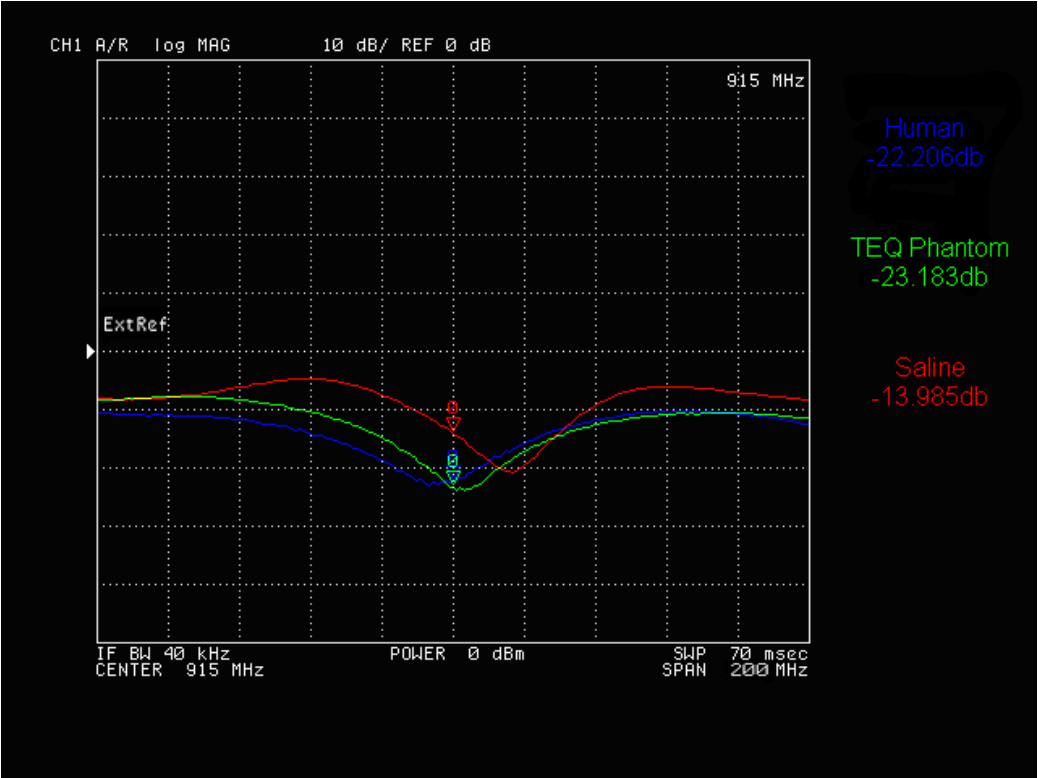


Figure 6-6. A 45 mm MRI surface coil matched to the human body in blue, saline in red and the tissue equivalent phantom in green at 915MHz.

CHAPTER 7 SUMMARY AND FUTURE WORK

Summary

This work demonstrated the need for tissue equivalent phantoms that simulate the electrical properties of a biological system. The work begins with a general discussion about phantoms and their relevance to biomedical applications. This leads into an in depth study of the current standards as applicable to specific absorption rate (SAR) that was later applied to the tissue equivalent phantom. Equipment and procedures for measuring the complex permittivity were discussed. Three distinct types of phantoms for simulating the electrical properties of humans were discussed. The three types of phantoms are a saline phantom, a tissue equivalent phantom and a segmented tissue equivalent phantom. It was shown that the saline phantom breaks down as a good electrical model of the human body at very high frequencies (VHF) and at ultra-high frequencies the parameters are worse with results shown in Figures 4-8. Antenna simulations were performed for two different types of antennas. The first simulation was of a folded dipole at 915MHz, the second simulation was of a 45mm MRI surface coil at 915MHz. These simulations were used to compare simulation against a tissue equivalent and saline phantoms, with the method of comparison being a study of induced SAR.

A tissue equivalent phantom was constructed consisting of four combined tissues to accurately act as a human load. Those four tissues were fat, average muscle, a heart-liver-spleen average and an average abdomen (small and large intestines). These four tissue types were then concentrically placed in the former to electrically simulate human tissue. The next step was to compare the electrical properties of the

phantom versus a human load. Two types of experiments were performed, a reflection measurement and a transmission measurement. In the reflection measurement, the tissue equivalent phantom performed almost identically to the human load, whereas the saline load differed significantly from the human load. The next experiment was a transmission experiment to measure the attenuation of a transmitted source through the same three mediums, human body, saline phantom and the tissue equivalent phantom. All three loads had roughly the same attenuation at approximately 34dB. Upon confirming that the tissue equivalent was electrically equivalent to the human body, an SAR experiment was performed to compare simulation versus experiment.

The SAR experiment made an assumption that the majority of the power transmitted was far-field and utilizing the calorimetric method from IEC 600-601-1, 2W of continuous power was applied to the phantom until a 2 ° C temperature rise was obtained. The SAR was calculated and then compared to the simulations for the folded dipole and the MRI coil case, showing agreement.

This work has shown the usefulness of the tissue equivalent phantom for measurements, testing and empirical analysis of RF interactions with the human body. The tissue equivalent phantom did provide convincing evidence for making RF measurements versus a saline phantom in the 900 MHz range. Although the tissue equivalent phantom did not confirm the exact SAR distribution of the REMCOM simulations of a static human body (no fluid flow), it is the first step toward improving the accuracy of phantom and simulation work. The measurements of the TEQ heat rise and subsequent SAR calculations were within 15% for the folded dipole and within 19% for the MRI coil. Future generations of phantoms should include a lung space; this

should help with some of the complex air-tissue interfaces that are in the human body.

A summary of the results for the MRI coil experiments are shown in Table 7-1 and the folded dipole summary of results is shown in Table 7-2.

Table 7-1. Summary of 45mm MRI coil experiments.

<i>45mm MRI Coil</i>	<i>Human</i>	<i>REMCOM Body Model</i>	<i>Tissue Equivalent Phantom</i>	<i>Homogeneous Saline Phantom</i>
Loading	-22.2 dB	-19.5 dB	-23.2 dB	-14.0
Max SAR 1g	NA	6 W/kg	7 W/kg	2.5 W/kg

Table 7-2. Summary of folded dipole experiments.

<i>Folded Dipole Antenna</i>	<i>Human</i>	<i>REMCOM Body Model</i>	<i>Tissue Equivalent Phantom</i>	<i>Homogeneous Saline Phantom</i>
Loading	-36.7 dB	-16.5 dB	-33.2 dB	-18.1 dB
Insertion Loss	34 dB	~40 dB	34dB	35dB
SAR	NA	9 W/kg	10.4 W/kg	3.9 W/kg

Future Work

Future work should focus upon calculating a relationship between the ingredients of the phantom mixtures and obtain a standard formula that can be applied to phantom development. This would significantly speed up the design and construction of a phantom and also aid in disseminating the use of segmented phantoms for biomedical engineering studies. To improve the accuracy of temperature rise and induced SAR, the next generation phantom should pattern the human body model with more segmentation. A positioning grid should also be added to the phantom in order to accurately position temperature measurement probes or other measurement devices, such as e-field probes. Upon confirming a static model, a phantom should contain some basic fluid flow to simulate the circulatory system of the human body. This improvement could then aid in developing more accurate simulations, thus improving

accuracy of RF absorption studies in general. Future MRI work should focus on a smaller phantom that would fit in the current 21T (900MHz) animal system. MRI images of the phantom and its biological counterpart should be acquired to demonstrate the effectiveness of the phantom as an electrical loading tool for MRI.

LIST OF REFERENCES

1. Cox, D.C., *Wireless personal communications: what is it?* Personal Communications, IEEE, 1995. **2**(2): p. 20-35.
2. Ahmadian, M., et al., *Data Transmission for Implantable Microsystems using Magnetic Coupling*. IEE Proceedings Communications, 2005. **152**(2): p. 247-250.
3. Alomainy, A., et al. *UWB On-body Radio Propagation and System Modeling for Wireless Body-centric Networks*. in *IEE Proceedings Communications*. 2006.
4. Chirwa, C., et al., *Electromagnetic Radiation from Ingested Sources in the Human Intestines between 150MHz and 1.2GHz*. IEEE Transactions on Biomedical Engineering, 2003. **50**(4): p. 484-492.
5. Drysdale, T.D., W. Lei, and D.R.S. Cumming, *In Situ Characterization of Two Wireless Transmission Schemes for Ingestible Capsules*. IEEE Transactions on Biomedical Engineering, 2007. **54**(11): p. 2020-2027.
6. Glukhovsky, A., *Wireless Capsule Endoscopy*. Sensor Review, 2003. **23**(2): p. 128-133.
7. Iddan, G., et al., *Wireless Capsule Endoscopy*. Nature, 2000. **405**: p. 417.
8. Jovanov, E., et al., *A wireless body area network of intelligent motion sensors for computer assisted physical rehabilitation*. Journal of NeuroEngineering and Rehabilitation, 2005. **2**(1): p. 6.
9. Kern, N., B. Schiele, and A. Schmidt, *Multi-Sensor Activity Context Detection for Wearable Computing*. European Symposium on Ambient Intelligence(EUSAI), 2003.
10. Kramer, K. and L.B. Kinter, *Evaluation and Applications of Radio Telemetry in Small Laboratory Animals*. Physiological Genomics, 1988. **29**: p. 1035-1041.
11. Krause, A., et al., *Unsupervised, Dynamic Identification of Physiological and Activity Context in Wearable Computing*. Proc 7th International Symposium on Wearable Computers, 2003: p. 88 - 97.
12. Lee, S.W. and K. Mase, *Activity and Location Recognition Using Wearable Sensors*. Pervasive Computing, 2002. **1**(3): p. 24 - 32.
13. Mackay, R.S., *Radio Telemetry from within the Body*. Science, 1961. **134**: p. 1196-1202.

14. Martin, T., E. Jovanov, and D. Raskovic, *Issues in Wearable Computing for Medical Monitoring Applications: A Case Study of a Wearable ECG Monitoring Device*. Proc of The International Symposium on Wearable Computers ISWC Atlanta, Georgia, 2000: p. 43 - 50.
15. Molisch, A.F., J.R. Foerster, and M. Pendergrass, *Channel models for ultrawideband personal area networks*. Wireless Communications, IEEE, 2003. **10**(6): p. 14-21.
16. Pandolfino, J.E., et al., *Ambulatory Esophageal pH Monitoring Using a Wireless System*. American Journal of Gastroenterology, 2003. **98**(4): p. 740-749.
17. Park, S. and S. Jayaraman, *Wearable Technology Enhancing the Quality of Life Through Wearable Technology*. Special Issue of the IEEE Engineering in Medicine and Biology Magazine, 2003. **22**(3): p. 41 - 48.
18. Pentland, S., *Healthwear: Medical Technology Becomes Wearable*. Computer, 2004. **37**(5): p. 34 - 41.
19. Raskovic, D., T. Martin, and E. Jovanov, *Center for Wireless Integrated Microsystems (WIMS) Medical Monitoring Applications for Wearable Computing*. The Computer Journal, 2004. **47**(4): p. 495 - 504.
20. Salonidis, T., et al., *Distributed topology construction of Bluetooth wireless personal area networks*. Selected Areas in Communications, IEEE Journal on, 2005. **23**(3): p. 633-643.
21. Van Laerhoven, K., et al., *Towards A Wearable Inertial Sensor Network*. IEE EuroWearable 2003 (EuroWearable), 2003.
22. Welch, J., F. Guilak, and S.D. Baker, *A Wireless ECG Smart Sensor for Broad Application in Life Threatening Event Detection*. Proc of the 26th Annual International Conference of the IEEE Engineering in Medicine and Biology Society, 2004: p. 3447 - 3449.
23. Zworykin, V.K., *Radio Pill*. Nature, 1957. **179**: p. 898.
24. IEEE, *Standard for Safety Levels with Respect to Human Exposure to Radio Frequency Magnetic Fields, 3 kHz to 300 GHz*. IEEE Standard C95.1-2005, 2006.
25. Beck, B.L., et al., *Tissue-Equivalent Phantoms for High Frequencies*. Concepts in Magnetic Resonance Part B: Magnetic Resonance Engineering, 2003. **20B**(1): p. 30-33.
26. Durney, C.H. and D.A. Christensen, *Basic Introduction to Bioelectromagnetics*. 1st ed. 2000, New York: CRC Press LLC. 169.

27. Hartsgrove, G., A. Kraszewski, and A. Surowiec, *Simulated Biological Materials for Electromagnetic Radiation Absorption Studies*. Bioelectromagnetics, 1986. **8**: p. 29-36.
28. Foster, K.R. and H.P. Schwan, *Dielectric Properties of Tissue - A Review, Handbook of Biological Effects of Electromagnetic Radiation*. 1986, Cleveland: CRC Press.
29. Gabriel, S., R.W. Lau, and C. Gabriel, *The Dielectric Properties of Biological Tissues: I. Literature Survey*. Phys Med Biol 1996. **41**: p. 2231–2249.
30. Gabriel, S., R.W. Lau, and C. Gabriel, *The Dielectric Properties of Biological Tissues: II. Measurements in the Frequency Range of 10 Hz to 20 GHz*. Phys Med Biol 1996. **41**: p. 2251–2269.
31. Gabriel, S., R.W. Lau, and C. Gabriel, *The Dielectric Properties of Biological Tissues: III. Parametric Models for the Dielectric Spectrum of Tissues*. Phys Med Biol 1996. **41**: p. 2271–2293.
32. Stuchly, M.A., et al., *Dielectric properties of animal tissues in vivo at frequencies 10 MHz - 1 GHz*. Bioelectromagnetics, 1981. **2**(2): p. 93-103.
33. Stuchly, M.A. and S.S. Stuchly, *Dielectric Properties of Biological Substances*. Journal of Microwave Power, 1980. **15**: p. 19-26.
34. Mazzara, G.P., et al., *Use of a Modified Polysaccharide Gel in Developing a Realistic Breast Phantom for MRI*. Magnetic Resonance Imaging, 1996. **14**(6): p. 639-648.
35. Athey, T.W., et al., *Measurement of Radio Frequency Permittivity of Biological Tissues with an Open-Ended Coaxial Line: Part I. Microwave Theory and Techniques*, IEEE Transactions on, 1982. **82**(1): p. 82-86.
36. Burdette, E.C., F.L. Cain, and J. Seals, *In-Vivo Probe Microwave Technique for Determining Dielectric Properties at VHF through Microwave Frequencies*. IEEE Trans Microwave Theory Tech, 1980. **29**: p. 414-427.
37. Kraszewski, A., M.A. Stuchly, and S.S. Stuchly, *ANA Calibration Method for Measurements of Dielectric Properties Instrumentation and Measurement*, IEEE Transactions on, 1983. **32**(2): p. 385-387.
38. Kraszewski, A., et al., *On the Measurement Accuracy of the Tissue Permittivity In Vivo*. IEEE Trans Instrum Meas 1986. **32**: p. 37-42.
39. Ulaby, F.T., *Fundamentals of Applied Electromagnetics*. 2004 Media Edition ed. 2004, Upper Saddle River: Pearson Prentice Hall. 433.

40. *Handbook of Biological Effects of Electromagnetic Fields*, ed. C. Polk and E. Postow. 1996, Boca Raton: CRC Press 597.
41. Elliot, R.S., *Electromagnetics*. 1966, New York: McGraw-Hill, Inc. 631.
42. Papas, C.H., *Theory of Electromagnetic Wave Propagation*. 1965, New York: McGraw-Hill. 244.
43. WHO, *Electromagnetic fields (EMF)*. 2009, World Health Organization.
44. Repacholi, M.H., *Low-level exposure to radiofrequency electromagnetic fields: Health effects and research needs*. *Bioelectromagnetics*, 1998. **19**(1): p. 1-19.
45. Peterson, D.M., et al., *An MR Transceive Phased Array Designed for Spinal Cord Imaging at 3 Tesla: Preliminary Investigations of Spinal Cord Imaging at 3 T*. *Investigative Radiology*, 2003. **38**(7): p. 428-435.
46. Gordon, C.J., *Local and Global Thermoregulatory Responses to MRI Fields*. *Annals New York Academy of Sciences*, 1992. **649**: p. 273-284.
47. Durney, C.H., H. Massoudi, and M.F. Iskandler, *Radiofrequency Radiation Dosimetry Handbook, Report USAFSAM-TR85-73*. 4th ed. 1986, Brooks Air Force Base: USAF School of Aerospace Medicine.
48. ICNIRP, *Guidelines for limiting exposure to time varying electric, magnetic and electromagnetic fields (up to 300 GHz)*. *Health Physics*, 1998. **74**: p. 494-522.
49. INIRC-IRPA, *Guidelines for limiting exposure to time varying electric, magnetic and electromagnetic fields (up to 300 GHz)*. *Health Physics*, 1998. **74**: p. 494-522.
50. FCC, *Radio Frequency Devices, Rules Part 15*. <http://www.fcc.gov/oet/info/rules/part15/>, 2006.
51. NCRP, *Radiofrequency Electromagnetic Fields: Properties, Quantities and Units, Biophysical Interaction, and Measurements*. National Council on Radiation and Protection Measurements, 1981. **67**.
52. FDA, *Quality System Regulation (QS)/Good Manufacturing Practices (GMP) - 21 CFR Part 820*, in <http://www.fda.gov/cdrh/devadvice/overview.html>. 2007.
53. Tang, J., et al., *An alternative to fourier transform spectral analysis with improved resolution*. *J of Magn Reson*, 1985. **62**: p. 167-171.
54. OSHA, *Occupational Safety and Health Standards, No. 1910.97*. United States Department of Labor, 1996.
55. EPA, *Radiation Protection and Control Act* Radiation Protection Committee, 1982.

56. Hoult, D.I., *The principle of reciprocity in signal strength calculations - A mathematical guide*. Concepts in Magnetic Resonance, 2000. **12**(4): p. 173-187.
57. Debye, P., *Polar Molecules*. Chemical Catalog. 1929, New York: Dover Publications.
58. Cole, K.S. and R.H. Cole, *Dispersion and absorption in dielectrics*. J. Chem. Phys., 1941. **9**: p. 341-351.
59. Mitsunami, K., et al., *In vivo 31P nuclear magnetic resonance spectroscopy in patients with old myocardial infarction*. Jpn Circ J, 1992. **56**: p. 614-619.
60. Gabriel, C.; Chadwick, P., "Development of Whole-Body Shell and Solid Phantoms and for SAR and Radio Propagation Measurement," *Bioinformatics and Biomedical Engineering, 2008. ICBBE 2008*. p.805-807.
61. Ogawa, K., et al. *A high-precision real human phantom for EM evaluation of handheld terminals in a talk situation*. in *Antennas and Propagation Society International Symposium, 2001. IEEE*. 2001.
62. Wieczorek, D.J.J. and C.C.K. Wang, *A 3D In-Phantom Dosimetry System to Estimate the Effective Dose Equivalent*. Radiat Prot Dosimetry, 1998. **76**(3): p. 149-157.
63. Seppi, E.J., et al., *Megavoltage cone-beam computed tomography using a high-efficiency image receptor*. International Journal of Radiation Oncology*Biography*Physics, 2003. **55**(3): p. 793-803.
64. Balanis, C.A., *Antenna Theory Analysis and Design*. 2nd ed. 1997, New York: John Wiley and Sons, Inc. 941.
65. Angelone, L.M., et al., *On the effect of resistive EEG electrodes and leads during 7 T MRI: simulation and temperature measurement studies*. Magnetic Resonance Imaging, 2006. **24**(6): p. 801-812.
66. Ayatollahi, M., et al. *Effects of supporting structure on wireless SAR measurement*. in *Antennas and Propagation Society International Symposium, 2008. AP-S 2008. IEEE*. 2008.
67. Gallo, M., P.S. Hall, and M. Bozzetti. *Use of Animation Software in the Simulation of On-Body Communication Channels*. in *Antennas and Propagation Conference, 2007. LAPC 2007. Loughborough*. 2007.
68. Jayawardene, M., et al. *Comparative study of numerical simulation packages for analysing miniature dielectric-loaded bifilar antennas for mobile communication*. in *Antennas and Propagation, 2001. Eleventh International Conference on (IEE Conf. Publ. No. 480)*. 2001.

69. Tarvas, S. and A. Isohatala. *An internal dual-band mobile phone antenna*. in *Antennas and Propagation Society International Symposium, 2000. IEEE*. 2000.
70. Yu, H., et al., *Printed capsule antenna for medication compliance monitoring*. *Electronics Letters*, 2007. **43**(22).
71. Brown, S.B. and R.P. Shannon, *Improving Medication Compliance in Patients With Heart Failure*. *The American Journal of Cardiology*, 2008. **101**(2): p. 274-277.
72. Fletcher, S.W., E.M. Pappius, and S.J. Harper, *Measurement of Medication Compliance in a Clinical Setting: Comparison of Three Methods in Patients Prescribed Digoxin*. *Arch Intern Med* 1979. **139**: p. 635-638.
73. Koehler, A.M. and H.I. Maibach, *Electronic Monitoring in Medication Adherence Measurement: Implications for Dermatology*. *American Journal of Clinical Dermatology*, 2001. **2**(1): p. 7-12.
74. McDonald, H.P., A.X. Garg, and R.B. Haynes, *Interventions to Enhance Patient Adherence to Medication Prescriptions: Scientific Review*. *JAMA*, 2002. **288**(22): p. 2868-2879.
75. Perri, M., www.rx.uga.edu/main/home/phrm3900/compliance.ppt
76. Wagner, G.J. and J.G. Rabkin, *Measuring Medication Adherence: Are Missed Doses Reported More Accurately than Perfect Adherence?* *AIDS Care*, 2000. **12**(4): p. 405.
77. Uko-Ekpenyong, G., *Improving Medication Adherence with Orally Disintegrating Tablets*. *Nursing*, 2006. **36**(9): p. 20-21.
78. Burke, W.S. and I.S. Ockene, *Compliance in Healthcare and Research*. 2001, Armonk, NY: Futura Publishing Company, Inc.
79. Farmer, K.C., *Methods for Measuring and Monitoring Medication Regimen Adherence in Clinical Trials and Clinical Practice*. *Clin Ther*, 1999. **21**(6): p. 1074-1090.
80. Lei, W., T.D. Drysdale, and D.R.S. Cumming, *In Situ Characterization of Two Wireless Transmission Schemes for Ingestible Capsules*. *IEEE Transactions on Biomedical Engineering*, 2007. **54**(11): p. 2020-2027.
81. Tufts. *Tufts CSDD Outlook Report*. 2005 [cited; Available from: <http://csdd.tufts.edu/InfoServices/OutlookReports.asp>].
82. Finkenzeller, K., *RFID Handbook*. 2nd ed. 2003, New York: John Wiley and Sons, Inc. 427.

83. Scanlon, W.G., J.B. Burns, and N.E. Evans, *Radio Wave Propagation from a Tissue-implanted Source at 418MHz and 916.5MHz*. IEEE Transactions on Biomedical Engineering, 2000. **47**(4): p. 527-533.
84. IEEE, *Standard for Local and metropolitan area networks. Part 16: Air Interface for Broadband Wireless Access Systems*. IEEE Standard 802.16-2009.
85. Yang, Q.X., et al. *Phantom Design in the Presence of Wave Behavior of the Radiofrequency Field*. in *10th Scientific Meeting of the International Society for Magnetic Resonance In Medicine*. 2002. Honolulu, HI.
86. Reed, J., *FCC Part 15 Rules Clarification*, D.M. Peterson, Editor. 2008.
87. Fujimoto, K., et al., *Small Antennas*. 1st ed. Electronics and Electrical Engineering Research Studies, Antenna Series, ed. J.R. James. 1987, New York: John Wiley and Sons Inc. 300.
88. Johnson, R.C., *Antenna Engineering Handbook*. 3rd ed, ed. R.C. Johnson. 1993, New York: McGraw-Hill, Inc.
89. Terman, F.E., *Radio Engineers' Handbook*. 1st ed. 1943, New York: McGraw-Hill. 1019.
90. Fukushima, E. and S.B.W. Roeder, *Experimental Pulse NMR: A Nuts and Bolts Approach*. 1981, Boulder: Westview Press. 539.
91. Collin, R.E., *Foundations for Microwave Engineering*. 1966, New York: McGraw-Hill, Inc. 589.
92. Hsu, H.P., *Signals and Systems*. 1995, New York: McGraw-Hill.
93. Karu, Z.Z., *Signals and Systems Made Ridiculously Simple*. 1st ed. 2002, Cambridge: ZiZi Press. 122.
94. Ludwig, R. and Bogdanov, G. *RF Circuit Design: Theory and Applications*. 2nd ed. 2009, Upper Saddle River, NJ: Pearson Prentice Hall
95. Graf, R.F., *The Modern Amplifier Circuit Encyclopedia*. 1st ed. 1992, New York: McGraw-Hill.
96. Ifeachor, E.C. and B.W. Jervis, *Digital Signal Processing: A Practical Approach*. 1st ed. Electronic Systems Engineering Series. 1993, New York: Addison-Wesley. 760.
97. NessAvier, M., *All You Really Need to Know About MRI Physics*. 1997, Baltimore, MD: Simply Physics.

98. King, S.B., *Evolution of Methodology for Obtaining ¹H Magnetic Resonance Spectra of Thyroid Nodules in Vivo*, in *Physics and Astronomy*. 1999, University of Manitoba: Winnipeg, Manitoba Canada. p. 198.
99. Andrew, E.R., *Nuclear Magnetic Resonance*. 1955, New York: Cambridge University Press. 265.

BIOGRAPHICAL SKETCH

David Michael Peterson was born in Eau Claire, Wisconsin in July 1969 and grew up in the Northwoods of WI, graduating from Cadott High School in 1987. He subsequently joined the United States Army and was eventually stationed in Berlin Germany in March of 1989 and was present for the fall of the Berlin Wall on 9 November 1989 a day that will stand out in history and forever changed this nation's view on communism and socialism. The question for this country is, will we remember that lesson and learn from it? David went through the U.S. Army Basic Airborne Course (BAC) in 1992, upon successfully completion of this course he went on to pursue scholastic endeavors and graduated from Florida Agricultural and Mechanical (A&M) University in 1995 with a degree in Electronics Engineering Technology. His first employment as an engineer was working for Dr. Jeffrey Fitzsimmons doing MRI coil design; from there he took a job in industry at MRI Devices Corporation in 2000 and attained a Master's of Science degree in Engineering from Newport, University in 2001. In 2002, Mr. Peterson returned to the University of Florida to do grant work and pursue a PhD in Biomedical Engineering which he started in the fall of 2003. Currently, David is the Director of Operations for Midwest RF, LLC and a producer of specialized MRI coils.